GEOMECHANICAL MODELING OF GAS HYDRATE BEARING SEDIMENTS AND OTHER COMPLEX SOILS

A Dissertation

by

XUERUI GAI

Submitted to the Office of Graduate and Professional Studies of
Texas A&M University
in partial fulfillment of the requirements for the degree of

DOCTOR OF PHILOSOPHY

Chair of Committee,	Marcelo Sanchez
Committee Members,	Charles Aubeny
	Robert Lytton
	I. Yucel Akkutlu
Head of Department,	Robin Autenrieth

May 2018

Major Subject: Civil Engineering

ABSTRACT

The research presented in this dissertation is aimed at advancing the current understanding of the mechanical behavior of three distinct complex soil systems, as follows: gas hydrate bearing sediment, partially saturated clay silt and microbially induced calcite precipitation treated sands. Particular emphasis is placed on the mechanical constitutive modeling of these different soil systems.

Gas hydrate bearing sediments (GHBS) are considered a potential future energy resource. The existence of the ice-like hydrates in the pore space and the associated phase change during hydrate dissociation make the modeling of GHBS very challenging. This thesis presents two novel constitutive models for GHBS that incorporate a number of improvements that allow simulating features of sediments behavior that were not captured by previous approaches. First, a simpler model was developed based on the critical state soil mechanics theory for strain hardening materials which was enhanced and validated with experimental tests involving shearing at constant hydrate saturation. This basic model was then upgraded using strain-partition concepts with the aim to achieve a better description of GHBS behavior. This model allows tracking the evolution of the mechanical contribution from the sediment and hydrate during shearing and dissociation. This is a novel aspect that was not considered in previous constitutive models and that greatly assists to gain a better understanding about the geomechanical response of this complex multiphase material.

The progresses and developments made in the constitutive modeling of GHBS were adapted and extended to model other two geomaterials of great interest nowadays, as follows: unsaturated soils and treated soils by microbially induced calcite precipitation (MICP). The study of unsaturated soils is very relevant as they are often encountered in engineering applications. Furthermore, the mechanical behavior of partially saturated soils can be very different compared to that of fully saturated ones. The most popular framework to study the behavior of unsaturated soils is the so-called Barcelona Basic Model (BBM). This is an excellent model able to capture the main features of unsaturated soils, however it has some limitations to properly model materials exhibiting dilatancy during shearing. This model has been enhanced in this thesis. A critical comparison between the performances of these two models is carried out. It is observed that the enhanced model is able to satisfactorily capture the complex behavior observed in the lab and improve the response of the BBM for this type of soils. Finally, the focus is on the study of MICP treated soils. Microbially induced calcite precipitation (MICP) is a promising soil improvement technique for improving the performance of soft/loose soils. Sand is often the selected host soil in the lab to investigate this type of treatment. The mechanical behavior of MICP treated sand is carefully reviewed and an elastoplastic constitutive model is proposed for first time. The proposed model is widely validated against a number of laboratory experiments under different conditions. Also in this case the results are very satisfactory showing that the proposed model is capable of dealing with this type of treated soils.

ACKNOWLEDGEMENTS

I would like to express my sincere gratitude to my advisor, Dr. Marcelo Sanchez, for his support, guidance, patience and encouragement throughout my graduate studies. I felt I was so lucky to have him as my advisor as he had always been always there for me. The lessons I learnt from him is not limited to technical and research skills, but he also made me a better human in life by setting an example of excellence of as mentor, professor and role model. My thanks also go to the members of my committee members, Dr. Charles Aubeny, Dr. Robert Lytton and Dr. I. Yucel Akkutlu for their guidance and support throughout the course of this research.

Finally, thanks to my mother and father for their encouragement and love.

CONTRIBUTORS AND FUNDING SOURCES

This work was supervised by a dissertation committee consisting of Prof. Marcelo Sanchez, Prof. Charles Aubeny and Prof. Robert Lytton of the Zachry Department of Civil Engineering and Prof. I. Yucel Akkutlu of Harold Vance Department of Petroleum Engineering.

All work for the thesis (or) dissertation was completed by the student, under the advisement of Prof. Marcelo Sanchez of the Zachry Department of Civil Engineering. The work in Section 4 is completed by the student in collaboration with Prof. Marcelo Sanchez of the Zachry Department of Civil Engineering and Prof. J. Carlos Santamarina of Physical Science and Engineering Division, King Abdullah University of Science and Technology. The work in Section 5 is in collaboration with Prof. Marcelo Sanchez of the Zachry Department of Civil Engineering and Prof. Enrique Romero Morales of Department of Civil and Environmental Engineering, Universitat Politècnica de Catalunya.

Graduate study was supported by a project funded by Department of Energy, US and the Dissertation Fellowship from the Texas A&M University Office of Graduate and Professional Studies.

TABLE OF CONTENTS

Page

ABSTRACT ii

ACKNOWLEDGEMENTS iv

CONTRIBUTORS AND FUNDING SOURCES v

TABLE OF CONTENTS vi

LIST OF FIGURES ix

LIST OF TABLES xiv

1 INTRODUCTION 1

- 1.1 Background 1
  - 1.1.1 Gas hydrate bearing sediments 1
  - 1.1.2 Unsaturated soils 5
  - 1.1.3 Microbially induced calcite precipitation treated sand 6
- 1.2 Objectives and activities related to the thesis research 8
- 1.3 Outline 9

2 MECHANICAL PROPERTIES OF GHBS 12

- 2.1 Laboratory test conducted on GHBS-constant saturation 12
- 2.2 Laboratory test conducted on GHBS-hydrate dissociation 15
- 2.3 Previous modeling efforts 19
- 2.4 Discussion 21

3 HIERARCHICAL CRITICAL STATE MODEL 24

- 3.1 Introduction 24
- 3.2 Model description 24
- 3.3 Model application 33
  - 3.3.1 Case 1-Morphology effect 34
  - 3.3.2 Case 2-Natural core sediment 37
  - 3.3.3 Case 3-Different hydrate saturation 44

3.4 Conclusion and discussion 47

4 ADVANCED GHBS MODEL WITH STRESS-PARTITION 49

4.1 Introduction 49
4.2 Model description..50
    4.2.1 Basic relationships 50
    4.2.2 Constitutive model for hydrate 53
    4.2.3 Constitutive model for the sediment skeleton..55
    4.2.4 Final stress-strain relationships...59
4.3 Model application-constant S_h 61
    4.3.1 Case 1-Different hydrate saturation..62
    4.3.2 Case 2-Morphology effect 66
    4.3.3 Case 3-Natural core sediment 69
4.4 Parametric study..72
    4.4.1 Case 1-Confining pressure..72
    4.4.2 Case 2-Different χ_0 76
4.5 Hydrate dissociation under loading...78
    4.5.1 Case 1-hydrate dissociation under triaxial conditions 78
    4.5.2 Case 2-hydrate dissociation under oedometric conditions 86
4.6 Conclusion and discussion 92

5 MECHANICAL BEHAVIOR OF A PARTIALLY SATURATED SOIL...................94

5.1 Introduction 94
5.2 Experimental program..95
    5.2.1 Tested material and compaction procedure 95
    5.2.2 Triaxial cell and stress paths followed...96
5.3 Test results and interpretation within the Barcelona Basic Model........................104
    5.3.1 Barcelona Basic Model main components..104
    5.3.2 Parameter estimation...106
    5.3.3 Main experimental and modeling results...110
5.4 Enhanced BBM with sub-loading concepts 119
    5.4.1 Enhanced BBM Model formulation 119
    5.4.2 New modeling results 122
5.5 Conclusions and discussion...127

6 MECHANICAL BEHAVIOR OF MICP TREATED SAND....................................130

6.1 Introduction 130
6.2 Mechanical behavior of MICP treated sand 132
6.3 Model description 136
  6.3.1 Yield surface 136
  6.3.2 Stiffness matrix 139
  6.3.3 Hardening law and flow rule 140
  6.3.4 Stress-strain relation 141
6.4 Model application 142
  6.4.1 Host sand 143
  6.4.2 Drained triaxial compression loading tests I 146
  6.4.3 Drained compression loading with various $CaCO_3$ mass content 152
  6.4.4 Parametric study-damage rate 158
  6.4.5 Drained loading under various confining pressure 161
  6.4.6 Drained loading under various loading path 165
6.5 Conclusion and discussion 170

7 CONCLUSIONS AND SCOPE FOR FURTHER WORK 172

7.1 Introduction 172
7.2 Gas hydrate bearing sediment 172
7.3 Partially saturated soil 176
7.4 MICP treated sand 177
7.5 Concluding remarks 179

REFERENCES 180

LIST OF FIGURES

Page

Figure 1-1 GHBS occurrence in nature: a) gas hydrates (white) in coarse grain sediment (grey); b) pore-filling gas hydrates in sandy sediment; c) gas hydrates in fine-grained sediment; d) large chunks or nodules like gas hydrates..2

Figure 1-2 Phase boundaries for water-gas mixtures in the pressure-temperature space. Adapted from (Sanchez et al, 2014) 3

Figure 1-3 Global gas hydrates resource potential..4

Figure 1-4 Schematic representation of the partially saturated soil..................................6

Figure 2-1 Main types of hydrate morphology: a) cementation; b) pore filling; and c) load-bearing 13

Figure 2-2 Tests on natural and synthetic GHBS in terms of stress-strain behavior and volumetric response. a) specimens prepared at different hydrate saturation (Miyazaki et al., 2011); and b) samples prepared with different hydrate morphology(Masui et al., 2008)..15

Figure 2-3 Experimental results: a) drained triaxial tests involving hydrate dissociation (Hyodo et al., 2014); b) behavior of a natural GHBS subjected to loading and dissociation under stress at oedemetric conditions(Santamarina et al., 2015) 18

Figure 2-4 a) Schematic representation of the hydrate damaged during shearing; b) rearrangement of the GHBS structure upon dissociation.............................23

Figure 3-1 Different HISS yield surface options 25

Figure 3-2 Yield surfaces incorporating sub-loading concepts.......................................29

Figure 3-3 Modeling and experimental results: a) stress strain behavior, b) volumetric response. Experimental data from Masui et al. (2005)..................36

Figure 3-4 Modified Cam-Clay model results: a) stress strain relationship specimen S_h =38%; b) stress strain relationship specimen S_h =79%; c) volumetric response specimen S_h =38%; d) volumetric response specimen S_h =79%; e) stress path and yield surface evolution specimen

S_h =38%; and f) stress path and yield surface evolution specimen S_h =79%. Experimental data from (Yoneda et al., 2015) 40

Figure 3-5 Initial yield surfaces adopted for MCC and HISS a) specimen S_h 38%; and b) specimen S_h 79% 41

Figure 3-6 HISS model results: a) stress strain relationship specimen S_h =38%; b) stress strain relationship specimen S_h =79%; c) volumetric response specimen S_h =38%; d) volumetric response specimen S_h =79%; e) stress path and yield surface evolution specimen S_h =38%; and f) stress path and yield surface evolution specimen S_h =79%. Experimental data from Yoneda et al. (2015b) 43

Figure 3-7 Modeling the drained triaxial tests on synthetic samples using the HISS MH model: a) stress strain behavior, b) volumetric response. Experimental data from Hyodo et al. (2013) 45

Figure 4-1 Schematic representation of GHBS 51

Figure 4-2 Comparisons between model and experimental results for synthetic samples of GHBS prepared at different hydrate saturations: a) stress-strain behavior, b) volumetric response. Experimental data from (Hyodo et al., 2013) 65

Figure 4-3 Comparisons between model and experimental results for synthetic Toyoura sand samples with different hydrates pore habits: a) stress strain behavior, b) volumetric response. Experimental data from (Masui et al., 2008) 68

Figure 4-4 Comparisons between model and experimental results for triaxial tests on natural samples: a) stress strain behavior, b) volumetric response. Experimental data from (Yoneda et al., 2015) 71

Figure 4-5 Effect of confinement on GHBS response: a) stress strain behavior, b) volumetric response 73

Figure 4-6 Additional modeling information for the test in Fig 13 at σ'_c=1 MPa: a) stress-strain behavior; b) hardening variables; c) yield surfaces at two initial stages of the experiment A&B; and c) yield surfaces at two final stages of shearing C&D 75

Figure 4-7 Effect of χ_0 on HBS response: a) stress strain behavior, b) volumetric response 77

Figure 4-8 Experimental and modeling results for drained triaxial tests: a) already dissociated sediment, b) dissociation induced at ε_a=1%; and c) dissociation induced at ε_a=5%. Experimental data from (Hyodo et al., 2014) 82

Figure 4-9 Additional modeling information for the test in which dissociation was induced at ε_a=5%: a) extended stress-strain behavior; b) hardening variables, c) yield surfaces at the beginning of the experiment; and c) yield surfaces at an intermediate stage of shearing (ε_a=15.3%) and at the end of test 85

Figure 4-10 Behavior during dissociation of natural HBS specimens under oedometric conditions: a) core 8P; and b) core 10P. Experimental data from (Santamarina et al., 2015) 89

Figure 4-11 Additional modeling information for the test related to core 10P: a) vertical stresses computed by the model during loading; b) hardening variables 91

Figure 5-1 Compaction curve of samples 96

Figure 5-2. Scheme of the triaxial cell and picture. a) Specimen; b) local LVDT (axial strain); c) laser displacement sensor (radial strain); d) high air-entry ceramic disc surrounded by coarse metallic porous stone; e) Perspex wall; f) internal load cell; g) LVDT (vertical displacement of laser sliding subjection); h) confining air pressure; i) axial stress pressure chamber; j) water pressure (to volume change measuring system); k) air pressure; l) vertical displacement electric motor. Adapted from (Romero et al., 1997) 98

Figure 5-3 Stress paths followed in q : p : s space: a) tests A and B; b) tests C and D 100

Figure 5-4 Stress paths followed in p : s plane (Tests A, B, C and D). Activation of yield locus LC and SI. 102

Figure 5-5 Variation of q and ε_v under shearing. 103

Figure 5-6 Yield surfaces of the BBM model 106

Figure 5-7 Isotropic loading on saturated sample 107

Figure 5-8 Isotropic loading on unsaturated sample 108

Figure 5-9 Experimental results related to Barcelona clayey silt shear strength compiled from triaxial tests 109

Figure 5-10 Variation of volumetric strain with suction (A2→A3→A4)...................... 111

Figure 5-11 Evolution of LC and yield surface (A2→A3→A4) 113

Figure 5-12 Isotropic loading and unloading at constant suction (i.e. cycle path C1 → C2 → C3)... 114

Figure 5-13 Variation of volumetric strain with suction (D1 → D2 → D3). 115

Figure 5-14 Simulation of the shearing paths BBM 117

Figure 5-15 Evolution of LC and yield surface (B1→B2).. 118

Figure 5-16 Saturated isotropic test, experimental and Enhanced BBM result 123

Figure 5-17 Simulation of the shearing paths with enhanced BBM 125

Figure 5-18 Shear at different confining pressure (0.3, 0.6, 1.2 MPa) 127

Figure 6-1 Triaxial drained tests involving untreated and MICP treated specimens in terms of stress–strain behavior and volumetric response. Experimental data from (Montoya & DeJong, 2015) 133

Figure 6-2 Triaxial drained tests on MICP treated specimens with different $CaCO_3$ contents in terms of stress–strain behavior and excess pore pressure response. Experimental data from (Feng & Montoya, 2015) 134

Figure 6-3 Schematic representation of MICP sand: a) untreated sand; b) MICP treated sand; c) damaged MICP treated sand 135

Figure 6-4 Yield surface adopted in the model 139

Figure 6-5 Triaxial test results of host sand 145

Figure 6-6 Comparison of experimental and modeling results of drained triaxial compression tests on MICP treated sand (a) stress–strain behavior of the experiment; (b) stress–strain behavior of modeling; c) volumetric response of the experiment; d) volumetric response of the modeling 148

Figure 6-7 Comparison of experimental and modeling results: a) stress path evolution (experiment); b) stress path evolution (modeling); c) mean effective stress versus void ratio (experiment); d) mean effective stress versus void ratio (modeling) 150

Figure 6-8 Comparison of cementation degradation mechanism of the experiment and simulation 151

Figure 6-9 Comparison of experimental and modeling results of drained triaxial compression tests on MICP treated sand (a) stress–strain behavior of the experiment; (b) stress–strain behavior of modeling; c) volumetric response of the experiment; d) volumetric response of the modeling 154

Figure 6-10 Evolution of stress and corresponding yield surfaces. a) untreated;b)1.2% c) 2.4% and d) 5.1% 155

Figure 6-11 Evolution of main variables: a) damage factor (X) and sub-loading ratio (R); b) effective pre-consolidation pressure (p_c), bonding hardening parameter (p_b), and effective hardening parameter ($R\left(p_c+p_b\right)$) 157

Figure 6-12 Modeling the drained triaxial tests on MCIP treated sand (a) stress–strain behavior, and (b) volumetric response 159

Figure 6-13 Evolution of main model variables (p_c’, p_b, μ, and R) against axial strain: a) case 1 b) case 2 c) case 3 d) case 4 161

Figure 6-14 Comparison of experimental and modeling results of drained triaxial compression tests on MICP treated sand (a) stress–strain behavior of the experiment; (b) stress–strain behavior of modeling; c) volumetric response of the experiment; d) volumetric response of the modeling 163

Figure 6-15 Comparison of experimental and modeling results: a) stress path evolution (experiment); b) stress path evolution (modeling); c) mean effective stress versus void ratio (experiment); d) mean effective stress versus void ratio (modeling) 164

Figure 6-16 Comparison of experimental and modeling results of drained triaxial compression tests on MICP treated sand (a) stress–strain behavior of the experiment; (b) stress–strain behavior of modeling; c) volumetric response of the experiment; d) volumetric response of the modeling 167

Figure 6-17 Comparison of experimental and modeling results: a) stress path evolution (experiment); b) stress path evolution (modeling); c) mean effective stress versus void ratio (experiment); d) mean effective stress versus void ratio (modeling) 169

LIST OF TABLES

Page

Table 3-1 Different shape of yield surface 25

Table 3-2 Model parameters adopted in the modeling 36

Table 3-3 In situ conditions, soil index properties, and testing conditions 38

Table 3-4 Parameter adopted in the modeling 42

Table 3-5 Test conditions for triaxial compression tests 44

Table 3-6 Parameters adopted in the modeling 46

Table 4-1 Test conditions for triaxial compression tests studied 63

Table 4-2 Parameters adopted in the modeling 64

Table 4-3 Parameters adopted in the modeling 67

Table 4-4 In situ conditions, soil index properties, and testing conditions 70

Table 4-5 Parameters adopted in the modeling 70

Table 4-6 Parameters adopted in the modeling 72

Table 4-7 Parameters adopted in the modeling of HBS specimens. Effect of parameters*: χ_0 76

Table 4-8 Test conditions of methane hydrate dissociation tests 78

Table 4-9 Parameters adopted in the modeling 79

Table 4-10 Parameters adopted in the modeling of HBS specimens 86

Table 5-1 Material parameters used in the simulation (BBM) 110

Table 6-1 Model parameters of Ottawa sand (reference soil) 144

Table 6-2 Model parameters related with MICP treatment 146

Table 6-3 Soil index properties and testing conditions 147

Table 6-4 Soil index properties and testing conditions 152

Table 6-5 Different damage rates adopted in this study 158

Table 6-6 Soil index properties and testing conditions 162

Table 6-7 Soil index properties and testing conditions 165

1 INTRODUCTION

The aim of this chapter is to introduce the readers to the context of the research identifying the main aspects of the different soils under study alongside with the main objectives of the research and the main activities conducted. Finally, a detailed structure of the dissertation is presented.

1.1 Background

The background of each soil systems is introduced separately as below.

1.1.1 Gas hydrate bearing sediments

Gas hydrate bearing sediments (GHBS) are naturally occurring soils characterized by the presence of ice like gas (e.g., CH_4 or CO_2) hydrates in its pore space (Figure 1-1). Methane hydrate is the most common type of gas hydrates in nature. Water molecules clustered around methane molecules form a solid compound that are found in marine sediments and permafrost regions, where the (high) pressure and (low) temperature conditions guarantee the hydrates stability(Collett, 2002; Mahajan et al., 2007). Perturbations in pressure, temperature or water-chemistry may move the methane hydrates from its stability zone triggering hydrate dissociation (Figure 1-2). Hydrate dissociation is accompanied by gas and water production, as well as, by significant changes in the sediment structure and mechanical properties. The amount of hydrate in soils is commonly evaluated by means of the hydrate saturation (S_h), calculated as the ratio between the volume occupied by the hydrates and the volume of voids.

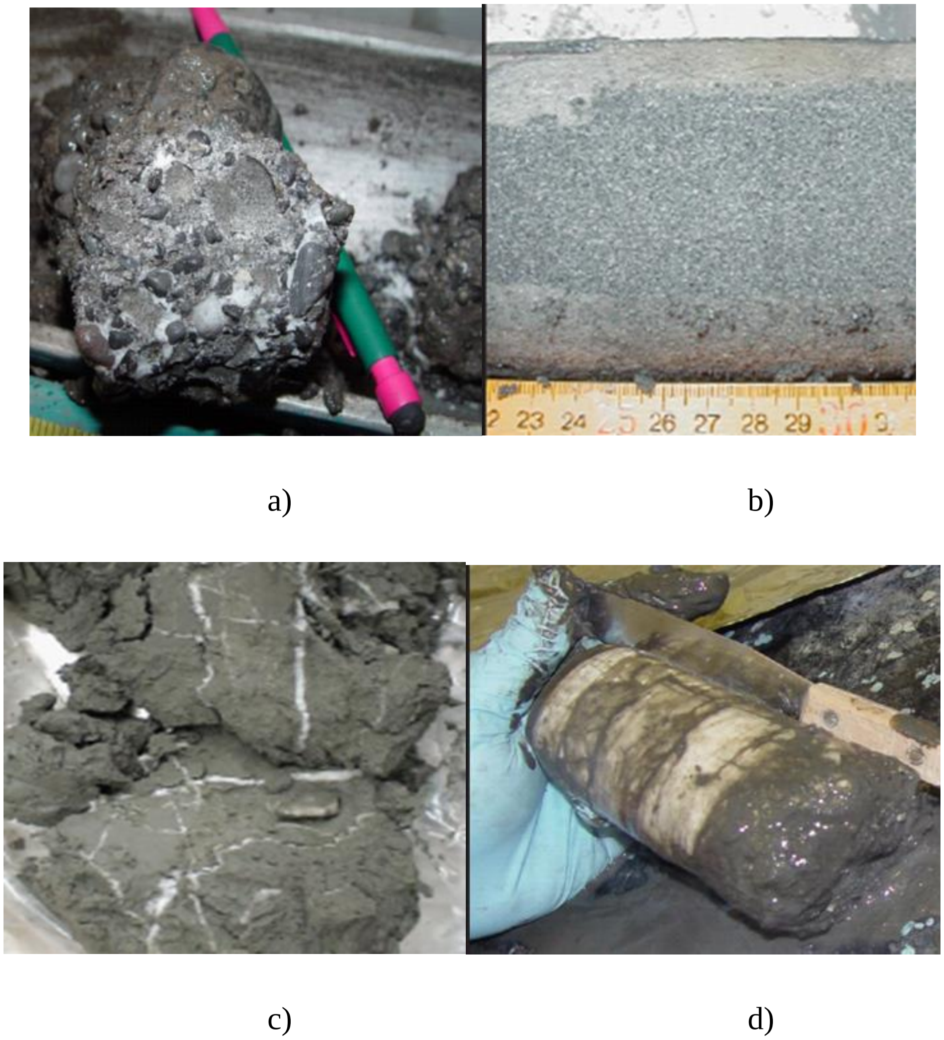

Figure 1-1 GHBS occurrence in nature: a) gas hydrates (white) in coarse grain sediment (grey); b) pore-filling gas hydrates in sandy sediment; c) gas hydrates in fine-grained sediment; d) large chunks or nodules like gas hydrates

Adapted from (Beaudoin et al., 2014)

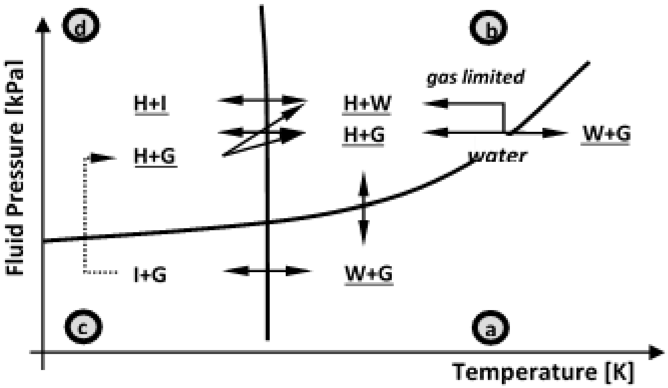

Figure 1-2 Phase boundaries for water-gas mixtures in the pressure-temperature space. Adapted from (Sanchez et al, 2014)

GHBS represent an attractive source of energy as significant methane reserves are found in the form of hydrates. The distribution of GHBS in the world is shown in Figure 1-3. Recent estimate that the total amount of methane trapped in natural gas hydrates range from 3000 to 30,000 Tcm (trillion cubic meters) of carbon at standard temperature and pressure, which is a larger hydrocarbon resource than all of the world's oil, natural gas and coal resources combined (Beaudoin et al., 2014). Due to the large magnitude of methane trapped in the pore space, GHBS are considered to be a significant energy resource for future exploitation. There are three mechanisms that can trigger hydrate dissociation thus generate methane gas. They are depressurization, thermal injection and chemical stimulation. Current methods accepted as feasible for extracting methane gas from GHBS are based on these three processes mainly.

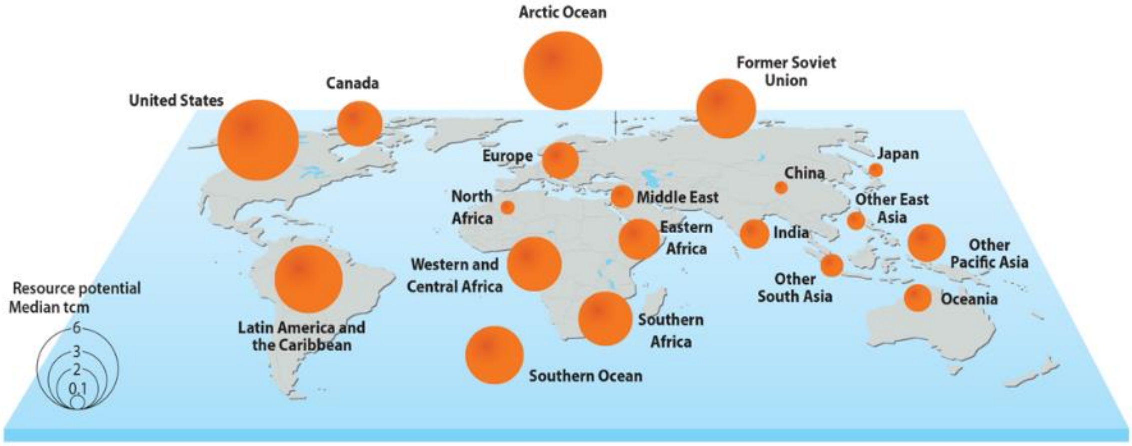

Figure 1-3 Global gas hydrates resource potential
Adapted from (Beaudoin et al., 2014)

Despite of the promising future, there exists a number of issues related with GHBS. Hydrate dissociation is a complex phenomenon involving changes in fluid pressure, effective stresses and mechanical structure of GHBS, which may lead to potential geo-hazards and engineering problems. For example, massive submarine landslides are in occasions related to hydrate dissociation from subsea sediments. This type of phenomenon generally involves large areas and may affect pipelines and other submarine infrastructure. A number of engineering problems (e.g. blowouts; platform foundation failures; and borehole instability) are sometimes triggered by hydrate dissociation. Furthermore, the venting of methane to the atmosphere during uncontrolled hydrate dissociation can negatively contribute to greenhouse effects (Beaudoin et al., 2014).

The issues discussed above have triggered significant research efforts to study the properties of GHBS. Numerous experimental study was conducted to understand the physical properties of GHBS. However, this type of study has been hindered by the instability of hydrate. The cost of field gas production test is enormous and the feasibility has to be accessed using numerical tools to reduce the risk of failure. This study focus on the geomechanical modeling of GHBS, which is a key component to perform realistic analyses of engineering problems involving this type of material. Two innovative constitutive mechanical models for GHBS were proposed and validated through a wide range of experimental data.

1.1.2 Unsaturated soils

Partially saturated soils (or unsaturated soils) are frequently encountered in engineering practice. Compared with saturated soils, the mechanical behavior of partially saturated soils is more complex due to the existence of both air and water in the pore space of the soil (Figure 1-4). The pressures difference between gas and water is known as soil suction. Buildings and civil infrastructure involving partially saturated soils can be dramatically affected by typical features associated with this type of soil. Therefore, a proper understanding and modeling of unsaturated soil behavior is critical for a safe and economical design of geotechnical structure’s.

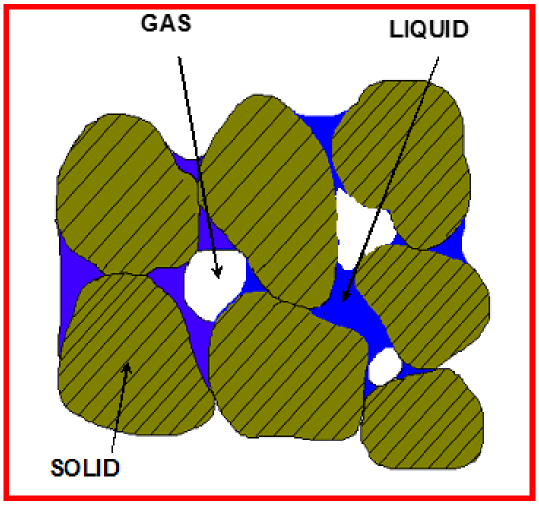

Figure 1-4 Schematic representation of the partially saturated soil Adapted from (Shastri, 2014)

In the past twenty years, the mechanical behavior of partially saturated soils has attracted the attention of several researches and companies. A critical step forward to advance the current understanding of the mechanical behavior of unsaturated soils is to conduct high quality experimental campaigns and to analyze the associated results with formal constitutive frameworks. In this study, an experimental and constitutive modeling collaboration efforts by the candidate and the group from Polytechnic University of Catalonia were presented.

1.1.3 Microbially induced calcite precipitation treated sand

Microbially induced calcite precipitation (MICP) is an innovative biomediated soil improvement method that can be used to induce cementation within originally loose and collapsible soils such as sand. This method utilizes biogeochemical processes with natural microbe has attracted a lot of attention recently (A Al Qabany & Soga, 2013; Ahmed Al Qabany et al., 2011; Bachmeier et al., 2002; Benini et al., 1999; Chou et al., 2011; J. T. DeJong et al., 2006; J. T. DeJong, Soga, et al., 2010; Fujita et al., 2010; B. Martinez et al., 2013; Mitchell & Santamarina, 2005; Stocks-Fischer et al., 1999; Weil et al., 2011). Enzymatic hydrolysis of urea of microbes is considered to be the most energy efficient of these processes (J. DeJong et al., 2013) and Sporosarcina pasteurii (ATCC 11859), an alkalophilic soil bacteria, has been recently used in laboratory studies to produce calcite precipitation (i.e. (Barkouki et al., 2011; Feng & Montoya, 2015; M. Li et al., 2013; Montoya & DeJong, 2015; Mortensen et al., 2011). Through MICP treatment, bacterially induced calcium carbonate can be generated in the void and at the contact of the soil matrix, thus creating artificial cementation on original soil matrix.

The idea of utilizing MICP as a soil improvement method for geotechnical problems has become popular recently (M. Burbank et al., 2012; M. B. Burbank et al., 2011; Cheng & Cord-Ruwisch, 2012; Chu et al., 2013; J. DeJong et al., 2009; J. DeJong et al., 2013; J. T. DeJong, Mortensen, et al., 2010; Gray & Sotir, 1996; Hamdan et al., 2017; Ivanov & Chu, 2008; James et al., 2000; M. Li et al., 2013; Manning, 2008; B. Martinez et al., 2013; B. C. Martinez & DeJong, 2009; Mitchell & Santamarina, 2005; L. Van Paassen, 2011; L. A. van Paassen, Daza, et al., 2010; L. A. van Paassen, Ghose, et al., 2010). For example, Whiffin et al. (Whiffin et al., 2007) found significant improvement in the behavior of soils treated with MICP in terms of both, strength and stiffness . The large-scale experiments conducted by van Paassen et al. (L. A. van Paassen, Ghose, et al.,

2010) were aimed at investigating the feasibility of MICP as a ground improvement. Method. It was observed that the stiffness of the treated sand increase significantly.

Recent modeling efforts associated with MICP treated soils have been mainly focused on the prediction of biogeochemical processes and precipitated calcite distribution (Barkouki et al., 2011; Fauriel & Laloui, 2012; B. Martinez et al., 2011; Van Wijngaarden et al., 2011, 2012). Despite the substantial interests in MICP, the modeling of the mechanical behavior of MICP treated soil is still limited. Fauriel & Laloui (Fauriel & Laloui, 2012) developed a bio-chemo-mechanical coupled approach to simulate the behavior of MICP treated soils. The mechanical constitutive model is based on non-linear elastic framework. Feng and Montoya Feng and Montoya (2015) used the discrete element method to study the mechanical behavior of MICP treated sands. In the last section of the dissertation, an elastoplastic critical state mechanical model is suggested for simulating the behavior of MICP treated sands which is the first of this kind as far as the author knows.

1.2 Objectives and activities related to the thesis research

The underlain aim of this research was to progress the current understanding and modeling of complex soils behaviors. A first step was to conduct an in-depth review related to the behavior of the three soils under study (i.e. GHBS, unsaturated soils, and MICP). The focus of the review was on two main aspects: i) the available information associated with the experimental behavior of these soils, and ii) the proposed constitutive models. A critical review of the available information allowed to identify the gaps on the state of the art and (based on it) achieve other of the objectives of this work that it was the proposal of new constitutive models capable of capturing the main features of these soils.

To assure that the news models were able to properly reproduce the actual soils behavior they were compared against available experimental data corresponding to different stress paths and tests conditions for the different types of soils considered in this thesis.

1.3 Outline

Section 1 of the dissertation provides the general background information about the studied soil systems, together with the objectives and outline of this dissertation.

A thorough literature review related with the mechanical behavior of GHBS is presented in Section 2. Section 2 is subdivided into two main parts. The first part presents a review of published experimental results related with GHBS. Tests with various conditions were studied and the mechanical behavior of GHBS were summarized. The second part reviews previous mechanical modeling efforts on this kind of sediment and their major characteristic were summarized.

Section 3 presents a mechanical constitutive model based on the concept of Hierarchical Single Surface (HISS) framework. The detailed mathematical formulation of the proposed model was firstly presented. Then, the model’s performance was examined by comparing the modeling results against experimental data. Various triaxial tests with different types of host sediment, hydrate morphology and confining pressure were selected to examine the proposed model.

Section 4 presents an advanced geomechanical constitutive model which incorporates stress partition concept, plus a number of inelastic mechanisms. The main components of the proposed model were first presented in detail. Then, the application and validation cases selected to study the behavior of GHBS are discussed. The model was applied and validated against experimental data from triaxial tests to 1D oedometric tests involving different hydrate saturation, hydrate morphology, and confinement conditions. Particular attention was paid to model the GHBS behavior during hydrate dissociation under loading.

Section 5 presents a joint effort conducted by the Texas A&M University and Polytechnic University of Catalonia to enhance the current understanding of partially saturated clay silt. The experimental study centred on the stress-strain response of a compacted clayey silt during shearing were conducted by the group from the Division of Geotechnical Engineering and Geosciences. Suction controlled triaxial cell with local axial and radial instrumentation is used to conduct suction-controlled isotropic and triaxial tests under different stress paths. The Barcelona Basic Model (BBM) was adopted as a formal tool to analyse the soil response to provide in-depth understanding of this type of soil. An enhanced mechanical model is then proposed to improve the current BBM to yield better prediction.

Section 6 presents a comprehensive study of the mechanical behavior of microbially induced calcite precipitation treat sand. As an innovative soil improvement techniques, it is important to understand the mechanical behavior of MICP treated soil before applying in engineering practice. This section first reviewed and summarized the mechanical response of MICP treated sand under various laboratory tests. Then, a constitutive model which account for these observation is proposed and presented in detail.

The model’s performance is examined through comparing model prediction and experimental data through a variety of conditions.

Section 7 presents the main conclusions and discussion of this study. Scope of future work is also suggested.

2 MECHANICAL PROPERTIES OF GHBS

As mentioned in the first chapter, hydrates in the pore space of the sediment may dissociate under thermal or depressurization condition. This phase change from solid hydrates to gas and water could induced significant structure changes of GHBS which can reflect on the mechanical response of the material. In the following sections, experimental evidences related to the mechanical behavior of GHBS are presented. The key features of GHBS under different stages are discussed in detail.

2.1 Laboratory test conducted on GHBS-constant saturation

Triaxial tests at constant hydrate saturation have provided very useful information to understand the influence of hydrate saturation and morphology on the mechanical behavior of GHBS. The presence of hydrates strongly affects key mechanical properties of soils. Gas hydrate increases the shear strength of the sediment. Hydrates specimens exhibit a softening behavior (after the peak stress) and more dilation than free hydrate samples. The sediment stiffness and strength generally increase with the increase in hydrate saturation. It has also been observed that the stiffness of GHBS degrade during shearing (Hyodo et al., 2014; Hyodo et al., 2005; Hyodo et al., 2013; Y. Li et al., 2011; Masui et al., 2005; Miyazaki et al., 2010; T. S. Yun et al., 2007; Zhang et al., 2012).

Hydrates are generally present in sediments in three main morphology types (Soga et al., 2006; Waite et al., 2009): a) cementation (Figure 2-1a); b) pore-filling (Figure 2-1b); and c) load-bearing (Figure 2-1c).

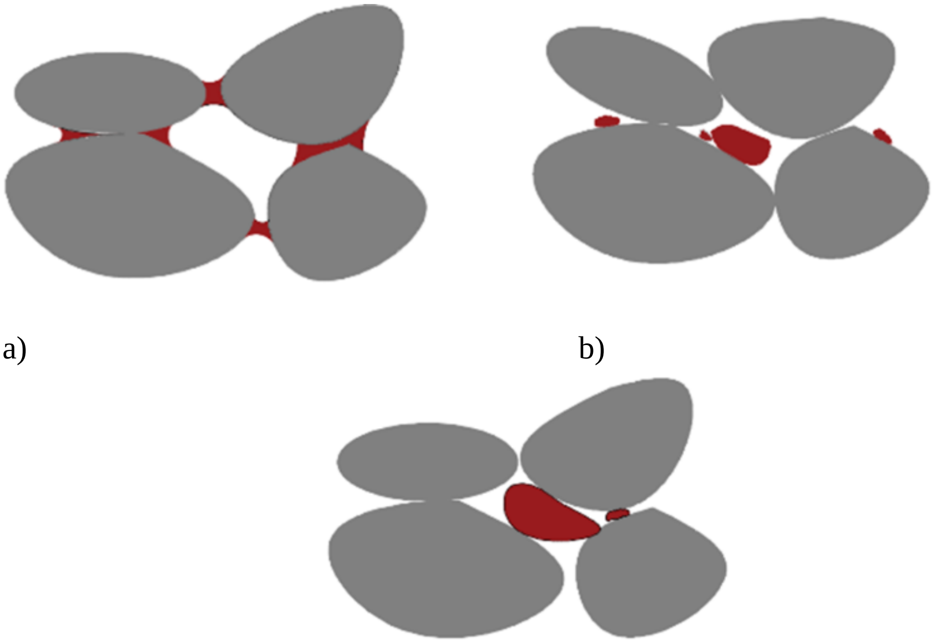

a)

b)

c)

Figure 2-1 Main types of hydrate morphology: a) cementation; b) pore filling; and c) load-bearing

Hydrates formed in the cementation mode are typically found at the contact between particles. A recent microstructural investigation (Chaouachi et al., 2015) (that does not involve any mechanical test), speculates about the actual cementation effects provided by the hydrates. However a large number of studies support that hydrates formed in the cementing mode do provide bonding between soil particles (Aman et al., 2013; Clayton et al., 2010; Jiang et al., 2014; Jiang et al., 2015; J. Lin et al., 2015; Lin et al., 2017; Liu et al., 2014; Masui et al., 2005; Shmulik Pinkert, 2016; Priest et al., 2009; J. Shen et al., 2016; Shen & Jiang, 2016; Z. Shen et al., 2016; S Uchida et al., 2012; Shun Uchida et al., 2016; Waite et al., 2009; Yu et al., 2016). For this morphology type, even a small hydrate saturation can significantly contribute to increase the sediment stiffness and strength (Dvorkin & Uden, 2004). In hydrate morphology type b), the hydrates nucleate on soil grains boundaries and grow freely into the pore space, without bridging two or more particles together. This type of hydrates also impacts on the mechanical properties of the sediments. When hydrate saturation is above 25%, this morphology turns into the load-bearing type c) (Berge et al., 1999; T. Yun et al., 2005; T. Yun et al., 2006). Sediment permeability and water storage capacity are significantly affected by the presence of hydrates in the load-bearing form (Helgerud et al., 1999). This mode is generally found in fine-grained soils and a typical example is the Mallik 5L-38 sediment (Dai et al., 2004).

Figure 2-2a presents some typical results showing the effect of S_h on stress-strain behavior and strain-volumetric response of natural methane hydrate samples under triaxial conditions (Masui et al., 2008). The type of hydrate pore-habit (i.e. morphology) also affects sediment behavior. For example, the tests conducted by Masui et al. (2005) to study the influence of hydrate morphology on the geomechanical response of hydrate bearing sediments are shown in Figure 2-2b. Of the three samples investigated in that research, the sample without hydrates (i.e. pure sediment) exhibited lower stiffness, strength, and dilatancy. The presence of hydrates increases the material stiffness, strength and dilatancy, corresponding the maximum values to the cementing mode (i.e. type 'a', above).

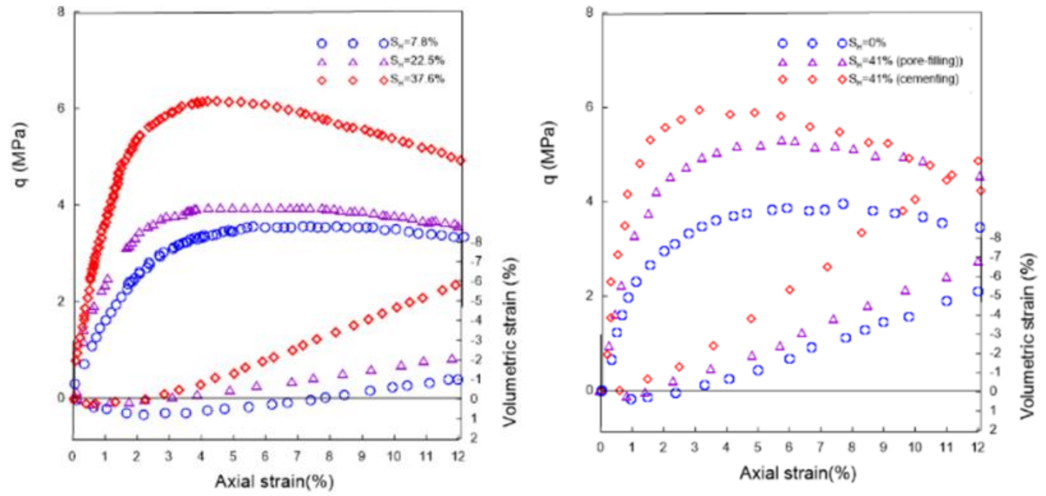

a) b)

Figure 2-2 Tests on natural and synthetic GHBS in terms of stress-strain behavior and volumetric response. a) specimens prepared at different hydrate saturation (Miyazaki et al., 2011); and b) samples prepared with different hydrate morphology(Masui et al., 2008)

2.2 Laboratory test conducted on GHBS-hydrate dissociation

Hydrate dissociation experiments under stress have allowed gaining a better understanding on the mechanical response of sediments when the presence of hydrates vanish or partially disappear. Two types of tests involving hydrate dissociation conducted under triaxial and oedemetric loading conditions are briefly discussed in this section.

Hyodo et al. (2014) adopted a temperature-controlled high pressure triaxial apparatus to mimic the formation and dissociation of methane hydrate in the deep seabed.

This device was used to conduct a series of triaxial compression tests on synthetic GHBS samples under various stress conditions. Toyoura sand was chosen as the host material to prepare samples with a similar porosity (i.e., ~40%), and with S_h ranging from ~37% to ~53%. Firstly, water and sand were mixed to form the specimen at the target density. The sample was placed in a freezer to keep it stand and then in a triaxial cell, at the target pressure and room temperature. Once the specimen was thawed, methane was injected into the specimen, while keeping the cell pressure and temperature condition inside the hydrate stability zone. Three experiments were selected in this work for the numerical simulations (see Section 5), namely: two triaxial tests at which hydrate dissociation was induced at two different initial axial strains (i.e., ε_a=1%, and ε_a=5%), and a third one in which the sample was subjected to shearing after the hydrates dissociated completely. These tests were conducted under isotropically consolidated specimens, at an effective confining stress σ'_c=5 MPa under drained conditions. Figure 2-3a presents the main experimental results in terms of axial strains against both deviatoric stress and volumetric strains. In one of the hydrate dissociation tests, the specimen was firstly sheared up to $q\approx8.4$ MPa (i.e., at ε_a=1%), then hydrate dissociation was induced at constant stress conditions and, once hydrate dissociation was completed, but the shearing continued up to ε_a=20%. A similar procedure was followed for the other test, but the maximum deviatoric load in this case was $q\approx12$ MPa (i.e., at ε_a=5%). The responses observed under these tests conditions are quite different. In the first test, the deviatoric stress after hydrate dissociation was smaller than the shear strength of the dissociated sediment, therefore a tendency to harden was observed in the subsequent shearing. However, in the second sample (i.e., dissociation induced at ε_a=5%) the deviatoric stress was higher than the strength of the dissociated sample. In consequence, a stress-softening behavior was observed during the hydrate dissociation stage, with a tendency of the deviatoric stress to decrease until reaching the maximum deviatoric stress observed in the already dissociated sample. More details about these tests and the associated modeling are presented in Section 4. The other set of experiments corresponds to the tests reported by (Santamarina et al., 2015). Two natural core samples were extracted from the Nankai Trough, offshore Japan, using the Pressure Core Characterization Tools (PCCT (Santamarina et al., 2012)). The tested cores were predominantly sandy- and clayey-silts, but also contained some silty-sands. Hydrate saturation ranged from ~15% to ~74%, with significant concentrations in the silty-sands samples. The PCCT was able to maintain the GHBS cores stable at field conditions. After retrieval, the cores were loaded under oedometric conditions and at some point, hydrate dissociation was induced under constant effective stress conditions. The mechanical behavior of the HBS specimens before, during and after dissociation was recorded. Figure 2-3 shows the results of a typical test in the 'effective stress chamber' (i.e., the sample coded as 'core-10P', with an initial S_h~74%). Prior to hydrate dissociation, the specimen was loaded up to an applied effective vertical stress σ'_v=3 MPa, then hydrate dissociation was induced via depressurization, maintaining the effective stress constant. Once the hydrates were fully dissociated, the specimen was loaded up to σ'_v=9 MPa, and it was unloaded afterwards. A significant volumetric collapse-compression deformation was observed during dissociation under load. This test and another one with lower hydrate dissociation (i.e., S_h~18%) are modeled and discussed in Section 4.

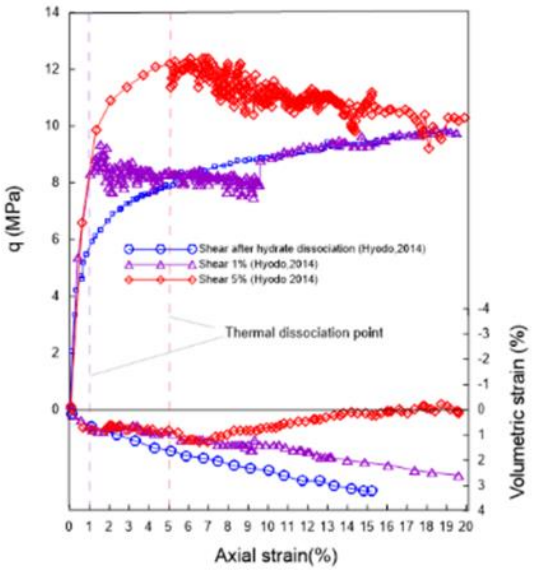

a)

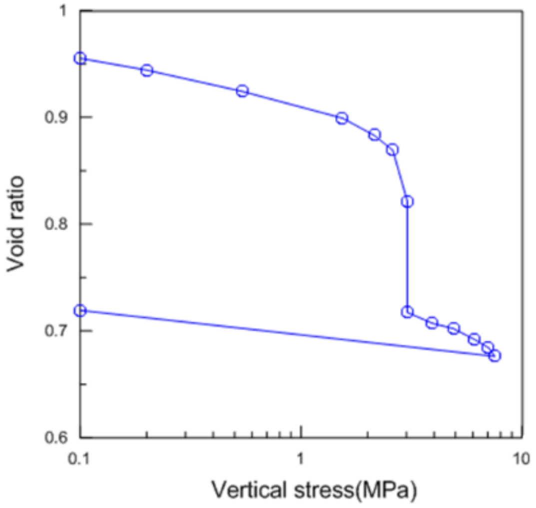

b)

Figure 2-3 Experimental results: a) drained triaxial tests involving hydrate dissociation (Hyodo et al., 2014); b) behavior of a natural GHBS subjected to loading and dissociation under stress at oedemetric conditions(Santamarina et al., 2015)

The other set of experiments corresponds to the tests reported by (Santamarina et al., 2015). Two natural core samples were extracted from the Nankai Trough, offshore Japan, using the Pressure Core Characterization Tools (PCCT (Santamarina et al., 2012)). The tested cores were predominantly sandy- and clayey-silts, but also contained some silty-sands. Hydrate saturation ranged from ~15% to ~74%, with significant concentrations in the silty-sands samples. The PCCT was able to maintain the GHBS cores stable at field conditions. After retrieval, the cores were loaded under oedometric conditions and at some point, hydrate dissociation was induced under constant effective stress conditions. The mechanical behavior of the HBS specimens before, during and after dissociation was recorded. Figure 2-3 shows the results of a typical test in the 'effective stress chamber' (i.e., the sample coded as 'core-10P', with an initial S_h~74%). Prior to hydrate dissociation, the specimen was loaded up to an applied effective vertical stress σ'_v=3 MPa, then hydrate dissociation was induced via depressurization, maintaining the effective stress constant. Once the hydrates were fully dissociated, the specimen was loaded up to σ'_v=9 MPa, and it was unloaded afterwards. A significant volumetric collapse-compression deformation was observed during dissociation under load. This test and another one with lower hydrate dissociation (i.e., S_h~18%) are modeled and discussed in Section 4.

2.3 Previous modeling efforts

Geomechanics is a key component in the numerical modeling of engineering problems involving GHBS. Several types of mechanical constitutive models for hydrate bearing sediment have been proposed in the last few years. Only a few of them are discussed below. For example, Miyazaki et al. (2012) suggested a nonlinear elastic model for hydrate bearing sands based on the Duncan-Chang model (e.g.,(Duncan & Chang, 1970)). The Mohr–Coulomb (MC) model has been adopted by several researchers to describe the behavior of GHBS. For instance, Rutqvist and Moridis (2007) simulated the geomechanical changes during gas production from GHBS undergoing depressurization-induced dissociation using a modified MC model. Klar et al. (2010) proposed a single-phase elastic–perfectly plastic MC model for hydrate soils based on the concept of effective stress that incorporates an enhanced dilation mechanism. Pinkert and Grozic (2014, 2015) proposed a model based on a non-linear elastic model (dependent on S_h) and the MC failure criterion. This model was able to fit well Miyazaki et al. (2011) experimental data. This model was used to simulate wellbore stability problems and accounted for the effect of S_h on mechanical strength and stiffness. The extension of MC type models to deal with hydrates is generally carried out by incorporating a dependency of the cohesion with the hydrate concentration (i.e. (Klar et al., 2010; S Pinkert & Grozic, 2014; Rutqvist & Moridis, 2007)). However, Pinkert 2016 showed that by using the Rowe's stress-dilatancy theory (Rowe, 1962), it was possible to model the behavior of hydrates without the need of enhancing the cohesion with the increase of S_h. As it is well-known, MC type models cannot capture plastic deformations before failure and are unable to simulate positive (compressive) plastic deformations.

The model based on the Modified Cam-Clay (MCC) framework proposed by Sultan and Garziglia (Sultan & Garziglia, 2011) was validated against the experimental data reported by Masui et al. (Masui et al., 2005; Masui et al., 2008). This model was calibrated against experimental data gathered from triaxial tests on synthetic hydrate sediments(Masui et al., 2005). The global performance of the model was satisfactory. However, it was unable to capture the softening behavior observed in these experiments. The critical state model for GHBS proposed by Uchida et al. (2012, 2016) is based on the MCC model and its validation was performed using published experiments conducted at constant hydrate saturation. Lin et al. (2015) developed a critical state model based on the 'spatial mobilized plane' framework and sub-loading concepts. The performance of this model was satisfactory when compared against triaxial test data from laboratory-synthesized samples and also from field specimens extracted from Nankai Trough, Japan (Masui et al., 2005; Masui et al., 2008). Kimoto et al. (Kimoto et al., 2007) proposed an elasto–viscoplastic model to analyze ground deformations induced by hydrate dissociation. The discrete element method has also been used to simulate the mechanical behavior of GHBS (e.g.,(Jiang et al., 2014; Jiang et al., 2015; Liu et al., 2014; J. Shen et al., 2016; Shen & Jiang, 2016; Z. Shen et al., 2016; Yu et al., 2016)). All the mechanical models discussed above have been used to simulate tests performed at constant hydrate saturation.

2.4 Discussion

The mechanical behavior of GHBS is highly complex because its response not only depends on the amount of hydrate, but also on the type of pore habit (i.e., cementing, pore-filling, or load-bearing s). It was observed that the behavior of GHBS during hydrate dissociation (and after it) depends on stress level. It has also been suggested that hydrate bonding effects can be damaged during shearing (J. Lin et al., 2015; S Uchida et al., 2012; Shun Uchida et al., 2016). The progressive stiffness degradation in tests involving GHBS is generally very evident. Figure 2-4a illustrates the phenomenon of hydrate damage during shearing. Hydrate dissociation is also accompanied by profound changes in the sediment structure. Figure 2-4b shows schematically the expected changes in the soil structure that lead to the collapse compression deformations observed during dissociation under normally consolidated conditions (e.g., Figure 2-3b). To summarize, the mechanical response of GHBS is highly non-linear, controlled by multiple inelastic phenomena that depends on hydrate saturation, sediment structure, and stress level. In the following section, two advanced constitutive mechanical models for GHBS are presented. The advantages compared with previous models are analyzed in detail through modeling experimental test.

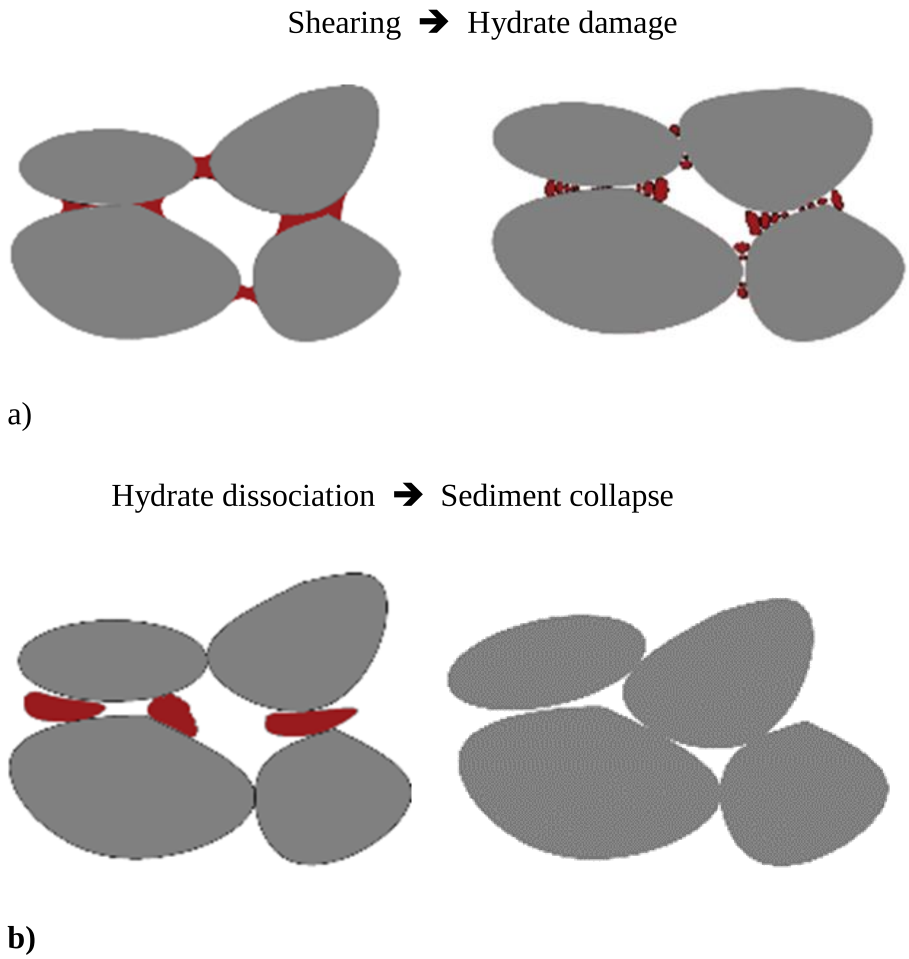

Figure 2-4 a) Schematic representation of the hydrate damaged during shearing; b) rearrangement of the GHBS structure upon dissociation

3 HIERARCHICAL CRITICAL STATE MODEL

3.1 Introduction

The constitutive model for HBS presented here is based on the Hierarchical Single Surface (HISS) framework (Desai, 1989; Desai, 1995). Some key ingredients proposed by Uchida et al. (2012) to deal with particular features of GHBS are incorporated into the model, namely: sub-loading concepts (Hashiguchi, 1977); cementing effects associated with the presence of hydrates; and bonding damage. The resulting approach is called hereafter Hierarchical Single Surface -Methane Hydrate (HISS-MH) model.

3.2 Model description

The HISS-MH model involves a single and continuous yield surface, which can have different shapes depending on the adopted parameters. The HISS yield surface (*F*) is expressed as:

$$F = \frac{a}{3M^2} q^2 - \gamma 3^2 p'^2 + \gamma 3^2 p'^n \, p_c^{\,2-n} \tag{3-1}$$

where a and γ are constants; n is the parameter related to the transition from compressive to dilative volume change; p' and q are the mean effective and deviatoric stresses, respectively; M is the slope of critical line in the q-p' space (Figure 3-1); p_c is the effective pre-consolidation pressure.

An advantage of the HISS is its flexibility to adapt the shape of the yield surface to the particular conditions of the soil under investigation by modifying three parameters (a, γ and n). Figure 3-1 shows some of the possible yield surfaces that can be adopted with this model, and Table 3-1 presents the corresponding parameters. Note that the Modified Camclay Model (MCC) yield surface corresponds to a particular case of this model.

Table 3-1 Different shape of yield surface

Parameters	YS1 (MCC)	YS2	YS3	YS4
a	3	3	3	3
n	1	3	5	1
γ	-1/9	1/9	1/9	-0.15

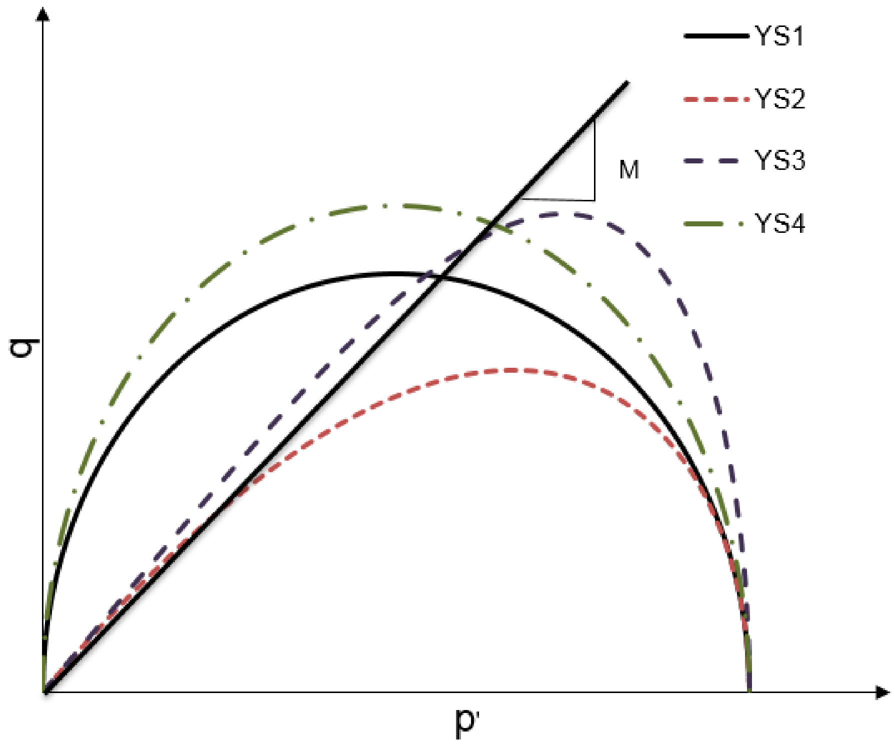

Figure 3-1 Different HISS yield surface options

As in other typical soil mechanic models, the increment of the elastic volumetric strains depend directly on the increment of the mean effective stress (*p'*) through the stress-dependent elastic soil bulk modulus *K':*

$$K' = \frac{v}{\kappa} p' \tag{3-2}$$

where v is the specific volume (v =1+*e*, where *e* is the void ratio); and κ is the slope of the unloading/reloading line in the *e-log(p)'* space. Deviatoric elastic strains and stresses relate through the shear modulus (G_s). It is also assumed that the hardening law is isotropic and depends on the plastic volumetric strains (ε_v^p) through:

$$\frac{dp_c}{p_c} = \frac{v}{\lambda - \kappa} d\varepsilon_v^p \tag{3-3}$$

where λ is the slope of the normal compression line in the *e-log(p)'* space. For the sake of the simplicity, an associated flow rule is assumed in this paper (i.e. *F* coincide with the plastic potential *G*), so the flow rule can be written as:

$$d\boldsymbol{\varepsilon}^p = \Lambda \frac{\partial G}{\partial \boldsymbol{\sigma}'} = \Lambda \frac{\partial F}{\partial \boldsymbol{\sigma}'} \tag{3-4}$$

where Λ is the plastic multiplier and $\boldsymbol{\sigma}'$ is the effective Cauchy's stress tensor.

An additional mechanism is added to the HISS model to account for the increase of strength and dilation observed in hydrate bearing sediments. This phenomenon can be associated with the cementing effects induced by the hydrates in the pore structure (Uchida et al., 2012). This mechanism will induce an isotropic expansion of the yield surface, with the related enhancement of the sediment strength (Figure 3-2). The relationship adopted in this paper is based on the empirical equations proposed by Uchida et al. (2012) as an evolution law in terms of a hardening variable (p_d), as follows:

$$p_d = \alpha \left(\chi \ S_H \right)^{\beta} \tag{3-5}$$

where p_d controls the increase of the sediment strength associated with the presence of hydrates; α and β are constants that describe the degree of hydrate contribution to the hardening law; χ is a damage factor that varies between 1 (maximum bonding effect provided by the hydrate) and 0 (no bonding effect). It is also assumed that the strength enhancement can be degraded during yielding. This degradation effect is incorporated by defining the following evolution law for χ.

$$d\chi = -\mu \ \chi \ d\varepsilon_q^p \tag{3-6}$$

where μ is a parameter that defines the rate of mechanical damage and $d\varepsilon^p{}_q$ is the plastic deviatoric strain.

The proposed model is able to account for different hydrate morphologies by defining different values of α, β, and μ. The parameter α can be used to consider the effect of hydrate morphology in the modeling, parameter β to account for the effect of hydrate saturation, and parameter μ to simulate rate of bonding degradation. More details about these model parameters are presented at the end of this Section and in the application cases.

The yield function of the HISS-MH model incorporating the strength enhancement effects related to the presence of methane hydrate can be written as:

$$F = \frac{a}{3M^2} q^2 - \gamma 3^2 p'^2 + \gamma 3^2 p'^n (p_c + p_d)^{2-n} \tag{3-7}$$

Sub-loading concepts are introduced in the model formulation to improve two main aspects: i) to simulate irrecoverable strains that may occur when the stress state is inside the yield surface (aspect that cannot be modeled with a standard elasto-plastic model), and ii) to predict a smooth transition between elastic and plastic states, particularly in soils that exhibit dilatancy (as it is well-known, conventional critical state model predicts a sharp transition in those cases, that is not very representative of the actual soil behavior). According to Hashiguchi (1989), the sub-loading surface ratio *R* (with $0 < R \leq 1$) can be incorporated in the definition of the yield surface, leading to:

$$F = \frac{a}{3M^2} q^2 - \gamma 3^2 p'^2 + \gamma 3^2 p'^n \left[\mathrm{R}(p_c + p_d)\right]^{2-n} \tag{3-8}$$

where the changes in *R* are defined through the following evolution law:

$$\mathrm{dR} = -\eta \ln \mathrm{R} \left| d\boldsymbol{\varepsilon}^p \right| \tag{3-9}$$

where $|d\varepsilon^p|$ is the norm of the (total) plastic strain vector and η is a sub-loading parameter associated with any plastic deformations that may develop inside initial yield surface. The sub-loading surface is sketched in Figure 3-2. Through this plastic mechanism, it is possible to model the irreversible strains generally observed when the stress state is inside the yield surface and also to introduce a smooth transition between elastic and plastic conditions.

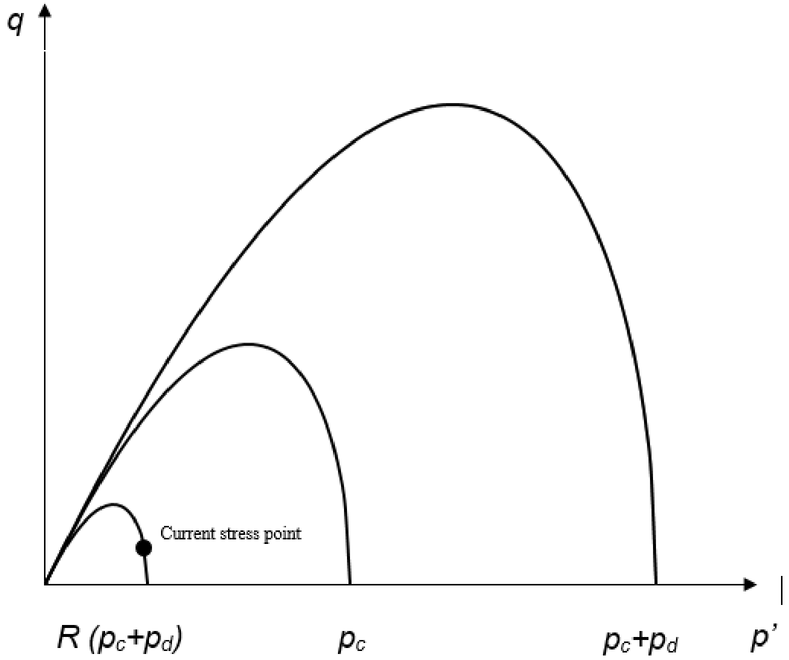

Figure 3-2 Yield surfaces incorporating sub-loading concepts

To ensure that the stress state remains on the yield surface during yielding the consistency condition is enforced:

$$dF = \frac{\partial \mathrm{F}}{\partial \boldsymbol{\sigma}'} : d\boldsymbol{\sigma}' + \frac{\partial F}{\partial \mathrm{p}_c} d\mathrm{p}_c + \frac{\partial \mathrm{F}}{\partial \mathrm{p}_d} d\mathrm{p}_d + \frac{\partial \mathrm{F}}{\partial \mathrm{R}} d\mathrm{R} \tag{3-10}$$

By substituting the flow rule Eq. (3-4) into the consistency condition Eq. (3-10), the plastic multiplier can be expressed as:

$$\Lambda = \frac{\dfrac{\partial \mathrm{F}}{\partial \boldsymbol{\sigma}'} : d\boldsymbol{\sigma}' + \dfrac{\partial \mathrm{F}}{\partial \mathrm{p}_d} \alpha\ \beta\left(\chi\ S_H\right)^{\beta-1} \chi\ dS_h}{\dfrac{\partial \mathrm{F}}{\partial \mathrm{p}_c} \dfrac{v}{\lambda - \mathrm{k}} p_c \dfrac{\partial \mathrm{F}}{\partial \mathrm{p}} + \dfrac{\partial \mathrm{F}}{\partial \mathrm{p}_d} \alpha\beta\left(-\mu\right)\left(\chi\ S_h\right)^{\beta} \dfrac{\partial \mathrm{F}}{\partial \mathrm{q}} + \dfrac{\partial \mathrm{F}}{\partial \mathrm{R}}\left(-\eta\right)\ln\mathrm{R}\left|\dfrac{\partial F}{\partial \boldsymbol{\sigma}'}\right|} \tag{3-11}$$

The effective stress-strain relationship can be obtained after multiplying the elastic constitutive matrix (**D**^{e})De time the elastic strains; which in turns can be obtained as the difference between the total and the plastic strains, as follows:

$$d\boldsymbol{\sigma}' = \mathbf{D}^e \left(d\boldsymbol{\varepsilon} - \Lambda \frac{\partial \mathrm{F}}{\partial \boldsymbol{\sigma}'} \right) \tag{3-12}$$

After some algebra, the constitutive relationship can be expressed as:

$$d\boldsymbol{\sigma}' = \mathbf{D} d\boldsymbol{\varepsilon} + \mathbf{D}_{s_h} dS_h \tag{3-13}$$

where:

$$\mathbf{D} = \left[\mathbf{D}^e - \frac{\mathbf{D}^e \dfrac{\partial \mathrm{F}}{\partial \boldsymbol{\sigma}'} \left(\dfrac{\partial \mathrm{F}}{\partial \boldsymbol{\sigma}'} \right)^T \mathbf{D}^e}{\left(\dfrac{\partial \mathrm{F}}{\partial \boldsymbol{\sigma}'} \right) \mathbf{D}^e \dfrac{\partial \mathrm{F}}{\partial \boldsymbol{\sigma}'} + \dfrac{\partial \mathrm{F}}{\partial \mathrm{p}_c} \dfrac{v}{\lambda - \mathrm{k}} p_c \dfrac{\partial \mathrm{F}}{\partial \mathrm{p}} + \dfrac{\partial \mathrm{F}}{\partial \mathrm{p}_d} \alpha\beta(-\mu)(\chi\ S_h)^{\beta} \dfrac{\partial \mathrm{F}}{\partial \mathrm{q}} + \dfrac{\partial \mathrm{F}}{\partial \mathrm{R}} (-\eta) \ln \mathrm{R} \left| \dfrac{\partial F}{\partial \boldsymbol{\sigma}'} \right|} \right] \tag{3-14}$$

$$\mathbf{D}_{S_H} = \left[\mathbf{D}^e \frac{\dfrac{\partial \mathrm{F}}{\partial \mathrm{p}_d} \alpha\beta(\chi S_h)^{\beta-1} \chi}{\dfrac{\partial \mathrm{F}}{\partial \mathrm{p}_c} \dfrac{v}{\lambda - \mathrm{k}} p_c \dfrac{\partial \mathrm{F}}{\partial \mathrm{p}} + \dfrac{\partial \mathrm{F}}{\partial \mathrm{p}_d} \alpha\beta(-\mu)(\chi S_h)^{\beta} \dfrac{\partial \mathrm{F}}{\partial \mathrm{q}} + \dfrac{\partial \mathrm{F}}{\partial \mathrm{R}} (-\eta) \ln \mathrm{R} \left| \dfrac{\partial F}{\partial \boldsymbol{\sigma}'} \right|} \right] \tag{3-15}$$

For the sake of the completeness, the influence of temperature on the description of the sediment behavior is added, the Eq. (3-13) can be extended to consider thermomechanical effect as follows (Uchida et al., 2012):

$$d\boldsymbol{\sigma}' = \mathbf{D} d\boldsymbol{\varepsilon} + \mathbf{D}_{Sh} dS_h + \frac{\partial \boldsymbol{\sigma}'}{\partial T} dT \tag{3-16}$$

The temperature-dependent behavior of methane hydrate sediments (e.g. Hyodo et al. 2005) was considered through the following equation:

$$\frac{\partial \boldsymbol{\sigma}'}{\partial T} dT = (1-n_p)\beta_T K' \boldsymbol{\delta} dT = \mathbf{D}(1-n_p)\beta_T \frac{\boldsymbol{\delta}}{3} dT \tag{3-17}$$

where n_p is porosity, β_T is the thermal expansion coefficient of hydrate sediment and $\boldsymbol{\delta}$ is the Kronecker's delta vector $(1,1,1,0,0,0)^T$.

The mechanical behavior of GHBS is very complex and depends on a number of factors, amongst others, stress level, stress history, hydrate concentration, and hydrate morphology. Therefore, an advanced elasto-plastic model with several evolution laws and parameters (as the one presented above) is generally required to capture the main features of sediment behavior observed in the lab/field. Some of the model parameters can be directly determined from experiments, but some others require an indirect estimation by fitting experimental observations. The procedure followed in this study to obtain the model parameters is briefly discussed below.

The first step is to determine the parameters associated with the 'hydrate-free' sediment. An elastoplastic critical state model was adopted in this work, therefore the determination of the model parameters (i.e. κ, λ, Gs, p_o, and M) follows the typical procedure used in soils mechanics for this type of model. The only difference here is that the HISS yield surface and plastic potential were adopted. Considering that the MCC is a particular case of the HISS model, the procedure followed hereafter was to determine firstly the parameters associated with MCC. If the MCC response is satisfactory, there is no need to change the model and the MCC is adopted to describe the behavior of the pure sediment. However, if the MCC performance is not optimal or acceptable, the advantage of the HISS model flexibility was taken to adapt the shape of the yield surface or plastic potential to enhance the model performance. An example of how this can be done is presented in Case 2 below (i.e. Section 3.3.2).

The parameters related to the effect of hydrates on sediment behavior are a bit more difficult to determine. The model incorporates evolution laws capable of considering in the (macroscopic) modeling, aspects related to the GHBS structure (as e.g. S_h and pore habit). Eq. 3-5 encompasses two parameters, α and β, plus a variable χ, which in turns depend on the parameter μ through Eq.3-6. These parameters are associated with the increase of preconsolidation pressure and sediment strength with the presence of gas hydrates. Parameters β and μ can be used to account for the effect of S_h on GHBS response (i.e. for a given hydrate morphology), and the parameter α can be used to model the effect of pore habit (i.e. for a given S_h). For example, in the analysis presented in this paper a fix value of β was assumed for all the simulations (i.e. β=1.6). The effect of S_H in HBS behavior (i.e. Cases 3.3.2 and 3.3.3) was considered by means of the parameter μ and the parameter α was used to account for the effect of hydrate morphology (i.e. Case 3.3.1). The parameter μ also controls the rate of mechanical damage. It was considered that the rate of mechanical damage increases with S_h, and it was also assumed that for the cementing morphology the rate of damage is higher than the pore-filling one. Generally, these parameters cannot be directly determined from experiments, and a number of tests (ideally three or more) are necessary to estimate them indirectly. The Case 3.3.3 shown how some tests can be used to estimate the model parameters (i.e. by back-analyzing the experimental data) and other tests can be used to validate the predicting capabilities of the proposed approach (i.e. by using the previously determined parameters).

An additional issue associated with the selection of model parameters for GHBS is that the available data base is quite limited (at least when compared with the information existent for other types of soils and rocks). It is anticipated that as more experimental evidence become available and more insight on the behavior of GHBS is gained, a better estimation of model parameters could be achieved.

3.3 Model application

The performance of the model presented in Section 3.2 was evaluated against available experimental data involving a variety of tests, some of them published quite recently. The stress integration method proposed by (Sloan, 1987) was adapted for the specific characteristics of this model . All the analyses presented in this paper correspond to the ‘point integration level’ type. The model was compared first against tests conducted on synthetic samples prepared at a similar hydrate saturation (i.e. $S_h \sim 0.41$), but with two different type of hydrate pore habits (i.e. pore-filling and cementing forms). The tests were performed at a relatively low confinement (i.e. effective cell pressure $\sigma'_3 \sim 1$ MPa). Then, the capability of the model to reproduce the behavior of natural samples was explored looking at the effect of hydrate saturation at relatively low confinement as well ($\sigma'_3 \sim 1.5$ MPa). In this case, the model results using HISS yield surface were compared against the results obtained from the MCC yield surface to analyze the advantages of the adopted approach. Finally, the model was compared against experimental data gathered from synthetic samples prepared at different hydrate saturation (i.e. from free-hydrate samples to specimens with S_h ~ 53%), and tested at relatively high cell pressures (i.e. σ'_3 ~ 5 MPa). The main analyses are presented in the following Sections.

3.3.1 Case 1-Morphology effect

Masui et al. (2005) conducted several triaxial compression tests using synthetic methane hydrate specimens. The samples containing synthetic methane hydrate were produced from two types of host specimen mixture of Toyoura sand: i) mixture of sand with ice (using the ice-seed method, and ii) mixture of sand with water (using the partial water saturation method). It can be anticipated that the ice-seed method will produce gas hydrates where the pore-filling habit is dominant, and that the partial water saturation method will form hydrates sediments where the cementing habit will be dominant. The sediments formed using these two methods were confined in a triaxial pressure vessel that replicates the pore pressure conditions equivalent to a depth of approximately 800m below the sea. Drained tests were conducted under a constant temperature of 278 °K and an effective confining pressure of 1.0 MPa.

A triaxial compression test using pure Toyoura sand (i.e. with no hydrate) was chosen, plus two more experiments involving synthetic specimens, one of them with hydrate in pore-filling dominating habit and the other one in which the effect of the hydrate was mainly cementing. The porosity (*n*) values reported by Masui et al. (2005) were between 37.7 and 42.4% and the hydrate saturation was practical identical in both tests (i.e., $S_h = 0.409$ for the pore-filling case and $S_h = 0.410$ for the cementing one).

Figure 3-3 shows the stress-strain relationship and volumetric behavior of the selected tests showing with symbols the experiments and with lines the model outputs. A marked increase in the initial stiffness and strength is observed for the pore-filling and cementing samples. It is clear that the enhancement in stiffness, strength and dilatancy is higher in cementing samples. The parameter α was used to account for the effect of hydrate morphology considering that the ‘cementing’ hydrate morphology has a stronger impact on hydrate strength than the ‘pore-filling’ one, and therefore a higher value of α was adopted for the case cementing (i.e. α=42) than for the pore-filling case (i.e. α=22). It is also considered that degradation parameter μ dependents on hydrate morphology. A higher value of μ is associated with a faster degradation of p_d; which is the case of the cementing pore habit. The critical state parameters (such as the slopes of critical state line, normal compression and unloading/reloading lines) are the same for both cases since they are considered independent of hydrate morphology. The response provided by the MCC was considered satisfactory; therefore, it was not needed to change the shape (i.e. ellipse) of the yield surface and plastic potential. The main parameters adopted for the numerical analysis are presented in Table 3-2.

Table 3-2 Model parameters adopted in the modeling

Properties	Pure sand	Pore-filling	Cementing
M	1.07	1.07	1.07
λ	0.16	0.16	0.16
κ	0.004	0.004	0.004
p_c (MPa)	12	12	12
n	1	1	1
a	3	3	3
γ	-1/9	-1/9	-1/9
S_H	0	0.41	0.41
α	-	22	42
β	-	1.6	1.6
μ	-	1.5	3.5
η	15	15	15

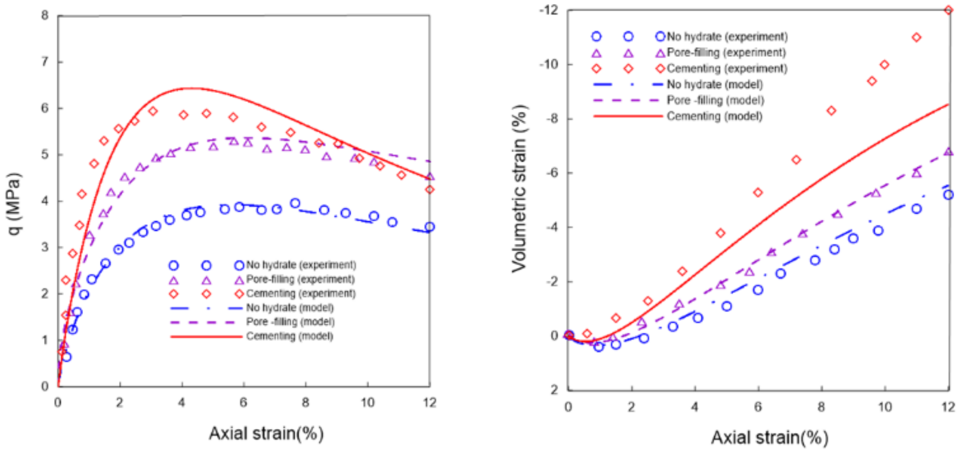

Figure 3-3 Modeling and experimental results: a) stress strain behavior, b) volumetric response. Experimental data from Masui et al. (2005)

It can be observed that the model is able to capture very well the different features of GHBS behavior observed in these experiments, between the pore-filling and cementing specimens, particularly in terms of peak deviatoric stresses. The model also captures well the tendencies observed in terms of soil dilatancy, with slight under-prediction for the case of higher S_h.

3.3.2 Case 2-Natural core sediment

The second set of tests selected to validate the proposed HISS-MH model involves natural hydrate samples studied by (Yoneda et al., 2015). To investigate the mechanical behavior of natural gas-hydrate-bearing sediments, several core samples were extracted from the Eastern Nankai Trough. Two different core-handling methods were adopted in this study, as follows:"LN2 core" and "CH4 purge LN2 core". It should be noted that both methods require the core samples to be depressurized at atmospheric pressure for a short period of time, which might cause hydrate dissociation, thus causing disruptions on the mechanical behavior of the sample.

Core N^o 7 (i.e. LN_2 core method) and N^o 9 (i.e. CH_4 purge LN_2 core method), with hydrate saturation around 38% and 79%, respectively, were tested under triaxial drained conditions. The in-situ hydrate saturation was in the range 65 to 90% for Core N^o 7. However, just before the mechanical test the hydrate saturation was around 38%, this drop in S_h can be associated with handling of the specimen. Moreover, many fractures and cracks were observed in the CT image, which means that the soil structure was affected during its manipulation before testing. For Core N^o 9, the in-situ hydrate saturation was in the range of 70 to 95%, and S_h at test condition was around 79%. Furthermore, no fractures or cracks were observed in the CT scanning of the sample, which suggest that the conditions of the Core N^o 9 just before the test were very close to the in-situ ones. Based on the fact that the state of these two cores were different at the beginning of the tests, the samples were considered as different materials during the modeling. Note that the focus in this Section is on the comparison of MCC and HISS model's performances.

Table 3-3 presents the main soil index properties, alongside with the more relevant in-situ and testing conditions related to these samples and experiments.

Table 3-3 In situ conditions, soil index properties, and testing conditions

Test name	Host type	Effective confining pressure (MPa)	Test condition	Water Content (%)	Porosity	Hydrate saturation S_h (%)
No.7	Silty sand	1.5	CD	26.4	44.1	38
No.9	Silty sand	1.5	CD	22.7	39.4	79

Figure 3-4 presents the experimental stress-strain behavior and volumetric response of the natural hydrate-bearing core samples discussed above (with symbols) together with the model results (with lines). As in other cases, the MCC was initially adopted to reproduce the observed experimental behavior. It is noticeable that the Core N^o 9 (with higher S_h) exhibits a much higher peak strength and a more noticeable enhancement in stiffness and dilatancy than Core N^o 7. Since the dominant soils in both specimens are silty sand and considering that both cores were extracted from almost the same depth and around the same location, it is reasonable to assume the pore habit of these two samples are similar. To model these different responses, it was considered the dependence of μ on hydrate concentration. Considering the high concentration of hydrate in Core N^o 9, it was assumed that this specimen has a higher damage rate on shearing than Core N^o 7, and therefore a higher μ was adopted. Considering two aspects: i) a fix value of β=1.6 was adopted for all the simulations in this paper, and ii) α depends mainly in hydrate pore habit, even though that part of Core N^o 7 might have dissociated during the handling process, the pore habit is assumed to remain the same, thus a unique value of α=12 for Core N^o 7 and Core N^o 9 was adopted.

It is clear that the MCC performance is not very satisfactory in this case. Figure 4-4a&b show that for both hydrate saturations the model under predicts the material strength. As for the volumetric behavior (i.e. Figure 3-4 c & d), the model slightly over-predict sediment dilation. This implies that any change in the parameters controlling the sediment strength and dilation enhancement (i.e. parameters β, and μ), may improve the model prediction in terms of strength, but it will also increase the dilation and softening predictions, up to values that may be not acceptable. Figure 3-4 e & f shows the stress paths for the two tests with the corresponding initial and final MCC yield surfaces

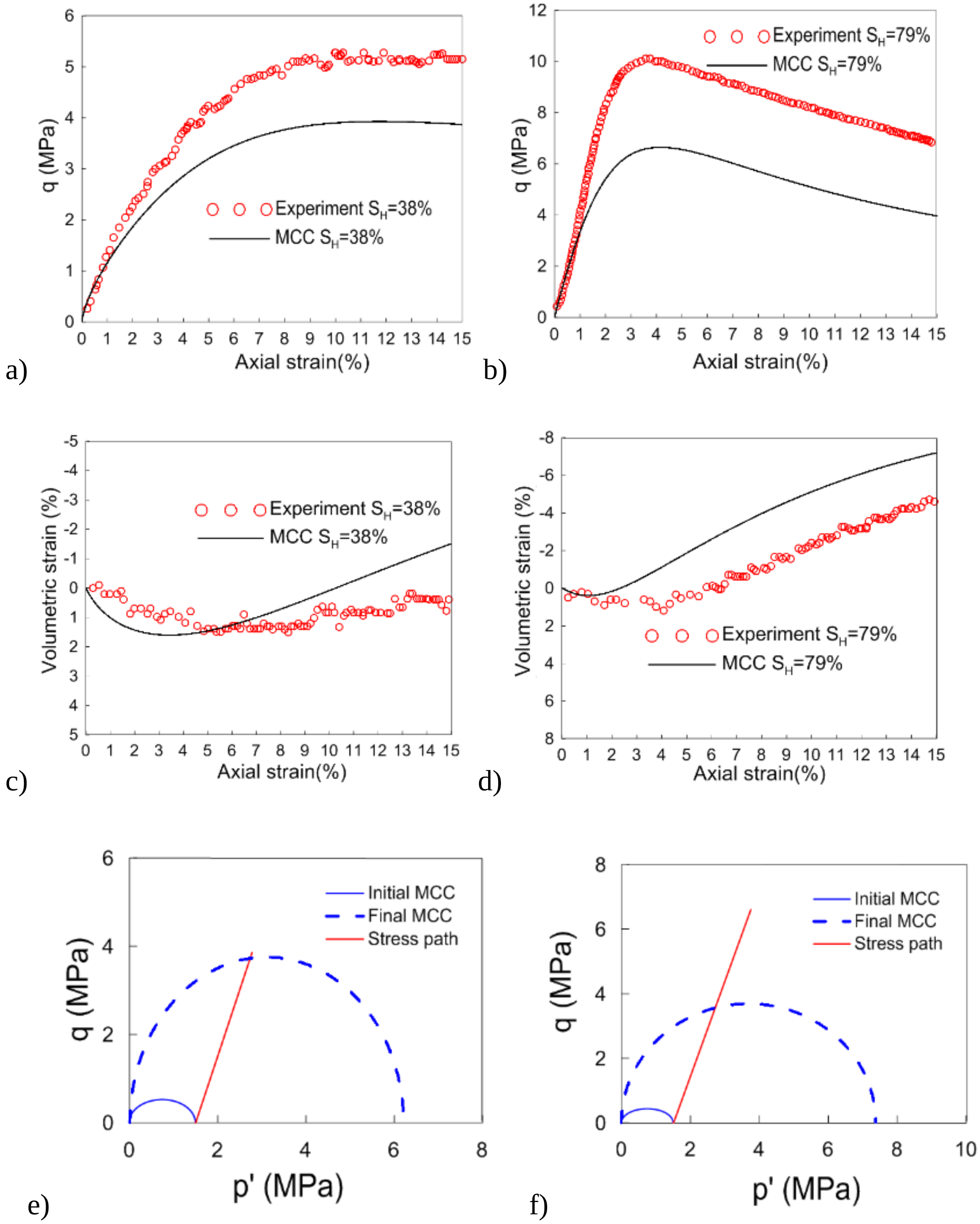

Figure 3-4 Modified Cam-Clay model results: a) stress strain relationship specimen S_h =38%; b) stress strain relationship specimen S_h =79%; c) volumetric response specimen S_h =38%; d) volumetric response specimen S_h =79%; e) stress path and yield surface evolution specimen S_h =38%; and f) stress path and yield surface evolution specimen S_h =79%. Experimental data from (Yoneda et al., 2015)

To improve the model performance, the HISS model flexibility was explored by changing the shape of the yield surface and plastic potential to obtain more satisfactory results. Figure 3-5 shows the initial HISS yield surface suggested for the two cores, together with the MCC ones for comparisons purposes only. Figure 3-6 presents results similar to the ones introduced in Figure 3-4 for the MCC, but in this case for the HISS yield surface. The model performance is evidently more satisfactory in this case, with better perditions in terms of sediment stiffness, strength and softening behavior (i.e.Figure 3-6 a & b) as well as in terms of volumetric behavior (i.e. Figure 3-6 c & d). Table 3-4 lists the parameters adopted in all the simulations. As shown, the HISS-MH model provide enough flexibility to satisfactorily reproduce the mechanical behavior of two natural samples from Nankai Trough.

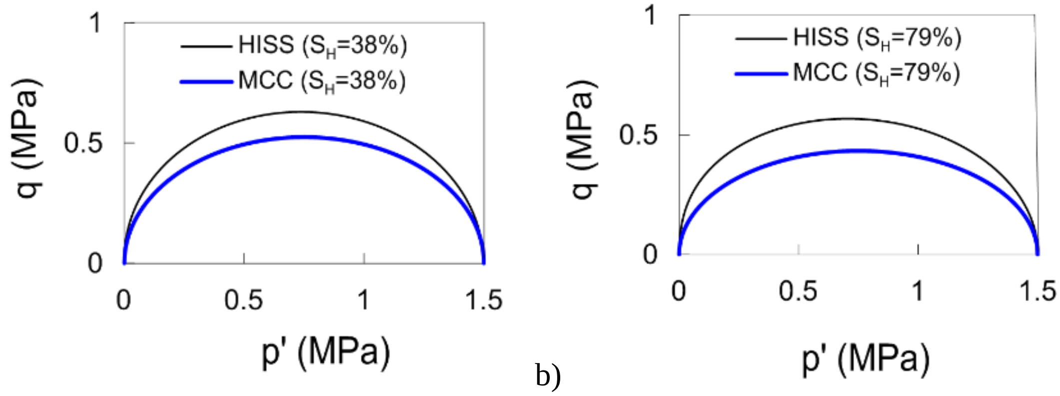

a) b)

Figure 3-5 Initial yield surfaces adopted for MCC and HISS a) specimen S_h 38%; and b) specimen S_h 79%

Table 3-4 Parameter adopted in the modeling

S_h=38%

Properties	HISS	MCC
M	1.21	1.21
λ	0.13	0.13
κ	0.008	0.008
p_c (MPa)	12	12
n	0.95	1
a	3	3
γ	-0.15	-1/9
S_h	0.38	0.38
α	12	12
β	1.6	1.6
μ	1.0	1.0
η	2.7	2.7

S_h=79%

Properties	HISS	MCC
M	1.21	1.21
λ	0.13	0.13
κ	0.008	0.008
p_c (MPa)	12	12
n	0.95	1
a	3	3
γ	-0.15	-1/9
S_h	0.79	0.79
α	12	12
β	1.6	1.6
μ	3.5	3.5
η	28	28

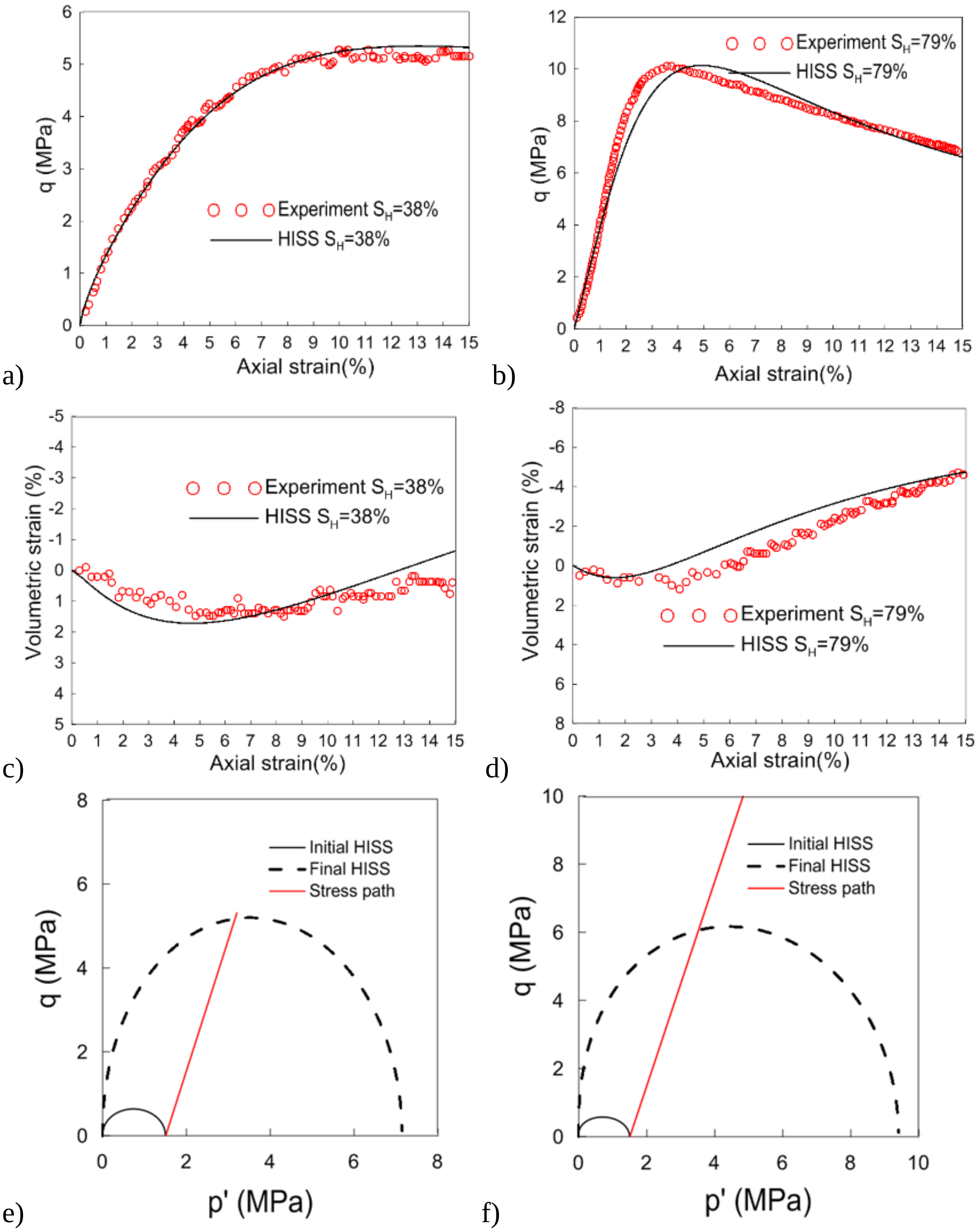

Figure 3-6 HISS model results: a) stress strain relationship specimen S_h =38%; b) stress strain relationship specimen S_h =79%; c) volumetric response specimen S_h =38%; d) volumetric response specimen S_h =79%; e) stress path and yield surface evolution specimen S_h =38%; and f) stress path and yield surface evolution specimen S_h =79%. Experimental data from Yoneda et al. (2015b)

3.3.3 Case 3-Different hydrate saturation

The third and final set of experimental data studied in this research corresponds to the tests reported by Hyodo et al. (2013). They conducted series of triaxial compression tests on synthetic methane hydrate-bearing sand in order to study the mechanical behavior of GHBS. Toyoura sand was chosen as the host material. The global porosity of all the samples were quite similar (n ~ 40%). The following S_h were investigated: 0; 24.2; 35.1; and 53.1 %. The effective confining pressure for all the tests was 5 MPa and the temperature during the experiments was around 5 °C. The main test conditions in this experimental study are summarized in Table 3-5.

Table 3-5 Test conditions for triaxial compression tests

Effective confining pressure (MPa)	**Temperature (C)**	**Porosity (%)**	**Degree of hydrate saturation (%)**
5	5	39.4	0
5	5	39.6	24.2
5	5	39.2	35.1
5	5	40.1	53.1

Figure 3-7 shows the responses of specimens with different hydrate saturations in terms of deviatoric stress (Figure 3-7a), axial and volumetric strains (Figure 3-7b), for samples that where isotropically consolidated first and subjected to shearing afterwards. It is observed that most of specimens shown a dominant compressive volume change and strain hardening behavior at this (relatively high) level of confining pressure. Only the sample with the higher hydrate saturation (i.e., S_h=53.1%) presents a notorious dilative behavior. Also in these tests, a marked increase in the initial stiffness and shear strength is observed with the increase of hydrate saturation of the samples.

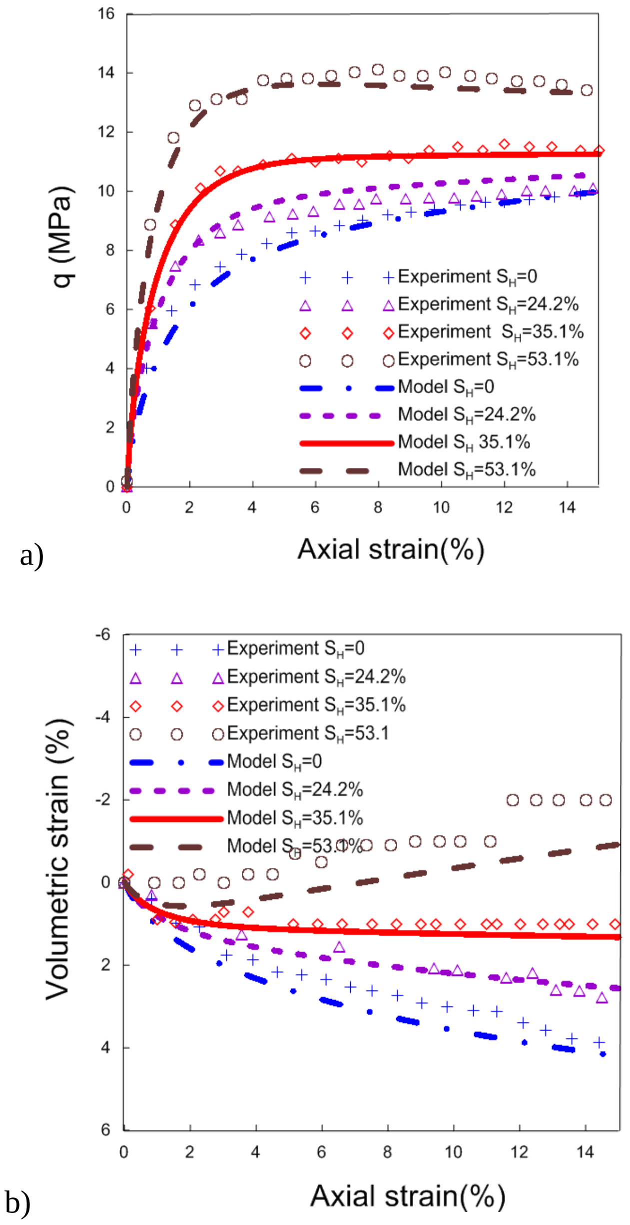

Figure 3-7 Modeling the drained triaxial tests on synthetic samples using the HISS MH model: a) stress strain behavior, b) volumetric response. Experimental data from Hyodo et al. (2013)

The behavior of the pure (free-hydrate) sediment was modeled first using the MCC, but the model performance was not very satisfactory, so a procedure similar to the one explained in Section 4.2 was adopted to find a more convenient yield surface. Afterwards, the sample with S_h =24.2% was modeled and the parameters were determined after back-analyzing the experimental data. Table 3-6 lists the parameters used in the numerical simulations. Finally, the other two experiments (i.e. S_h =35.1% and S_h =53.1%) were used to validate the model by predicting the soil behavior without changing the parameters adopted in the previous stages. The model performance can be considered very satisfactory in these analyses. There is only a slight under-prediction of the dilatant behavior for the specimen prepared at a S_h =53.1%.

Table 3-6 Parameters adopted in the modeling

Properties	**Test 1**	**Test 2**	**Test 3**	**Test 4**
M	1.15	1.15	1.15	1.15
λ	0.18	0.18	0.18	0.18
κ	0.004	0.004	0.004	0.004
$p_c\,(MPa)$	10.0	10.0	10.0	10.0
n	0.95	0.95	0.95	0.95
a	3	3	3	3
γ	-0.13	-0.13	-0.13	-0.13
S_H	0	0.242	0.351	0.531
α	-	31	31	31
β	-	1.6	1.6	1.6
μ	-	1.0	1.0	1.0
η	65	65	65	65

3.4 Conclusion and discussion

In this section, a constitutive model for hydrate bearing soil was presented. The core of the proposed model includes: a HISS critical state framework, sub-loading concepts for modeling the plastic strains generally observed inside the yield surface and a hydrate enhancement factor to account for the cementing effects provided by the presence of hydrates in sediments. The model was developed in the framework of elasto-plastic theory for strain hardening/softening soils, incorporating bonding and damage effects. The formal full mathematical framework was presented and discussed in detail.

The model performance against published experimental data was also investigated using a variety of available tests, some of them published quite recently. The tests involving different hydrate saturations (i.e., from free-hydrate samples up to S_h=79%), different types of hydrate pore habits (i.e., pore filling and cementing morphologies) and different range of confinement conditions (i.e. σ'_3 from 1 MPa up to 5 MPa). It was observed that the model was able to reproduce quite satisfactorily the enhanced stiffness and strength induced by the presence of methane hydrate in the sediment pore space, as well as the soil dilatancy observed in the triaxial experiments. The model was also capable of capturing the difference in the mechanical response associated with different S_h values and also with the type of hydrate morphology. This model also performs well under different ranges of confining pressure. Under low confining conditions, it was observed that the hydrate sediment behaved mainly as a strain softening material, with a marked dilatant behavior. While at higher confinements, the GHBS samples tended to act mainly as a strain hardening material, with contraction under shearing loads, this response was particularly true for samples with not very high hydrate saturation (i.e. $S_h < 35\%$). In spite of some minor issues, it can be considered that the global response of the HISS-MH model was satisfactory under the variety of GHBS types test conditions considered in this study.

4 ADVANCED GHBS MODEL WITH STRESS-PARTITION

4.1 Introduction

In this section, a more advanced constitutive model based on critical state and stress-partition framework is presented. The stress-partition concept proposed by Pinyol et al. (Pinyol Puigmartí et al., 2007) for clayed cementing materials is adapted for describing the behavior of GHBS. The main reason behind the selection of this model is that it is extremely well suited to deal with materials that have two main constituents (i.e. ‘hydrates’ and ‘sediments’ in this case), feature that is not considered in the previous model HISS-MH model in section 3. The model allows to explicitly define specific constitutive models and evolutions laws for each one of those two compounds with the corresponding variables. The modeling of the hydrates can be well represented by a damage model that is able to account for the material degradation induced by loading and hydrate dissociation. As for the sediment skeleton, a model based on critical state soil mechanics concepts is adopted, which is an appropriate approach for describing the elastoplastic behavior of the soils. The particular constitutive equations adopted hereafter are based on a modification of the HISS elasto-plastic model (C. Desai, 1989; C. Desai et al., 1986; C. S. Desai, 2000; Gai & Sancehz, 2016; Gai & Sánchez, 2017; Sanchez & Gai, 2016; Xuerui & Marcelo, 2017). The proposed framework also incorporates sub-loading and dilation enhancement concepts.

Therefore, the proposed model takes in account two basic aspects related to the presence of hydrates in soils: i) it considers that hydrates contribute (together with the soil skeleton) to the mechanical stability of the sediment, the stress partition concept is used to compute this contribution; and ii) it contemplates that the presence of hydrates alters the mechanical behavior of sediments (e.g., providing hardening and dilation enhancement effects), inelastic mechanisms are incorporated into a critical state model for the sediment to account for these effects.

4.2 Model description

The main model components and its mathematical formulation are detailed below, introducing firstly some basic relationships, detailing afterwards the specific constitutive models for the hydrates and sediment, and developing finally the global stress-strain equations.

4.2.1 Basic relationships

The stress-partition concept (Pinyol Puigmartí et al., 2007) was adopted to develop the basic relationships. The total volume of the sample (V) can be computed as:

$$V = V_s + V_h + V_f \tag{4-1}$$

where V_s is the volume of sediment skeleton, V_h is the volume of hydrate, V_f is the volume occupied by the fluid in the pore space (Figure 4-1).

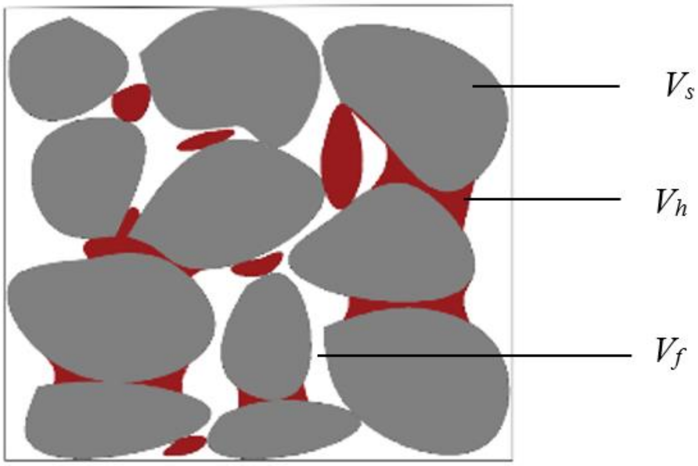

Figure 4-1 Schematic representation of GHBS

Assuming that the soil grains are incompressible, the total volumetric strain can be defined as:

$$\varepsilon^{v} = -\frac{\Delta V_f}{V} - \frac{\Delta V_h}{V} \tag{4-2}$$

where the superscript *v* indicates volumetric strains. The volumetric strain of methane hydrate is computed as:

$$\varepsilon_h^{v} = -\frac{\Delta V_h}{V_h} \tag{4-3}$$

The deformation of hydrate can be defined locally through the following relationship:

$$-\frac{\Delta V_h}{V} = -\frac{\Delta V_h}{V_h}\frac{V_h}{V} = \varepsilon_h^{v} C_h \tag{4-4}$$

where C_h is the volumetric concentration of methane hydrate; which in turns is equal to the porosity (ϕ) times the hydrate saturation (i.e., $C_h = \phi S_h$). From equations (4-

2) and (4-4), the total volumetric strain accounting for both the sediment skeleton (i.e., subscript *ss*) and the hydrates deformations can be calculated as:

$$\varepsilon^{v} = \varepsilon_{ss}^{v} + C_h \varepsilon_h^{v} \tag{4-5}$$

In a similar fashion, the deviatoric strains can be computed as:

$$\varepsilon^{q} = \varepsilon_{ss}^{q} + C_h \varepsilon_h^{q} \tag{4-6}$$

The relationships that link hydrates and soil skeleton strains are proposed following an approach similar to (Pinyol Puigmartí et al., 2007):

$$\varepsilon_h^{v} = \chi \varepsilon_{ss}^{v} \tag{4-7}$$

$$\varepsilon_h^{q} = \chi \varepsilon_{ss}^{q} \tag{4-8}$$

where χ is the strain partition variable that evolves during loading. The evolution law for this variable is presented in Section 4-2-2. From these equations, it can be anticipated that when the sediment skeleton deforms, the local hydrate strain reduces if χ decreases. Combining equations (4-5), (4-6), (4-7) and (4-8) leads to:

$$\varepsilon_h^{v} = \frac{\chi}{1 + C_h \chi} \varepsilon^{v} \tag{4-9}$$

$$\varepsilon_h^{q} = \frac{\chi}{1 + C_h \chi} \varepsilon^{q} \tag{4-10}$$

Equations (4-9) and (4-10) can also be written as a vector:

$$\boldsymbol{\varepsilon}_h = \frac{\chi}{1 + C_h \chi} \boldsymbol{\varepsilon} \tag{4-11}$$

In the following sections, the specific constitutive models for the hydrate and sediment skeleton are discussed.

4.2.2 Constitutive model for hydrate

The damage theory is an appropriate framework to describe the degradation process of geomaterials subjected to loading (Kachanov & Krajcinovic, 1987). Isotropic scalar damage models track the degradation behavior of materials via damage variables. Loading degradation occurs when the stress state arrives to a predefined threshold. As mentioned above, previous studies suggested that hydrate can be damaged during shearing (J. Lin et al., 2015; S Uchida et al., 2012; Shun Uchida et al., 2016). It is also assumed here that the material degradation takes place during hydrate dissociation. When the stresses are below a pre-established threshold, a linear elastic response of the material is assumed via the following relationships:

$$\boldsymbol{\sigma}_h = \mathbf{D}_{h0}\boldsymbol{\varepsilon}_h \tag{4-12}$$

where $\boldsymbol{\sigma}_h$ corresponds to the stresses taken by the hydrate and $\mathbf{D}_{h0}$ is the methane hydrate elastic constitutive matrix of the intact material, as follows:

$$\mathbf{D}_{h0} = \begin{bmatrix} K_{h0}+\frac{4}{3}G_{h0} & K_{h0}-\frac{2}{3}G_{h0} & K_{h0}-\frac{2}{3}G_{h0} & 0 & 0 & 0 \\ & K_{h0}+\frac{4}{3}G_{h0} & K_{h0}-\frac{2}{3}G_{h0} & 0 & 0 & 0 \\ & & K_{h0}+\frac{4}{3}G_{h0} & 0 & 0 & 0 \\ & \mathit{Symetric} & & G_{h0} & 0 & 0 \\ & & & & G_{h0} & 0 \\ & & & & & G_{h0} \end{bmatrix} \tag{4-13}$$

where K_{h0} and G_{h0} are the bulk and shear moduli, of the intact hydrate, respectively. A logarithmic isotropic damage variable ($L: +\infty > L \geq 0$) is introduced to account for the damage induce by loading (Fernandez & Santamarina, 2001). The following expressions can be adopted for damaged states:

$$\boldsymbol{\sigma}_h = e^{-L}\mathbf{D}_{h0}\boldsymbol{\varepsilon}_h = \mathbf{D}_h\boldsymbol{\varepsilon}_h \tag{4-14}$$

where $\mathbf{D}_h$ is the methane hydrate constitutive matrix.

It is assumed that the material damage and the subsequent changes in L can be related to the variation in the energy (per unit of volume) stored in the hydrates (Carol et al., 2001)). This energy can be defined as the elastic secant energy that would be recovered upon unloading; which, e.g. for triaxial conditions, can be written as:

$$u_h = \frac{1}{2}\left(p_h\varepsilon_h^v + q_h\varepsilon_h^q\right) \tag{4-15}$$

The hydrate damage locus is defined by a threshold value 'r_0' of the secant elastic energy that can be represented by an ellipse in the 'p_h-q_h' space. The hydrate stiffness remains constant when the stresses are inside that ellipse. Loading damage takes place when the changes in the stress state is such that the secant elastic energy reaches r_0. During damage, the associated variable L increases, inducing a reduction of the material stiffness. The damage evolution is determined by means of the function below (Pinyol Puigmartí et al., 2007):

$$r_{(L)} = r_0 e^{r_1 L} = u_h \tag{4-16}$$

The damage rate is controlled by r_1. The consistency condition is adopted for defining the evolution law for L (Pinyol Puigmartí et al., 2007). The following evolution law for the partition variable is adopted:

$$\chi = \chi_0 e^{-\frac{L}{2}} \tag{4-17}$$

where χ_0 is an initial reference value assumed for the partition variable.

4.2.3 Constitutive model for the sediment skeleton

Similar to the HISS-MH model, the constitutive model for the soil skeleton is also based on a modified HISS framework. The constitutive equation incorporates sub-loading concepts, as well as hardening and dilation enhancement mechanisms associated with the presence of hydrates in the sediments. The modified HISS model involves a single and continuous yield surface that can adopt different shapes depending on the selected parameters (C. Desai, 1989; C. Desai et al., 1986; C. S. Desai, 2000). The HISS yield surface (F) is given by:

$$F = \frac{a}{3M^2} q_{ss}{}^2 - 9\gamma\left[\left(p'_{ss}\right)^2 - \left(p'_{ss}\right)^n p_c{}^{2-n}\right] \tag{4-18}$$

where a and γ are model constants; n is the parameter related to the transition from compressive to dilative behavior; p'_{ss} and q_{ss} are the mean effective and deviatoric stresses, respectively, both associated with the sediment skeleton; M is the slope of critical line in the q_{ss}-p'_{ss} space; and p_c is the effective pre-consolidation pressure.

The mean effective stress (p'_{ss}) and the elastic volumetric strains are related through the stress-dependent elastic sediment bulk modulus K'_{ss}:

$$K_{ss}^{'} = \frac{v}{\kappa} p_{ss}^{'} \tag{4-19}$$

where v is the specific volume; and κ is the slope of the unloading/reloading curve in the void ratio (e) versus $log(p'_{ss})$ space. The sediment-skeleton shear modulus (G_{ss}) relates the deviatoric elastic strains with the deviatoric stresses.

An isotropic strain hardening behavior in terms of the plastic volumetric deformation (ε^{vp}) is adopted:

$$\frac{dp_c}{p_c} = \frac{v}{\lambda - \kappa} d\varepsilon^{vp} \tag{4-20}$$

where λ is the slope of the normal compression line in the $e\text{-}log(p'_{ss})$ plane. It has assumed that the yield surface F and the plastic potential G coincide (i.e. associated plasticity). A non-associated flow rule can be easily incorporated if necessary.

$$d\boldsymbol{\varepsilon}^{p} = \Lambda \frac{\partial G}{\partial \boldsymbol{\sigma}_{ss}^{'}} = \Lambda \frac{\partial F}{\partial \boldsymbol{\sigma}_{ss}^{'}} \tag{4-21}$$

where Λ is the plastic multiplier and $\boldsymbol{\sigma}_{ss}^{'}$ is the effective Cauchy's stress tensor.

The isotropic expansion of the yield surface is controlled by the hardening parameter 'p_d'. Based on (S Uchida et al., 2012), the influence of hydrates in this law is considered as:

$$p_d = \alpha \left(\chi C_h \right)^{\beta} \tag{4-22}$$

where α and β are constants that describe the degree of hydrate contribution to the hardening law. In all the analyses conducted in this work, a good agreement with the experimental data was obtained when β=1, therefore this parameter could be excluded from the formulation, however it was kept providing more flexibility to model in case is necessary. Also, previous works adopted a similar expression for p_d. Note that the presence of hydrate is also accounted when modeling the soil skeleton because of the profound impact of hydrates on sediment matrix behavior. Equation (4-22) considers that once the hydrates fully dissociate, the behavior of the pure soil skeleton is recovered. The partition parameter χ (Eq. 4-17) accounts for the effect of hydrate degradation on the preconsolidation pressure and it also provides a link between the damage law for the hydrates and the critical state model for the solid skeleton. The yield function (YF) incorporating the strength enhancement associated with the presence of methane hydrate can be expressed as:

$$F_b = \frac{a}{3M^2} q_{ss}{}^2 - 9\gamma \left[\left(p'_{ss} \right)^2 - \left(p'_{ss} \right)^n (p_c + p_d)^{2-n} \right] \tag{4-23}$$

where F_b corresponds to an external (limit) surface, called hereafter boundary yield surface. This surface coincides with F when the effect of hydrates on the sediment matrix vanishes because of hydrate dissociation or damage.

To account for inelastic deformations that may occur inside the bounding yield-surface sub-loading concepts are incorporated into the model formulation. This technique also smooths the transition between elastic and plastic states. Sub-loading concepts were used before with success to model the behavior of GHBS (J. Lin et al., 2015; S Uchida et al., 2012; Shun Uchida et al., 2016). The sub-loading yield surface and the yield surface F, are geometrically similar. The sub-loading surface passes through the present stress state and it evolves during yielding. More details about sub-loading concepts can be found elsewhere (e.g., (Hashiguchi, 1977, 1989)). The modified sub-loading yield surface (F_s) incorporating p_d can be written as:

$$F_s = \frac{a}{3M^2} q_{ss}{}^2 - 9\gamma \left\{ \left(p'_{ss}\right)^2 - \left(p'_{ss}\right)^n \left[R\left(p_c + p_d\right)\right]^{2-n} \right\} \tag{4-24}$$

where R is the sub-loading surface ratio. As suggested by Hashiguchi et al. (Hashiguchi, 1977, 1989), it is assumed that $0 < R \leq 1$. The changes in R are defined through the following evolution law (S Uchida et al., 2012; Shun Uchida et al., 2016):

$$dR = -\eta \ln R \left| d\varepsilon^p \right| \tag{4-25}$$

where $|d\varepsilon^p|$ dεpdεpis the norm of the incremental plastic strain vector and η is a sub-loading parameter that controls the plastic deformations inside F_b. The term between brackets in Eq. (4-24) is called effective hardening parameter (i.e., $H=R(p_c+p_d)$).

The consistency condition is enforced to ensure that the stress state remains on the (sub-loading) yield surface during yielding:

$$dF_s = \frac{\partial F_s}{\partial \boldsymbol{\sigma}'_{ss}} d\boldsymbol{\sigma}'_{ss} + \frac{\partial F_s}{\partial p_c} dp_c + \frac{\partial F_s}{\partial p_d} dp_d + \frac{\partial F_s}{\partial R} dR \tag{4-26}$$

After substituting the flow rule (4-21) into the consistency condition (4-26), the plastic multiplier can be obtained as:

$$\Lambda = \frac{\left(\dfrac{\partial F_s}{\partial \boldsymbol{\sigma}'_{ss}}\right)^T d\boldsymbol{\sigma}'_{ss} + \dfrac{\partial F_s}{\partial p_d} \alpha\beta\chi\left(C_h\right)^{\beta-1} dC_h}{\dfrac{\partial F_s}{\partial p_c}\left(\dfrac{v}{\lambda - k}\right) p_c \dfrac{\partial F_s}{\partial p'_{ss}} + \dfrac{\partial F_s}{\partial R}\left(-\eta\right)\ln R \left|\dfrac{\partial F_s}{\partial \boldsymbol{\sigma}'_{ss}}\right|} \tag{4-27}$$

The constitutive relationship for the sediment skeleton is obtained following the procedure suggested in (Pinyol Puigmartí et al., 2007):

$$d\boldsymbol{\sigma}_{ss}^{'} = \mathbf{D}_{ss} d\boldsymbol{\varepsilon} + \mathbf{d}_{C_h} dC_h \tag{4-28}$$

where:

$$\mathbf{D}_{ss} = \left[\mathbf{D}_{ss}^{e} - \frac{\mathbf{D}_{ss}^{e} \dfrac{\partial F_s}{\partial \boldsymbol{\sigma}_{ss}^{'}} \left(\dfrac{\partial F_s}{\partial \boldsymbol{\sigma}_{ss}^{'}} \right)^{T} \mathbf{D}_{ss}^{e}}{\left(\dfrac{\partial \mathrm{F}_s}{\partial \boldsymbol{\sigma}_{ss}^{'}} \right)^{T} \mathbf{D}^{e} \dfrac{\partial F_s}{\partial \boldsymbol{\sigma}_{ss}^{'}} + \dfrac{\partial F_s}{\partial p_c} \left(\dfrac{v}{\lambda - k} \right) p_c \dfrac{\partial F_s}{\partial p_{ss}^{'}} + \dfrac{\partial F_s}{\partial R} (-\eta) \ln R \left| \dfrac{\partial F_s}{\partial \boldsymbol{\sigma}_{ss}^{'}} \right|} \right] \tag{4-29}$$

$$\mathbf{d}_{C_h} = \left[\mathbf{D}_{ss}^{e} \frac{\dfrac{\partial F_s}{\partial p_d} \alpha \beta \chi \left(C_h \right)^{\beta - 1} \dfrac{\partial F_s}{\partial \boldsymbol{\sigma}_{ss}^{'}}}{\dfrac{\partial F_s}{\partial p_c} \left(\dfrac{v}{\lambda - \mathrm{k}} \right) p_c \dfrac{\partial F_s}{\partial p_{ss}^{'}} + \dfrac{\partial F_s}{\partial R} (-\eta) \ln R \left| \dfrac{\partial F_s}{\partial \boldsymbol{\sigma}_{ss}^{'}} \right|} \right] \tag{4-30}$$

where $\mathbf{D}^{e}_{ss}$ is the sediment skeleton elastic constitutive matrix, with a structure similar to Eq. (4-13) but K'_{ss} (i.e., Eq. (4-19) and G_{ss} are used instead of K_{h0} and G_{h0}, respectively. Equation (4-28) shows the effect of hydrates on effective stress; which in turns affects the mechanical behavior of GHBS. This equation also shows that the effect of hydrates vanishes once they dissociate and the true response of the sediment matrix is recovered.

4.2.4 Final stress-strain relationships

To obtain the expressions relating the external effective stress $\boldsymbol{\sigma}'$ with the two stress components, the principle of virtual work is advocated, which for triaxial conditions can be written as (Pinyol Puigmartí et al., 2007):

$$p' d\varepsilon^{v} + q d\varepsilon^{q} = p'_{ss} d\varepsilon^{v} + q_{ss} d\varepsilon^{q} + p_h C_h d\varepsilon_h^{v} + q_h C_h d\varepsilon_h^{q} \tag{4-31}$$

The following equation is obtained after replacing equations (5-9) and (5-10) into equation (4-31):

$$p' d\varepsilon^{v} + q d\varepsilon^{q} = p'_{ss} d\varepsilon^{v} + q_{ss} d\varepsilon^{q} + p_h C_h \frac{\chi}{1+C_h\chi} d\varepsilon^{v} + q_h C_h \frac{\chi}{1+C_h\chi} d\varepsilon^{q} \tag{4-32}$$

Considering that the equation above is valid for any external strain:

$$p' = p'_{ss} + \frac{C_h\chi}{1+C_h\chi} p_h \tag{4-33}$$

$$q = q_{ss} + \frac{C_h\chi}{1+C_h\chi} q_h \tag{4-34}$$

For a given C_h the redistribution of external stress between hydrates and soil skeleton is given by χ. When χ decreases (i.e., when degradation is taking place), the mechanical contribution associated with the hydrates is progressively transferred to the sediment matrix. A similar phenomenon takes place during dissociation, and once the hydrates fully dissociate, the external stresses are equal to the soil skeleton ones (i.e., as expected, there is no contribution from the hydrates).

Considering equations (4-33) and (4-34), the external (global) effective stress can be expressed as follows.

$$d\boldsymbol{\sigma}' = d\boldsymbol{\sigma}'_{ss} + \frac{C_h\chi}{1+C_h\chi} d\boldsymbol{\sigma}_h \tag{4-35}$$

Finally, d$\boldsymbol{\sigma}$’ becomes:

$$d\boldsymbol{\sigma}' = \left[\mathbf{D}_{ss} + \left(\frac{\chi}{1+C_h\chi} \right)^2 \mathbf{D}_h \right] d\boldsymbol{\varepsilon} + \left[\mathbf{d}_{C_h} + \boldsymbol{\sigma}_h \left(\frac{\chi}{1+C_h\chi} - C_h \left(\frac{\chi}{1+C_h\chi} \right)^2 \right) \right] dC_h \tag{4-36}$$

The constitutive equations quoted above provide the relationships between the external stresses in terms of hydrate and soil matrix stresses. Eq. (4-36) in particular expresses the changes in external effective stresses, when changes in total strains and hydrate concentration take place. Note that C_h is acting as a 'pseudo-strain' (i.e. Eq. 4-36), in the sense that changes in hydrate concentration also induce changes in effective stress.

4.3 Model application-constant S_h

The performance of the model presented in Section 4.2 was compared against available experimental data (most of them published recently) involving a variety of conditions, from tests at constant S_h, to experiments involving hydrate dissociation at constant stresses.

The hydrates parameters K_h and G_h can be considered material constants, therefore they were not changed in the analysis considered. They were from (Miranda & Matsuoka, 2008). As for the model related to the sediment skeleton, an ellipse (as in the MCC model) was adopted initially in all the cases. However, when the response based on the MCC yield surface was not satisfactory, its shape was slightly modified to improve the model performance. This happened in the analyses corresponding to Cases 2 and 3 below, in all the other analyses the MCC yield surface was adopted. More details about the determination of the model parameters are provided below in each one of the analyzed cases. It is also worth mentioning that the main aim of the modeling was not to exactly reproduce the experimental behavior, but to check whether or not the suggested approach was able to capture the main features of GHBS behavior observed in these experiments.

The equations presented in this section can be integrated numerically as suggested in Pinyol et al. (Pinyol Puigmartí et al., 2007). The stress integration method proposed by (Sloan, 1987) was adapted for the specific characteristics of this model. All the analyses presented in this paper correspond to the ‘point integration level’ type. For the modeling of the tests loaded at constant hydrate concentration, dC_h was kept constant, changes in $d\boldsymbol{\varepsilon}$ were introduced by steps and $d\boldsymbol{\sigma}$’ was updated correspondingly (see Eq. (4-36)). While for those cases in which hydrate dissociation was induced at constant effective stress (i.e. cases below in Sections 4.3.4 and 4.3.6), $d\boldsymbol{\sigma}$’ was hold constant, dC_h was changed by steps and Equation (4-36) was solved in terms of $d\boldsymbol{\varepsilon}$. All the experiments analyzed in this paper were conducted under drained conditions, this assumption was considered in the corresponding modeling.

4.3.1 Case 1-Different hydrate saturation

Hyodo et al. (2013) reported triaxial compression tests on synthetic HBS samples conducted at four constant hydrate saturations (i.e. S_h=0; 24.2; 35.1; and 53.1%) All the samples were prepared at a similar porosity (i.e., ϕ~40%). The effective confining pressure for all the tests was 5 MPa. The samples were isotopically consolidated first and then subjected to shearing. The main test conditions related to this experimental study are listed in Table 4-1.

Table 4-1 Test conditions for triaxial compression tests studied

Effective confining pressure (MPa)	Porosity (%)	S_h (%)
5	39.4	0
	39.6	24.2
	39.2	35.1
	40.1	53.1

The model parameters were determined using back-analysis based on two tests, the one involving sediments without hydrates (i.e., S_h=0) and the test related to the highest hydrate saturation (i.e., S_h~53.1%). Then, this model (without modifying the parameters adopted before) was used to predict the behavior of the samples with S_h~24.2% and S_h~35.1%. Table 4-2 lists the parameters adopted in the numerical simulations. Figure 4-2 a & b show the comparisons between experimental and model results for the different hydrate saturations in terms of deviatoric stress and volumetric strains versus axial strains. The specimen corresponding to hydrate saturation equal to 53.1% presents a (slight) stress-softening (post-peak) behavior and a dilatant response; while all the other samples exhibits a predominant compression behavior. The relatively high confining pressure at which these tests were performed (i.e., σ'_c=5 MPa) could be one reason for the predominant hardening behavior with positive volumetric strains observed in the experiments. In all the tests, the initial stiffness and shear strength increase with S_h. The model was able to match very satisfactorily the stress-strain curves for all the experiments under study, i.e. the ones used for calibration and also the others two prediction tests. The agreements between tests and models results in terms of volumetric behavior were also excellent.

Table 4-2 Parameters adopted in the modeling

Properties	Test S_h=0	Test S_h=24.2%	Test S_h=35.1%	Test S_h=53.1%
M	1.30	1.30	1.30	1.30
λ	0.16	0.16	0.16	0.16
κ	0.004	0.004	0.004	0.004
p_c (MPa)	10.0	10.0	10.0	10.0
a	3	3	3	3
n	1	1	1	1
γ	-1/9	-1/9	-1/9	-1/9
C_h (initial)	0	0.096	0.138	0.213
α	-	32	32	32
β	-	1.0	1.0	1.0
r_1	-	4.1	4.1	4.1
r_0	-	1e-5	1e-5	1e-5
η	42	42	42	42
χ_0	-	1	1	1
K_h (MPa)	-	9600	9600	9600
G_h (MPa)	-	4300	4300	4300

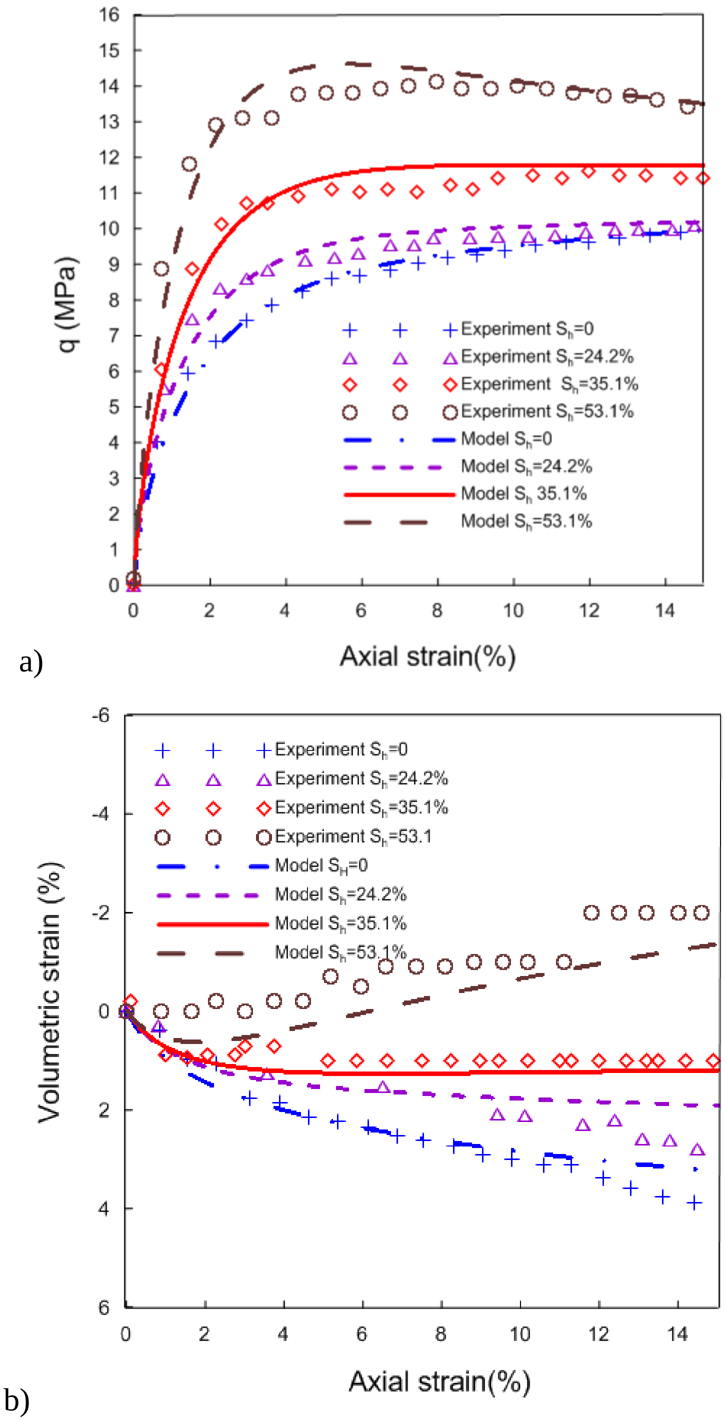

Figure 4-2 Comparisons between model and experimental results for synthetic samples of GHBS prepared at different hydrate saturations: a) stress-strain behavior, b) volumetric response. Experimental data from (Hyodo et al., 2013)

4.3.2 Case 2-Morphology effect

Triaxial compression tests based on synthetic methane hydrate samples were performed by (Masui et al., 2008). Some specimens were prepared using the ice-seed method that generally produces gas hydrates with dominant pore-filling pore-habit (Masui et al., 2008). For other samples, the partial water saturation method was adopted, which generally leads to GHBS where the cementing morphology type is dominant (Masui et al., 2008). Toyoura sand was adopted for all the tests. These specimens were tested in a triaxial device capable of reproducing fluid pressures equivalent to conditions of around 800 meters under sea level. The tests were conducted at a σ'_c=1.0 MPa. No hydrate dissociation was induced during the experiments.

The three experiments presented in Figure 2-2b carried out by (Masui et al., 2008) were selected to study the capability of the model to reproduce the effect of hydrate morphology on the mechanical behavior of GHBS. The main parameters adopted for the numerical analysis are listed in Table 4-3. (Masui et al., 2008) reported porosity values between 37.7% and 42.4%. The hydrate saturation was very similar in both tests (i.e., S_h~0.41).

Table 4-3 Parameters adopted in the modeling

Properties	Pure sand	Pore-filling	Cementing
M	1.17	1.17	1. 17
λ	0.18	0.18	0.18
κ	0.006	0.006	0.006
p_c (MPa)	12	12	12
a	3	3	3
n	1.02	1.02	1.02
γ	-1/9	-1/9	-1/9
C_h (initial)	0	0.16	0.16
α	-	35	70
β	-	1.0	1.0
r_1	-	1.1	1.05
r_0	-	7e-5	1e-4
η	15	15	15
χ_0	0	1.0	1.5
K_h (MPa)	-	9600	9600
G_h (Mpa)	-	4300	4300

Figure 4-3 shows the comparisons between experimental results and model outputs in terms of stress-strain and volumetric behaviors. The model was able to capture very satisfactorily the different features of GHBS behavior (i.e. increase of stiffness, strength and dilation in the samples with hydrates) observed in these tests involving different hydrate morphologies and pure sediment. The model was able to satisfactorily capture the more marked mechanical effect that the cementing form has on GHBS behavior when compared against the pore-filling morphology type. One issue to note is that the model under-estimate the sediment dilatancy and softening for the cementing case. Note that the same HISS model parameters were adopted for the sediment in the three cases since they do not depend on the hydrates pore-habit. As discussed before, it was assumed that the initial strain-partition parameter χ_o (i.e., Eq. (4-17)) depends on hydrate morphology. The value of the cementing sample was adopted higher (i.e., χ_o=1.5) than the pore-filling one (i.e., χ_o=1.0).

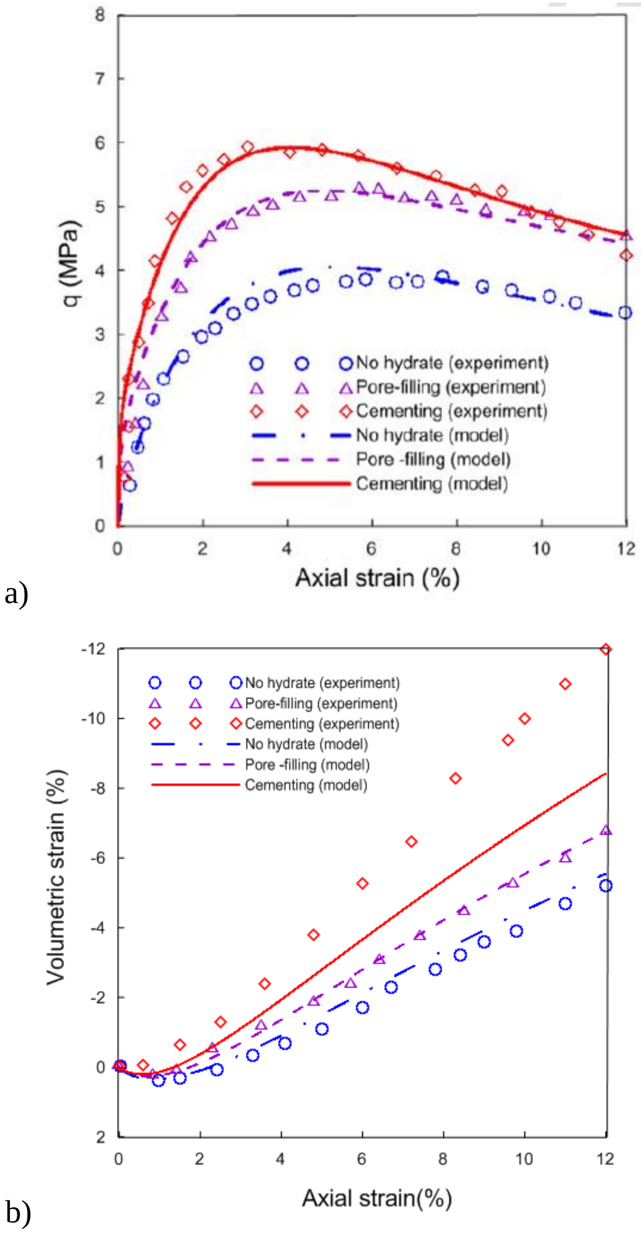

Figure 4-3 Comparisons between model and experimental results for synthetic Toyoura sand samples with different hydrates pore habits: a) stress strain behavior, b) volumetric response. Experimental data from (Masui et al., 2008)

4.3.3 Case 3-Natural core sediment

Synthetic methane hydrate specimens were modeled in the two previous Sections, in this one, experiments involving natural hydrate samples conducted by (Yoneda et al., 2015) are studied. Core samples were retrieved from the Eastern Nankai Trough by means of the pressure core analysis and transfer system. The natural sediments were maintained very close to the in-situ condition (Santamarina et al., 2012). Table 4-4 lists the main soil properties and other information associated with these experiments. Specimens identified as core#7 and core#9, with S_h~38% and S_h~79%, respectively, were tested under triaxial drained conditions. As explained in Yoneda et al. (2015), the manipulation of core#9 and core#7 induced changes in the material. Core#7 was treated using liquid nitrogen (LN_2) core method, while core#9 was treated using CH_4 purge LN_2 core method. In these two methods, the specimens were exposed to the atmospheric pressure, which might induce hydrate dissociation. Yoneda et al. (2015) suggested that the plausible in-situ hydrate saturation for core#7 could be between 65% and 90%, but because of the sample handling, the hydrate saturation decreased up to ~38% (i.e. at test condition). Furthermore, some damage of the core was observed in the CT images which means that the soil structure was affected by the handling method. As for core#9, the in-situ hydrate saturation was between 70% and 95%. It was also estimated that the hydrate saturation at test condition was around 79%. Furthermore, no damage was observed in this specimen which implies that when core#9 was tested at conditions similar to the field ones. Based on the comments above these two cores correspond to different materials and therefore slightly different parameters were assumed in the simulation of these two cases. However, the same critical state parameters were assumed for both cases because they are not related to the hydrate morphology. Table 4-5 lists the adopted modeling parameters.

Table 4-4 In situ conditions, soil index properties, and testing conditions

Test name	Host type	Overburden (m)	σ'_3 (MPa)	Water content (%)	ϕ (%)	S_h (%)
#7	Silty sand	279.3	1.5	26.4	44.1	38
#9	Silty sand	294.2	1.6	22.7	39.4	79

Figure 4-4 presents the experimental and numerical results for the stress-strain behavior and volumetric response of the natural HBS core samples discussed above. Core#9 exhibits a very noticeable peak strength, with a significant enhancement in stiffness and dilatancy, which can be associated with the higher hydrate saturation of this sample respect to core#7. As shown in Figure 4-4, the model provides enough flexibility to satisfactorily reproduce the mechanical behavior of two natural samples from Nankai Trough. The performance of the model is very satisfactory but for some slight deviations in terms of volumetric strain.

Table 4-5 Parameters adopted in the modeling

Properties	Core 7	Core 9
M	1.26	1.26
λ	0.16	0.16
κ	0.014	0.014
p_c (MPa)	12	12
a	3	3
n	0.98	0.98
γ	-0.14	-0.14
C_h (initial)	0.1675	0.311
α	6	21
β	1	1
r_1	1.1	1.3
r_0	1e-5	1.25e-4
η	3	48
χ_0	1	1
K_h (MPa)	9600	9600
G_h (MPa)	4300	4300

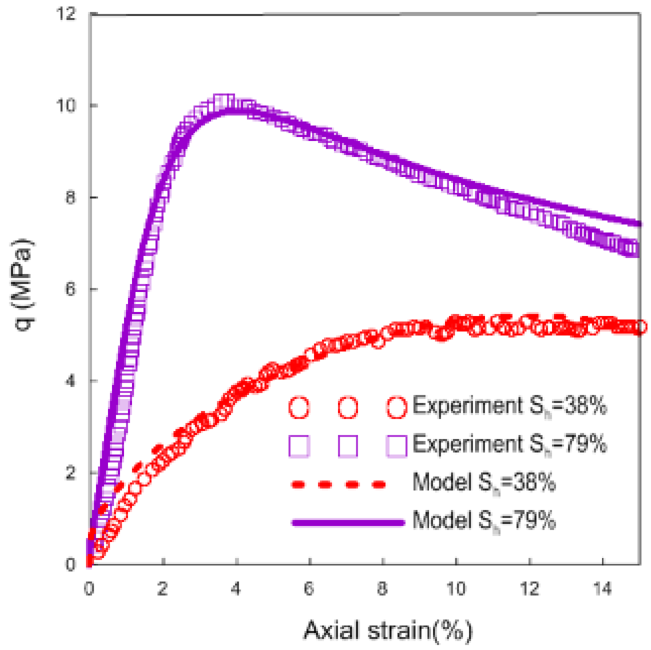

a)

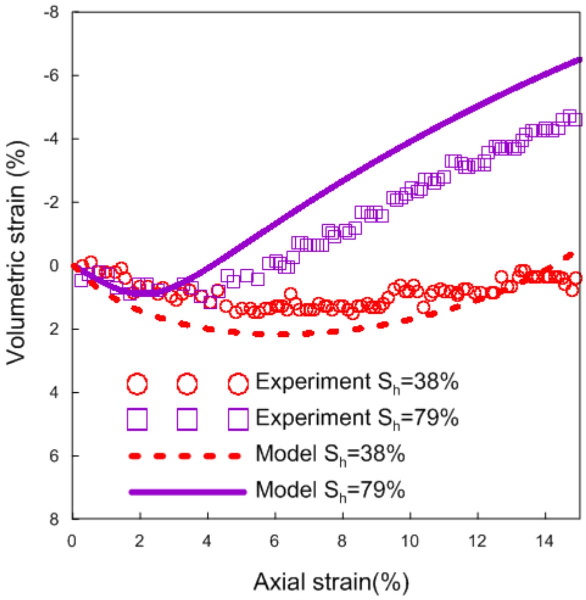

b)

Figure 4-4 Comparisons between model and experimental results for triaxial tests on natural samples: a) stress strain behavior, b) volumetric response. Experimental data from (Yoneda et al., 2015)

4.4 Parametric study

Once the ability of the model to reproduce the main tendencies observed in the experiments was checked, it could be of interest to see how other factors (not modeled in the cases before) have an influence on the behavior of GHBS. It can also be relevant to explore further about how the different parameters and inelastic mechanisms proposed in this model work to simulate the main features of GHBS behavior.

4.4.1 Case 1-Confining pressure

The first analysis in this section is related to the effect of confinement on GHBS behavior. The study is based on triaxial tests at three different cell pressures were simulated (i.e., σ'_c=1 MPa ,3 MPa ,5 MPa). Table 4-6 lists the adopted model parameters. Figure 4-5a &b show that the confinement plays a critical role in the behavior GHBS, as σ'_c decreases the peak strength decreases, the dilatancy increases and also the softening is more marked.

Table 4-6 Parameters adopted in the modeling

Properties	**σ'_3=1 (MPa)**	**σ'_3=3 (MPa)**	**σ'_3=5 (MPa)**
M	1.17	1.17	1.17
λ	0.12	0.12	0.12
κ	0.002	0.002	0.002
p_c (MPa)	11.5	11.5	11.5
a	3	3	3
n	1	1	1
γ	-1/9	-1/9	-1/9
C_h (initial)	0.195	0.195	0.195
α	16	16	16
β	1.0	1.0	1.0
r_1	2.9	2.9	2.9
r_0	1e-5	1e-5	1e-5
η	35	35	35
χ_0	3	3	3
K_h (MPa)	9600	9600	9600
G_h (MPa)	4300	4300	4300

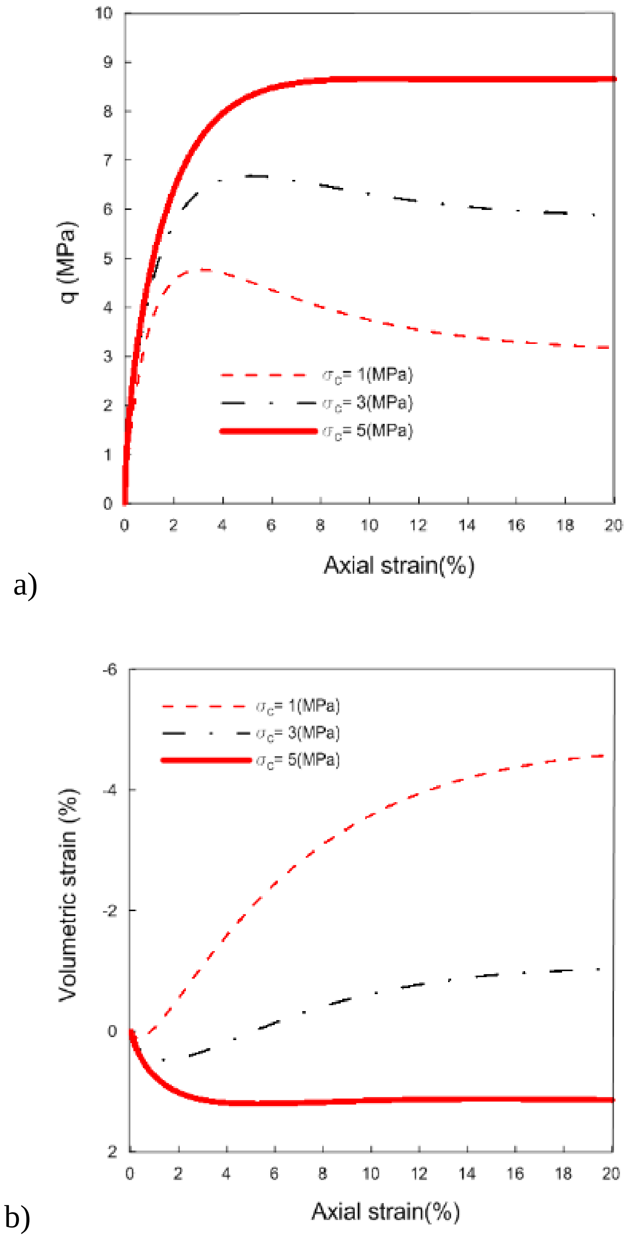

Figure 4-5 Effect of confinement on GHBS response: a) stress strain behavior, b) volumetric response

The plots in Figure 4-6 show more details about how the main variables of the model evolve for the test at σ'_c=1 MPa. The hardening or softening behavior of the sediment is controlled by the effective hardening parameter H, which depends on R, p_c and p_d through $H=R(p_c+p_d)$. It is assumed that the plastic deformations of the soil skeleton take place from the beginning of yielding. This is in line with previous works in this area (e.g., (J. Lin et al., 2015; S Uchida et al., 2012; Shun Uchida et al., 2016)). Under this assumption, the model predicts plastic positive volumetric strains at the start of the test (i.e., between 'A' and 'B', Figure 4-6a&b), because the stress state lies on the 'wet side' of F_s (Fig. 14c), therefore p_c increases. After point 'B', p_c decreases because the stress state is on the 'dry side' of F_s. The sub-loading parameter R increases during the whole test (as it depends on the module of the total plastic strain). The hardening enhancement provides by the hydrates (p_d) decreases through the tests due to progressive damage of the hydrates, up to reaching a fairly constant value. After the peak value 'C', the softening of the soil skeleton controls the global behavior of the HBS and the deviatoric stress tends to decrease substantially. The dilatant behavior of the skeleton also controls the global volumetric response of the GHBS. Figure 4-6c & d present the yield surfaces associated with this model at different stages of the test.

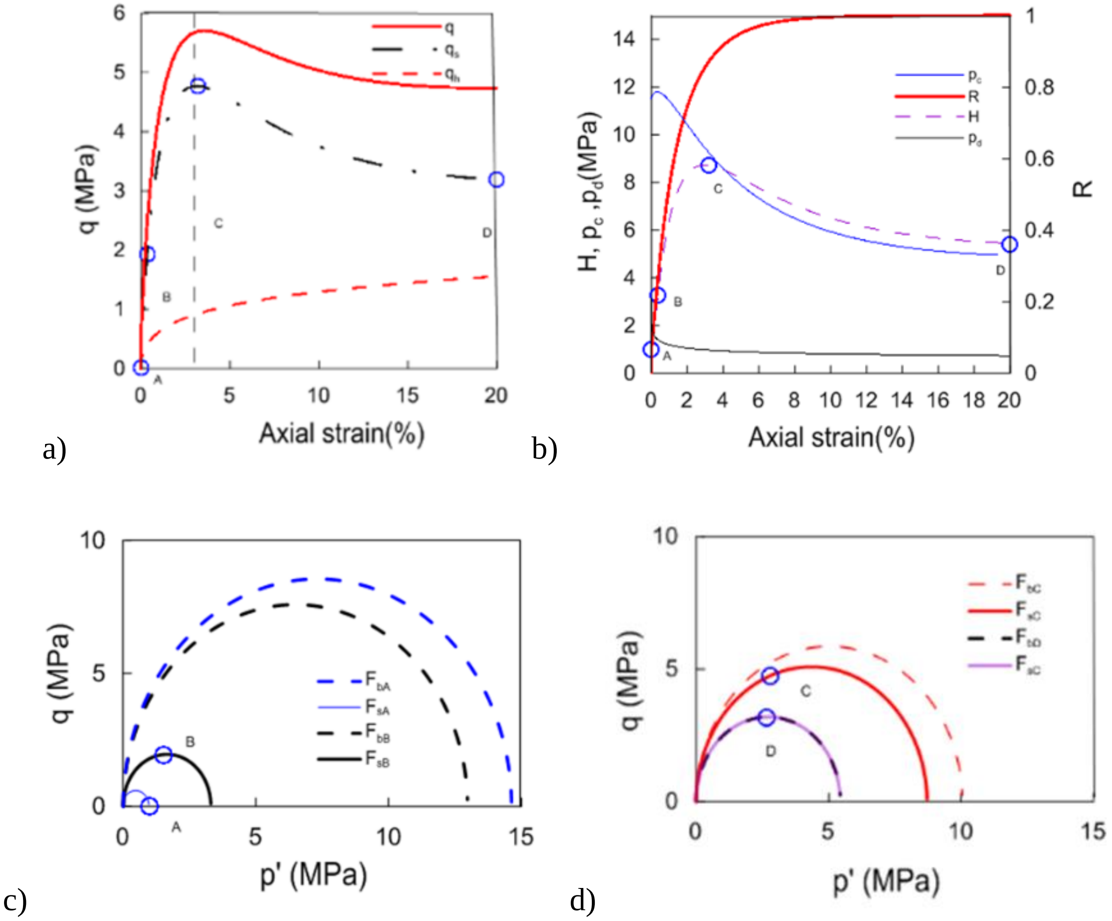

Figure 4-6 Additional modeling information for the test in Fig 13 at σ'_c=1 MPa: a) stress-strain behavior; b) hardening variables; c) yield surfaces at two initial stages of the experiment A&B; and c) yield surfaces at two final stages of shearing C&D

4.4.2 Case 2- Different χ_0

The study related to the effect of the partition parameter χ_0 on the model response is conducted. This factor controls the amount of the applied stress that is supported by the hydrate. The analysis discussed before with σ'_c=1 MPa and χ_0=3 was adopted as the base case, and two additional analyses were performed with χ_0=2 and χ_0=1. The reduction of this factor is related to a decrease of the bearing contribution of the hydrate and also with a reduction of the peak deviatoric strength Figure 4-7a). The volumetric behavior of the GHBS is also affected by this parameter (Figure 4-7b), a reduction of χ_0 is accompanied by an increase in the dilatancy. The adopted parameters are listed in Table 4-7.

Table 4-7 Parameters adopted in the modeling of HBS specimens. Effect of parameters*: χ_0

χ_0	r_0	r_1
1	$1e^{-5}$	2.9
2	$1e^{-5}$	2.9
3	$1e^{-5}$	2.9

*The parameters of the test in Table 9 with σ'_3=1 (MPa) was used as the base case for the parameter sensitivity study.

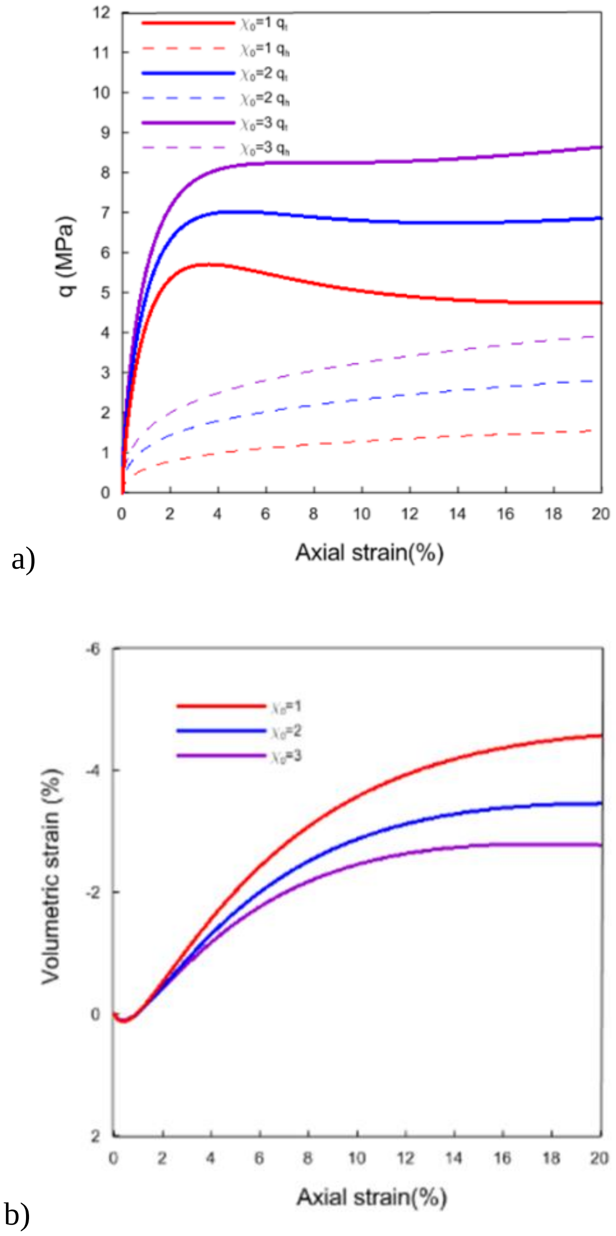

Figure 4-7 Effect of χ_0 on HBS response: a) stress strain behavior, b) volumetric response

4.5 Hydrate dissociation under loading

All the tests modeled previously involves hydrate bearing samples loaded at constant hydrate saturation. In this section, the behavior of hydrate bearing specimen under load and dissociation were studied using the proposed model. More information regarding this section can be found at (Marcelo Sánchez et al., 2017).

4.5.1 Case 1-hydrate dissociation under triaxial conditions

The tests conducted by Hyodo et al (2014) were selected to study the effect of hydrate dissociation under triaxial conditions. The main information about the samples and tests details were introduced in Section 2.2. Table 4-8 lists the main tests conditions related to these experiments.

Table 4-8 Test conditions of methane hydrate dissociation tests

Consolidation condition	σ'_c (MPa)	S_h (%)	Porosity (%)	Test Nº	Remarks
Isotropic	5	48.7	40.4	1	Dissociation→Shear
Isotropic	5	47.4	39.9	2	Shear1%→Dissociation→Shear
Isotropic	5	47.9	39.8	3	Shear5%→Dissociation→Shear

These tests provide very useful information about the effect of hydrate dissociation at two stages of shearing. When the dissociation was induced at ε_a=1%, the stress conditions were quite far from the failure of the dissociated sediment (i.e., the deviatoric stress of this sample at ε_a=1% was 8.4 MPa, while the strength at failure of the already dissociated sample was around 10 MPa, Figure 2-3). However, when the hydrate dissociation started at ε_a=5% the deviatoric stress (i.e. q≈12 MPa) was higher than the strength of the dissociated sediment and it was difficult to maintain the constant stress condition during dissociation. The sample failed and the deviatoric stress reduced tending to the strength of the dissociated sample (i.e., q≈10 MPa). These were quite complex experiments that have been simulated following, as close as possible, the reported test protocols.

The modeling of these experiments was approached as follows: i) first the test related to the already dissociated sediment was simulated (using typical reported parameters for this type of material, i.e. sand); then, ii) the test related to the dissociation at ε_a=1% was studied (and used to adjust the model parameters for the GHBS case); and finally, iii) the test involving hydrate dissociation at an initial ε_a=5% was simulated to validate the proposed model under these particular conditions. Table 4-9 lists the main parameters selected for the modeling.

Table 4-9 Parameters adopted in the modeling

Properties	Shear after dissociation	Dissociation induced at ε_a= 1%	Dissociation induced at ε_a= 5%
M	1.17	1.17	1.17
λ	0. 12	0.12	0.12
κ	0.002	0.002	0.002
p_c (MPa)	11.5	11.5	11.5
a	3	3	3
n	1	1	1
γ	-1/9	-1/9	-1/9
C_h (initial)	0	0.195	0.195
α	-	16	16
β	-	1.0	1.0
r_1	-	2.9	2.9
r_0	-	1e-5	1e-5
η	-	35	35
χ_0	-	3	3
K_h (MPa)	9600	9600	9600
G_h (MPa)	4300	4300	4300

Figure 4-8 present the comparisons between experiment and model results for the three cases discussed above. As for the already dissociated sample (Figure 4-8a), quite good agreements were obtained in terms of deviatoric stress and volumetric behavior. In particular, the model manages to replicate well the maximum stress, but slightly under-predicts the maximum volumetric strain. Figure 4-8b presents the experimental and numerical results related to the sample at which dissociation was induced at ε_a=1%. In addition to the external deviatoric stresses (i.e., the one to be compared against the experimental observations), the mechanical contributions of the hydrate and sediment skeleton are computed by the model and included in this figure as well.

Initially, both hydrate and sediment contributed progressively to the mechanical stability of the specimen. Afterwards, during hydrate dissociation, the mechanical contribution arising from the hydrate was progressively decreasing and transferred to the soil skeleton, leading to an increase in the sediment stress during this step at constant global stress. The external stress is solely supported by the soil skeleton at the end of the dissociation process. Shearing continued after full dissociation and the deviatoric stress increased until reaching the strength of the already dissociated sediment.

The model captures very satisfactorily the main trends observed in these experiments, particularly: the degradation in stiffness during the initial loading stage, the (average) deviatoric stress during dissociation, and the maximum final deviatoric stress after dissociation. However, the experimental deviatoric stress at ε_a=1% is slightly higher than the one computed by the model, and the axial strains observed during dissociation are larger than the simulated ones. Note that in any case, the volumetric deformations during dissociation are well reproduced by the model. The model slightly under-predicts the ε_v at advanced stages of the experiment (i.e., ε_a>12%). At that final stages of shearing, the three yield surfaces considered in this model coincided in one, and the stress state is on the summit of that ellipse. Therefore, according to the model, there are not changes in plastic volumetric strains (i.e., $d\varepsilon^{vp}=0$) and ε^{vp} remains fairly constant. In this way, the model simulates the material failure (i.e., continuous deformations at constant deviatoric stress). More details about how the different mechanisms adopted in this model work are presented in the following case.

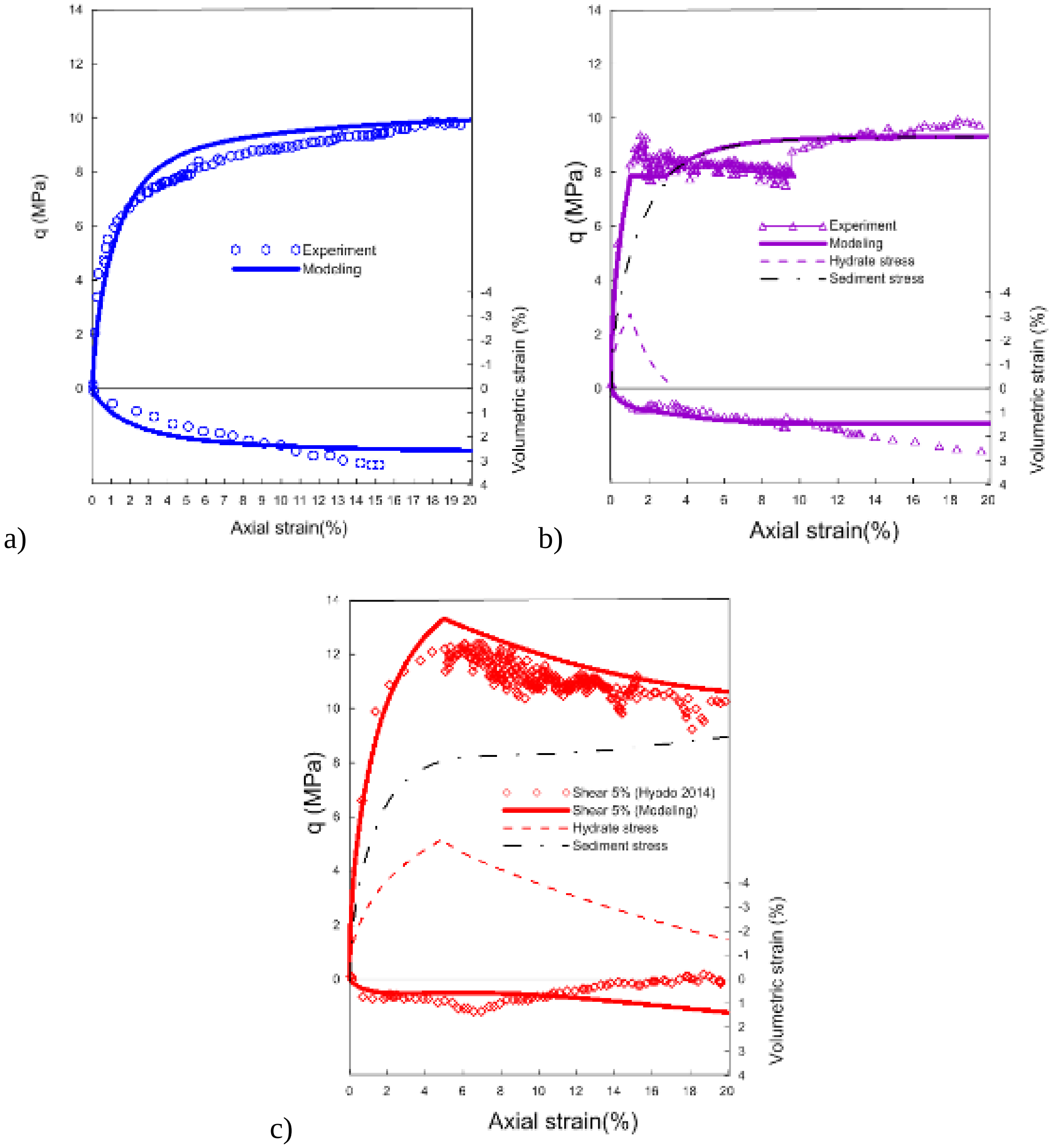

Figure 4-8 Experimental and modeling results for drained triaxial tests: a) already dissociated sediment, b) dissociation induced at ε_a=1%; and c) dissociation induced at ε_a=5%. Experimental data from (Hyodo et al., 2014)

Once the model parameters were calibrated using the two previous cases, the ability of the constitutive equation to predict the GHBS behavior under dissociation was checked against the third test. Figure 4-8c presents the comparisons between the experimental results and the model predictions for the case in which the hydrate was dissociated at ε_a=5%. The model results are also very satisfactory in this case, the main tendencies observed in this experiment are well captured by the model. However, the peak deviatoric stress is slightly over-predicted by the model. There are also some differences between the model predictions and the reported experimental data in terms of volumetric behavior. Surprisingly, it was observed that there was not volume change at the end of this test, because an apparent dilation during dissociation com0pensate the initial positive volumetric strains. This final dilation in the experimental result seems strange, the tendency during dissociation at high stresses under drained conditions should be to contract, because the sediment structure tend to a more compact state as the hydrates disappear. The positive ε^v predicted by the model during dissociation are related to the volumetric compression plastic strains induced by the collapse of the sediment structure during hydrate dissociation. This structure-collapse behavior is explained in more detail in Section 4.5.2

Hyodo et al. (2014) experienced some difficulties to maintain the deviatoric stress constant during dissociation in this test. Because of the progressive degradation of the HBS structure during hydrate dissociation, it was impossible to hold the (high) deviatoric stress applied just before dissociation (i.e., at ε_a=5%). The mechanical contribution from the hydrate (dash line) was gradually transferred to the sediment skeleton during dissociation, and the global deviatoric stress decreased progressively until reaching the maximum strength associated with the already dissociated sediment. At the end of shearing phase, the model predicts that hydrates still contribute to the mechanical behavior of the sample, this result is supported with the reported experimental data indicating that not all the hydrates dissociated at the final axial strain (i.e., ε_a=20%).

Figure 4-9 shows additional information about this modeling. Figure 4-9a presents the q-ε_a plot extended until full dissociation. As discussed before, during dissociation the bearing capacity of the hydrates decreased and the stress were gradually transferred to the sediment. The model predicts that at advanced stages of shearing and hydrate dissociation all the external stresses are supported by the sediment skeleton only. The effective hardening parameter ($H=R(p_c+p_d)$) always increased (Figure 4-9b). This implies that F_s kept expanding during the whole test. The variable R always increased during the simulation as well (Figure 4-9b). The increase in H (i.e. hardening of the sediment skeleton) observed at advanced stages of the experiment was induced by the volumetric-collapse-compression strains discussed above; which compensated the decrease of p_d during hydrate dissociation. Figure 4-9c presents the three initial yield surfaces (i.e., F, F_s, and F_b) considered in this model at the start of the test. Figure 4-9d presents again these three yield surfaces at two different stages: i) at ε_a=15.3%, i.e. when the sub-loading yield surface reached the boundary one (F is still inside $F_b=F_s$, because p_d did not vanish totally at this stage); and ii) at the end of the test, when the three yield surfaces coincided in one.

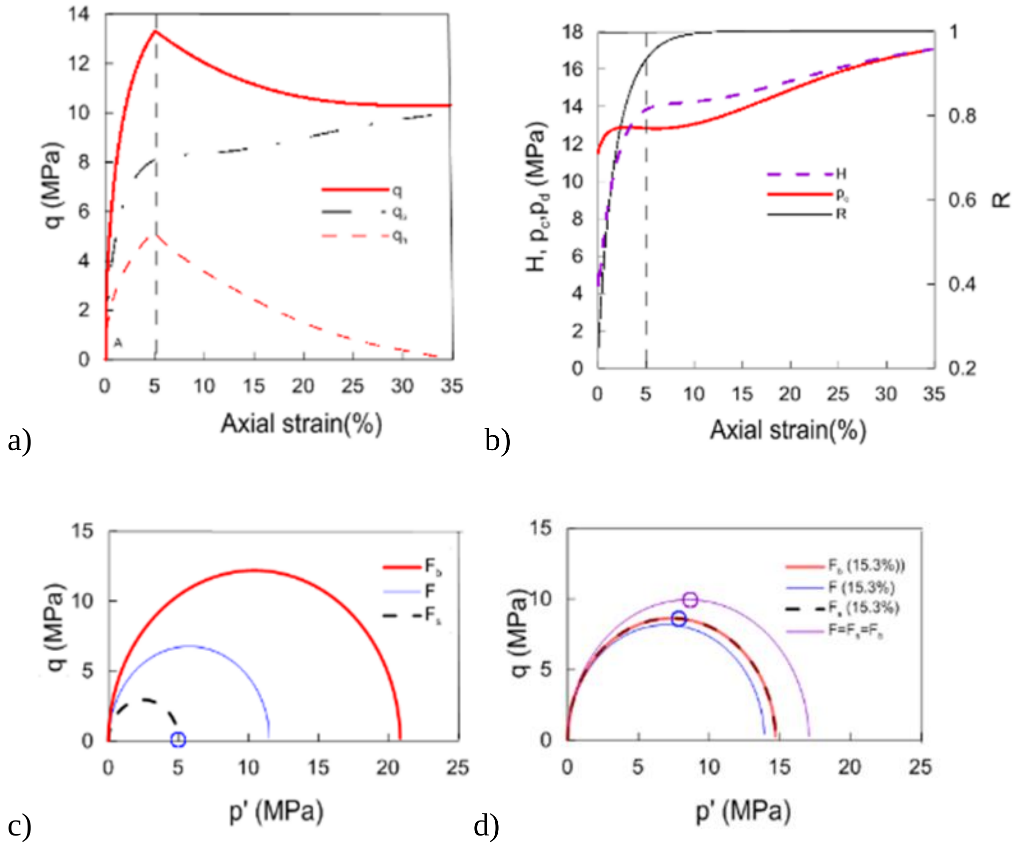

Figure 4-9 Additional modeling information for the test in which dissociation was induced at ε_a=5%: a) extended stress-strain behavior; b) hardening variables, c) yield surfaces at the beginning of the experiment; and c) yield surfaces at an intermediate stage of shearing (ε_a=15.3%) and at the end of test

The proposed model has not only reproduced and predicted satisfactorily the behavior observed in the experiments, but it has also provided an explanation to the main features and trends of GHBS behavior observed during the tests. In the tests, the hydrate dissociation was induced by heating (Hyodo et al., 2014). Thermal effects were not modeled in this analysis. This seems a reasonable assumption as the main focus here was on the influence of hydrates dissociation on material behavior. It also seems that temperature may have a small influence on the overall mechanical behavior of the specimen in this type of experiment. A more sophisticated analysis can certainly be done in the future incorporating thermal effects. The inclusion of temperature could also help to reproduce these experiments more closely.

4.5.2 Case 2-hydrate dissociation under oedometric conditions

The last set of experimental data studied in this work corresponds to two natural specimens gathered by means of the Pressure Core Characterization Tools (PCCTs) (Santamarina et al., 2012; Santamarina et al., 2015). The samples were loaded uniaxially with lateral confinement (i.e. oedometric conditions). General information about this research was presented in section 2. The test presented in Figure 2-3b) plus another one with a lower hydrate saturation are simulated in this section. The parameters reported (Santamarina et al., 2015) for the dissociated sediment (i.e. a silty sand) were adopted in the simulations. The selected parameters are listed in Table 4-10.

Table 4-10 Parameters adopted in the modeling of HBS specimens

Properties	core 8P	core 10P
M	1.07	1.07
λ	0.605	0.12
κ	0.065	0.04
p_c (MPa)	2.32	3.5
a	3	3
n	1	1
γ	-1/9	-1/9
C_h (initial)	0.102	0.3605
α	6	12.5
β	1.0	1.0
r_1	2.5	2.9
r_0	1e-6	2e-7
η	15	0.5
χ_0	1	3
K_h (MPa)	9600	9600
G_h (MPa)	4300	4300

Tests and models outputs related to the specimen ‘core-8P’ (i.e. initial S_h=18%) are presented in Figure 4-10a. The GHBS specimen was subjected to a monotonic increase in the vertical stress up to σ'_v=6 MPa, followed by an unloading up to σ'_v=3 MPa. Hydrate dissociation was induced in this over-consolidated sample followed by cycles of loading (with a maximum σ'_v=9 MPa) and unloading of the already dissociated sediment. The experimental and numerical results associated with specimen ‘core-10P’ (i.e. initial S_h=74%) are presented in Figure 4-10b. In this case the effective vertical stress was increased until σ'_v=3 MPa and hydrate dissociation was induced at this constant effective stress (under normally-consolidated conditions). Once the sample was fully dissociated, the vertical stress was increased until a maximum σ'_v=9 MPa, followed by an unloading. Settlements were recorded in the both tests during all the loading stages.

The proposed framework was able to represent very satisfactorily the main tendencies observed in the experiments. The yield stress and unloading-reloading behavior are properly reproduced in both specimens. The model slightly over-predicts the initial stiffness of the core-10P. It is worth to highlight the model ability to reproduce the differences in volumetric strains observed during dissociation at constant stress in these two tests. The collapse compression behavior exhibited by core-8P was much less noticeable than the one observed in core-10P. This large volumetric strain can be associated with significant rearrangements of the GHBS structure during hydrate dissociation. Some factors that can be considered to explain the differences between core-8p and core-10p in terms of the amount of the volumetric strain observed during dissociation are as follows: i) difference in hydrate saturation between the two samples (i.e. core-8P S_h=18% << core-10P S_h=74%); ii) difference in the effective vertical stress at which hydrates dissociation was induced (i.e. core-8P σ'_v=3 MPa << core-10P σ'_v=8 MPa), therefore the effect of confinement on the re-accommodation of the sediments particles is less significant for core-8p; iii) dissociation in core-8P took place under over-consolidated conditions while in core-10p dissociation happened under normally-consolidated conditions; and iv) core-8p was previously loaded up to a very high effective vertical stress (i.e. σ'_v=6MPa) that degraded the bonding effects of the hydrate and induced important changes in the sediment structure previous to dissociation.

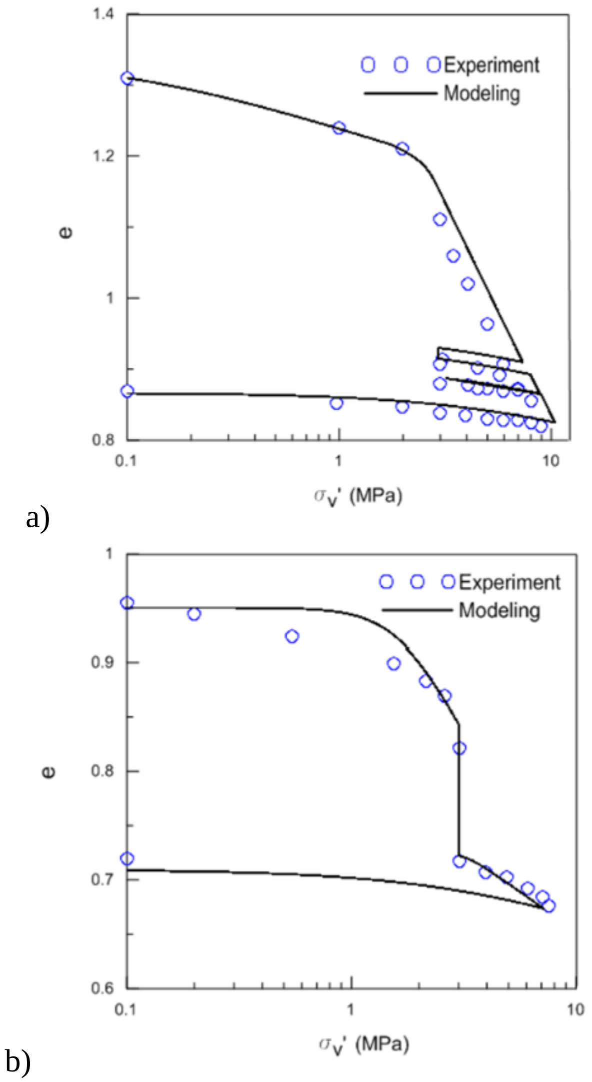

Figure 4-10 Behavior during dissociation of natural HBS specimens under oedometric conditions: a) core 8P; and b) core 10P. Experimental data from (Santamarina et al., 2015)

Figure 4-11a presents the evolution of σ'$_v$ calculated by the model in the soil skeleton and hydrate, together with the global (or external) one for the case of core-8P. A significant portion of the stress increase is taken by the hydrate at the beginning of the experiment, i.e. path ‘A-B’. Note that the hydrate saturation is very high in this case (i.e., S_h=74%) and therefore an important bearing contribution from the hydrate can be anticipated. Upon dissociation at constant effective stress, the load is gradually transferred from the hydrate to the sediment skeleton and significant plastic volumetric strains are computed by the model, i.e. path ‘B-C’. After full dissociation, the stresses are supported by the soil skeleton only, and the subsequent loading (‘C-D’) and unloading (‘D-E’) steps are controlled by the properties of the already dissociated sediment. Figure 4-11b shows that the hardening enhancement effect (controlled by p_d) reduces progressively during loading and it disappears during dissociation. The effective hardening parameter H increases during loading and remained unchanged upon unloading.

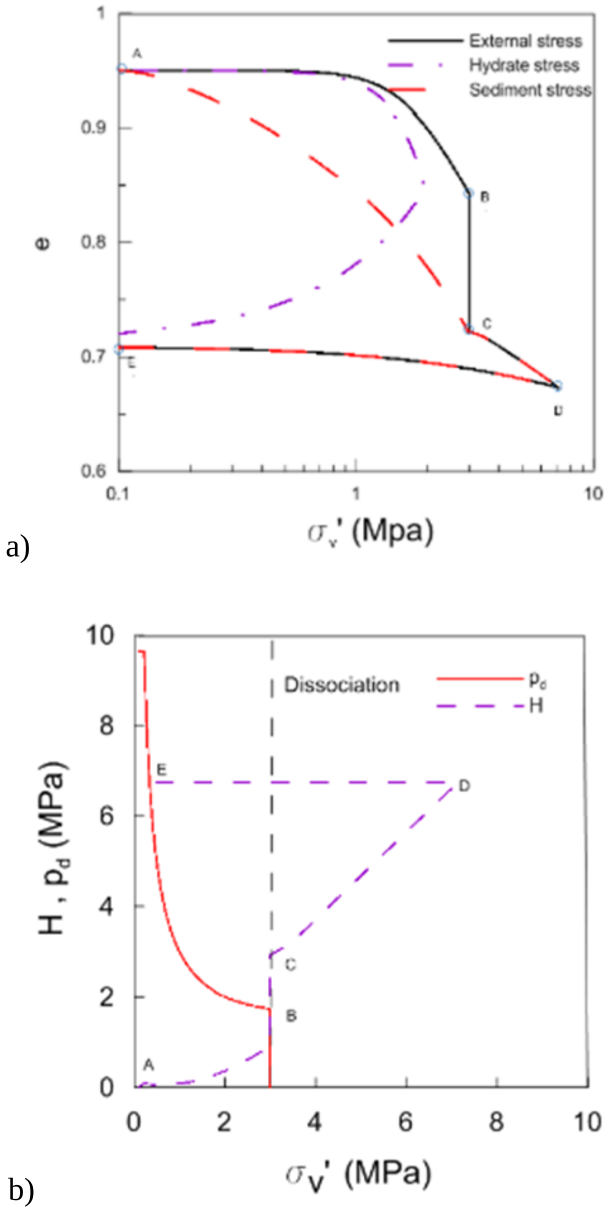

Figure 4-11 Additional modeling information for the test related to core 10P: a) vertical stresses computed by the model during loading; b) hardening variables

4.6 Conclusion and discussion

A constitutive model for hydrate bearing sediments is presented in this section. Experimental observations have shown that the presence of hydrates impacts on different aspects of sediment behavior, amongst others: stiffness, peak stress, softening behavior and dilation. It has been observed that these features of soil behavior depend on hydrate saturation as well. Hydrates also contribute to the mechanical stability of the sediment. Furthermore, during dissociation important changes in the mechanical behavior of GHBS and soil structure have been observed. The model proposed in this work encompasses different inelastic mechanisms to describe these complex features of GHBS behavior. The concept of stress partition was incorporated into the model to estimate the mechanical contribution associated with hydrates and soil skeleton at different stages of loading and hydrate dissociation. A damage model was adopted to describe the behavior of hydrate during loading, while the HISS elastoplastic model was selected for the sediment skeleton. The HISS model is a versatile mechanical constitutive law based on critical state soil mechanics. The proposed framework also incorporates sub-loading and hydrate enhancement mechanisms.

Information from several mechanical tests recently published is selected to study the model capabilities. The experiments were chosen to cover the most relevant conditions related to GHBS behavior. Hydrate soil specimens covering a wide range of hydrate saturations were considered in the analyses. The effect of hydrate morphology and confinement on the mechanical behavior of GHBS is also investigated in this work. Particularly attention was paid to the study of the mechanical behavior of GHBS during hydrate dissociation under loading. In the cases in which there was enough experimental data, some tests were used for determining the parameters and the other ones were left apart for model validation. The model performance during all of these conditions was extremely satisfactory. The proposed geomechanical model was capable of capturing not only the main trends and features of sediment observed in the different tests, but also to reproduce very closely the experimental observations in most of the analyzed cases. The enhancement of sediment strength, stiffness and dilation were well reproduced by the model. The ability of the proposed approach to simulate the volumetric soil collapse compression observed during hydrate dissociation at constant stresses is particularly remarkable. A contribution of this work is the modeling of GHBS during dissociation. This model has also assisted to interpret how sediment and hydrates contribute to the mechanical behavior of GHBS and how these contributions evolve during loading and hydrates dissociation.

5 MECHANICAL BEHAVIOR OF A PARTIALLY SATURATED SOIL

5.1 Introduction

In this section, a joint effort to enhance the current understanding of partially saturated clay silt by the Texas A&M University and Polytechnic University of Catalonia is presented. The experimental study centred on the stress-strain response of a compacted clayey silt during shearing were conducted by the group from the Division of Geotechnical Engineering and Geosciences, A controlled-suction triaxial cell with local axial and radial instrumentation (optical laser-based technique) is used to precisely monitor the volume change evolution on shearing. Several controlled-suction stress paths under isotropic stress state (drying/wetting, loading/unloading and wetting/drying) have been performed to induce different and slightly over-consolidated states before targeting the same initial state (mean stress and matric suction) for the shear tests. A series of controlled-suction triaxial compression paths have been then carried out at the different over-consolidated states previously generated, which also included the normally consolidated state. The modeling efforts were carried out by the author's group from Texas A&M University. The Barcelona Basic Model (BBM) was initially adopted in this work as a formal approach to analyse the soil response in the different experiments. Afterwards, the modification of the BBM model (Alonso et al., 1990) is presented in detail including the main equations associated with new formulation.

5.2 Experimental program

The experimental study centred on the stress-strain response of a compacted clayey silt during shearing were conducted by the group from the Division of Geotechnical Engineering and Geosciences, a detailed description of the experiment procedures are demonstrated below.

5.2.1 Tested material and compaction procedure

Laboratory tests were performed on a low plasticity clayey silt from Barcelona. It has a liquid limit of w_L = 32%, a plastic limit of w_P = 16%, 15% of particles less than 2 µm and a density of solids ρ_s = 2.66 Mg/m^3 (Barrera et al., 2002). Samples have been obtained following a stress-controlled isotropic static compaction procedure, ensuring no induced fabrication anisotropy. Powder passing ASTM No.16-1.18 mm has been left in equilibrium at an average relative humidity of 50% to achieve a hygroscopic water content of 2.2%. The silt was then sprayed with demineralised water to reach a water content of 11.0%. After equilibrium, the material was statically compacted following a two-step procedure. In the first step, a low vertical stress was applied to the soil mass confined in a split mould, until reaching a dry density of 1.20 Mg/m^3, which is required to handle the sample. In the second step, the sample was installed in a conventional triaxial cell under a net isotropic stress of p = 0.6 MPa, which was maintained for 40 min. The compacted sample presented a final dry density around 1.63 Mg/m^3 (void ratio e = 0.632), a degree of saturation of 46.3% and a total suction of s = 0.80 MPa measured with a psychrometer. Due to end-restraint effect, the sample has been subsequently trimmed to achieve uniform sample dimensions of 38 mm in diameter and 76 mm high. The initial sate of the sample is shown in the compaction plot represented in Figure 5-1. Isotropic static compaction results following the same procedure at different mean net stresses are presented. Contours of equal total suction obtained by psychrometer readings are also plotted in the figure.

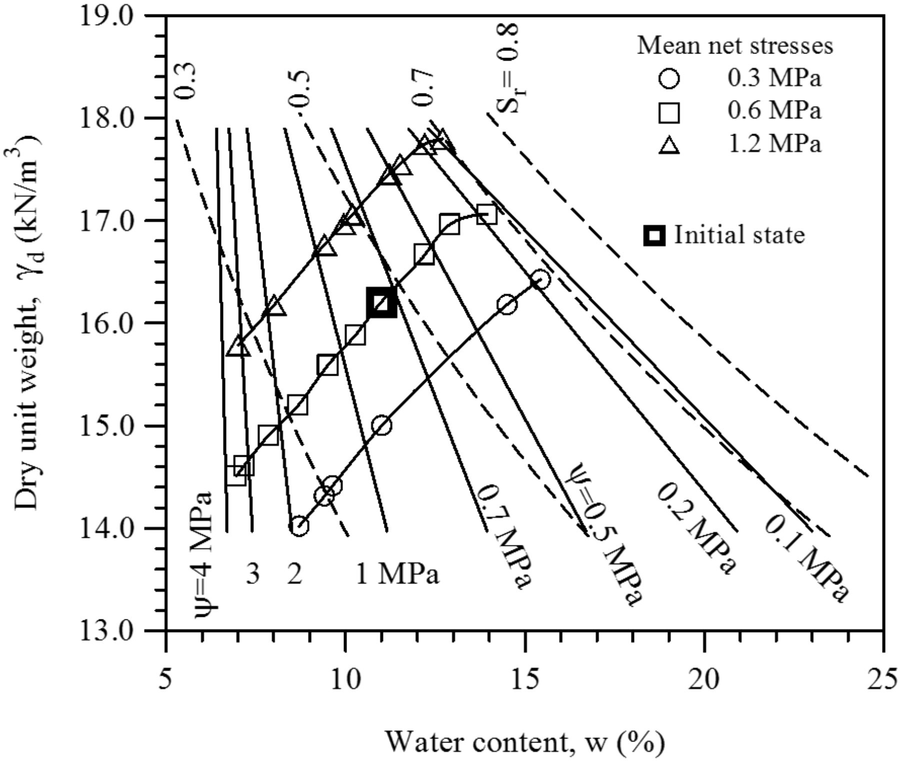

Figure 5-1 Compaction curve of samples

5.2.2 Triaxial cell and stress paths followed

Figure 5-2 represents a cross-section scheme of the controlled-suction triaxial cell (Barrera et al., 2002; Romero et al., 1997; Romero Morales, 1999). Matric suction is applied simultaneously via air overpressure technique to both ends of the sample, maintaining a constant air pressure (number 8 in Figure 5-2) and controlling water pressure (numbers 9 and 10). Top and bottom caps include a combination of two porous stones: a peripheral coarse one (number 12) connected to the air pressure and an internal HAEV one (1.5 MPa of bubbling pressure; number 11). This double drainage ensures a significantly shorter equalisation stage for liquid pressure. However, this system usually traps more occluded air at low suctions. Water content changes in the soil are calculated measuring the water volume that crosses both HAEV discs by means of two burettes with 10 mm^3 resolution. This volume is corrected by taking into account the amount of air diffusing through the ceramic discs.

Axial displacements are measured locally using two LVDT transducers (number 2). Radial deformations on two diametrically opposite sides are measured locally by means of an electro-optical laser system (2 μm resolution) mounted outside the chamber (number 3). This measuring system can be moved throughout the sample height by means of an electric motor (number 15). In this way, the whole profile of the sample from the base to the top cap can be measured, giving an estimation of the global volume and degree of saturation change. Axial load is applied at a typical displacement rate of 1 μm/min by means of a fluid pushing a piston in the loading pressure chamber (number 7). The top cap, screwed to an internal load cell (number 4), is maintained fixed.

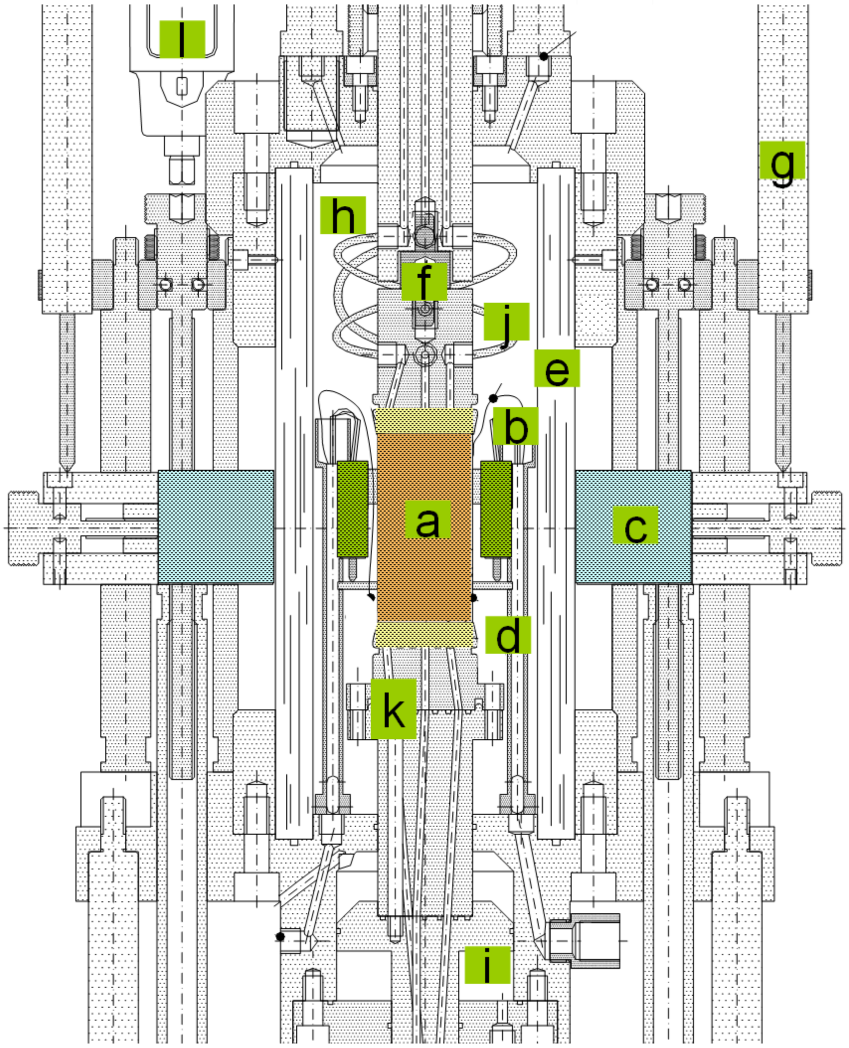

Figure 5-2. Scheme of the triaxial cell and picture. a) Specimen; b) local LVDT (axial strain); c) laser displacement sensor (radial strain); d) high air-entry ceramic disc surrounded by coarse metallic porous stone; e) Perspex wall; f) internal load cell; g) LVDT (vertical displacement of laser sliding subjection); h) confining air pressure; i) axial stress pressure chamber; j) water pressure (to volume change measuring system); k) air pressure; l) vertical displacement electric motor. Adapted from (Romero et al., 1997)

Different stress paths have been followed before the application deviatoric stress, which are indicated as paths A, B, C and D in the suction and mean stress plane shown in Figure 5-3. These four sleeted tests are name as Test A, Test B, Test C, Test D hereafter.

A constant air pressure of u_a = 0.9 MPa has been kept throughout the Test A, B C and D. These tests were initiated at p = 0.03 MPa and s = 0.8 MPa as shown in Figure 5-3 (s is suction, p is mean stress and q is deviatoric stress). The samples were isotropically compressed at a constant s = 0.8 MPa in four equalisation steps up to the same stress state at A2 / B2 (p = 0.6 MPa is the same value applied in the static compaction process).

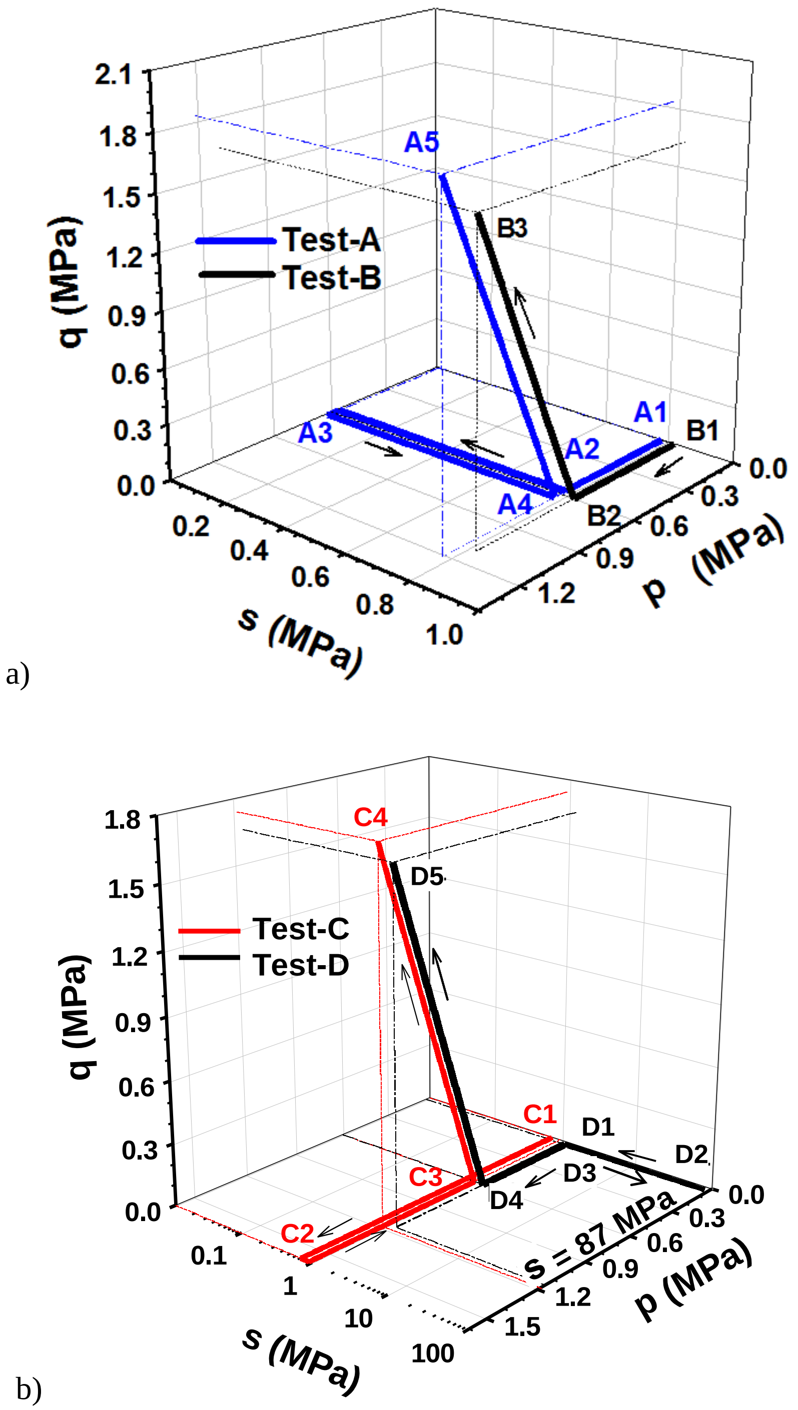

Figure 5-3 Stress paths followed in q : p : s space: a) tests A and B; b) tests C and D

In test A, a suction decrease / increase cycle at constant p = 0.6 MPa (path A2→A3→A4) was applied after this initial isotropic loading process and before the shearing stage (A4→A5). In this way, a slightly over-consolidated (OC) state is imposed to the soil before the beginning of the shearing path. The following suction steps were applied in the wetting path A2→A3: 0.8, 0.1 and 0.01 MPa. Afterwards, the sample was subjected to a drying path A3→A4 up to s = 0.8 MPa. Each step takes 10 days to make sure the sample reach equalisation in terms of strains and drainage.

While in test B, shearing (B2→B3) was applied on a normally consolidated (NC) state after the initial isotropic loading B1→B2 at constant s = 0.8 MPa. During the shearing stages at a constant rate of strain of 1.3×10-5 /min, matric suction and net cell pressure remained constant (s = 0.8 MPa and (σ_r-u_a) = 0.6 MPa). The selected axial strain rate ensures constant–suction conditions.

For test C, a previous isotropic loading and unloading path is performed at constant s = 0.80 MPa up to a maximum p = 1.60 MPa before the shearing stage. During this mechanical path: C1 → C2 → C3, an over-consolidated state was induced to the sample before shearing.

Test D was subjected to a drying and wetting cycle D1→D2→D3: 0.0-87-0.8 MPa before subjected shearing. OC state was induced by hydraulic path (D1→D2shrinkage).

To summarize, Test A, C and D are at OC state before shearing. However, they were caused by different mechanism. The OC state of Test A is caused by the collapse deformation during wetting. The OC state of Test D is caused by shrinkage during drying while Test C is caused by isotropic loading and unloading. Test B is at normally consolidated state at the beginning of shearing stage. Figure 5-4 demonstrated the stress path followed in the test and their yield locus (LC and SI) evolution.

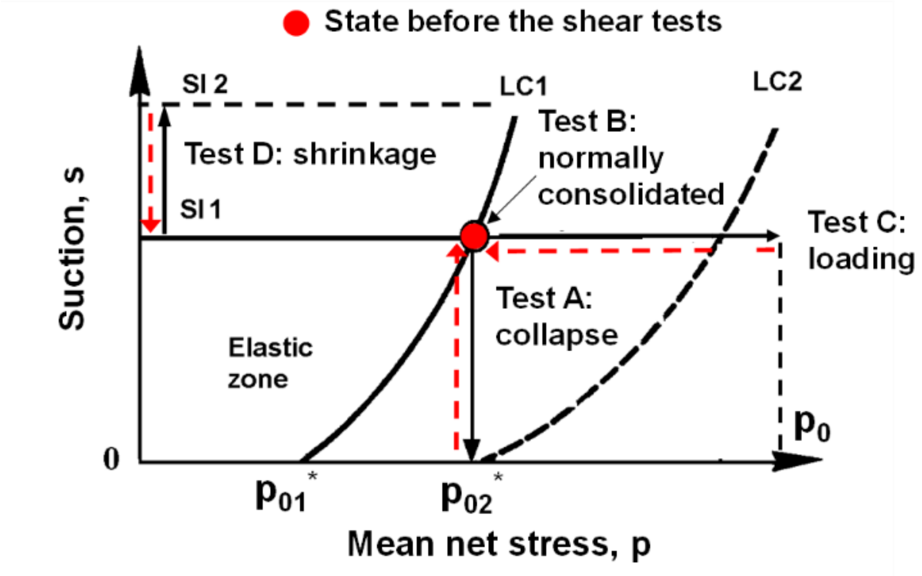

Figure 5-4 Stress paths followed in p : s plane (Tests A, B, C and D). Activation of yield locus LC and SI.

Figure 5-5 summarises the evolutions of q and ε_v for the different shearing stages at $s = 0.8$ MPa. Local axial and radial (ε_{vc}) strains were continuously registered near the central part of the specimen. At predetermined intervals, global radial strains (ε_v) were determined by means of the vertical motion of the laser sensors. As indicated in Figure 5-5, the q axial strain curves increase monotonically and stabilise at nearly the same asymptotic value, suggesting the attainment of a critical state.

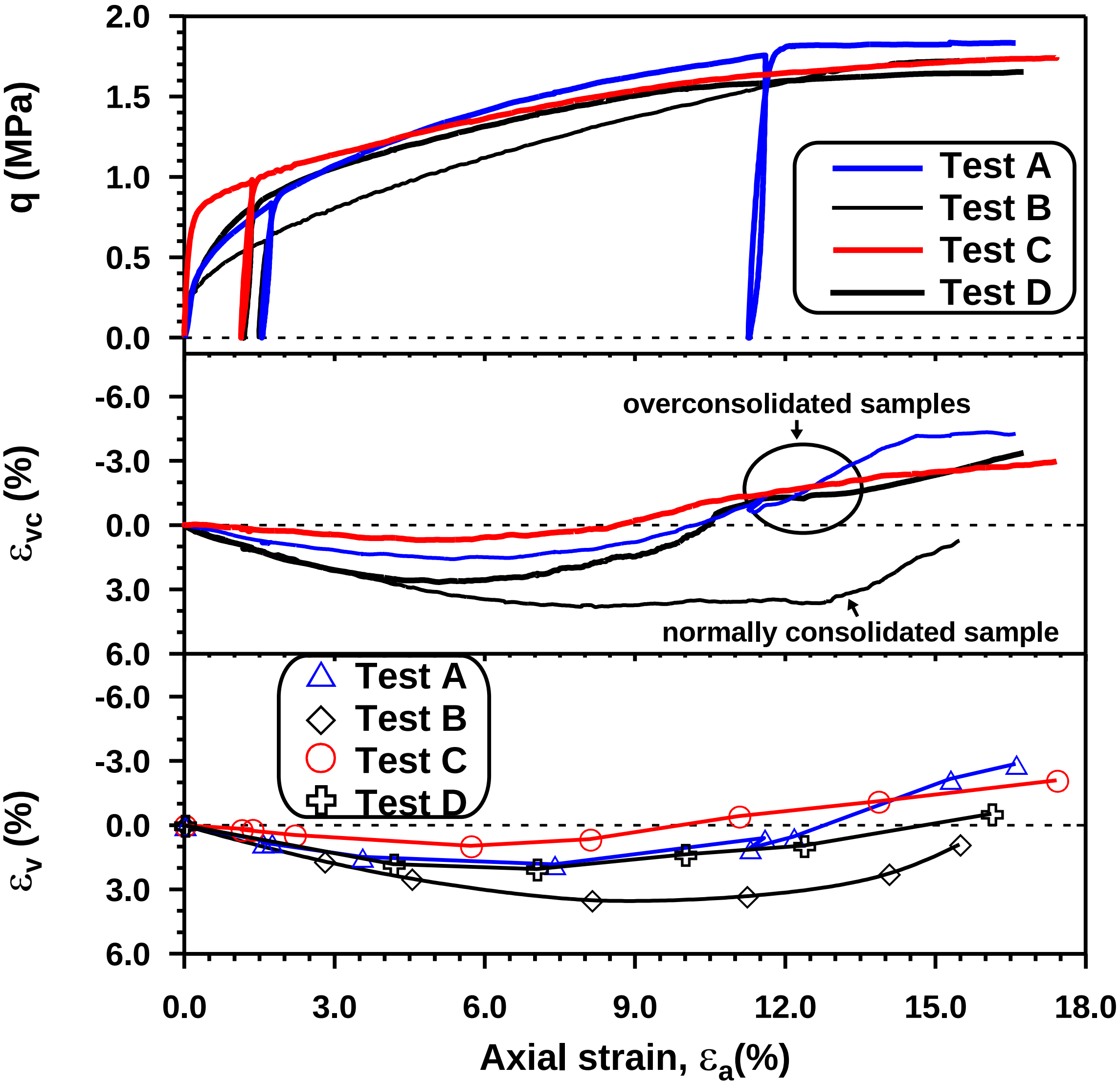

Figure 5-5 Variation of q and ε_v under shearing.

5.3 Test results and interpretation within the Barcelona Basic Model

The tests with different stress paths succinctly presented in the previous Section are discussed in more detail hereafter with the aid of a formal elastoplastic framework. The intention is to use first the BBM (which is the most established and perhaps simpler critical state framework for unsaturated soils) to check the capabilities of this model to explain the behavior observed in the experiments. The main *BBM* equations are presented first, then the estimation of the main model parameters is briefly described; afterwards the experimental and modeling results are discussed together.

5.3.1 Barcelona Basic Model main components

The original BBM was developed in the context of hardening elasto-plasticity and extends the modified Cam Clay model to the unsaturated condition. Two independent stress variables were adopted: the net stress tensor (excess of total stress over air pressure) and the suction, a scalar variable (air pressure minus liquid pressure). The yield function for triaxial stress is given by the following ellipses:

$$q^2 - M^2(p + p_s)(p_0 - p) = 0 \tag{5-1}$$

where p is the mean net stress; q the deviator stress, s the suction; and M is the slope of the critical state line. The increase in apparent cohesion with suction is given by p_s (which is initially assumed that increases linearly with suction through the constant k_s); and p_0 is the yield stress for isotropic stress conditions that is related to the applied suction through:

$$\left(\frac{\mathrm{p}_0}{\mathrm{p}_c}\right)=\left(\frac{p_0^*}{p_c}\right)^{\frac{\lambda_{(0)}-\kappa}{\lambda_{(s)}-\kappa}} \tag{5-2}$$

where p_0^* is the yield net stress for saturated conditions (which acts as a hardening parameter); p_c is a reference stress; κ is the slope related to elastic isotropic unloading–reloading paths; $\lambda_{(0)}$ is the slope of the virgin compression line for saturated conditions; and $\lambda_{(s)}$ is the slope of the virgin compression line for isotropic conditions that depends on suction through:

$$\lambda_{(s)}=\lambda_{(0)}\left[(1-r)\exp\left(-\beta\,\mathrm{s}\right)+r\right] \tag{5-3}$$

where r is a parameter controlling soil compressibility, and β provides the rate of change of $\lambda_{(s)}$ with s.Figure 5-6) shows a sketch of the yield surface in the (p, q, s) space, in which the trace of the yield locus on the isotropic $p{:}s$ plane is indicated. This trace is called the *LC* (Loading-Collapse) yield curve because it represents the locus of activation of irreversible deformation ($\mathrm{d}\varepsilon_v^p$) due to loading or wetting (collapse).

It is also considered that suction changes beyond the historical maximum suction (s_o), Figure 5-6 may also induce volumetric plastic strains, as follows:

$$\mathrm{d}\varepsilon_v^p=\frac{\lambda_s}{(1+e)}\frac{\mathrm{d}s_0}{\left(s_0+p_{atm}\right)} \tag{5-4}$$

where λ_s is the slope of the virgin compression line in terms of suction increase, e is the void ratio; and p_{atm} is the atmospheric pressure (added to avoid infinite values as s approaches zero). It is assumed that for wetting/drying processes below s_o the volumetric elastic strains depends on *s* changes through the elastic constant k_s (i.e. the compressibility constant for elastic changes in suction).

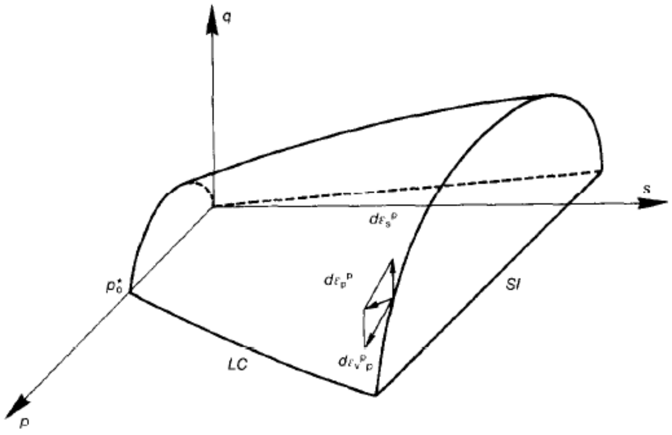

Figure 5-6 Yield surfaces of the BBM model
Adapted from (Alonso et al., 1990)

Finally, it is assumed that the isotropic hardening is controlled by the total plastic volumetric strains $\mathrm{d}\varepsilon_v^p$ (i.e. regardless if they are induced by *p*' and or *s* changes beyond the yield limits) through:

$$\frac{\mathrm{d}p_0^*}{p_0^*} = \frac{1+e}{\lambda_{(0)} - \kappa}\,\mathrm{d}\varepsilon_\mathrm{v}^\mathrm{p} \tag{5-5}$$

More details about the model formulation can be found in Alonso et al. (1990).

5.3.2 Parameter estimation

Isotropic paths involving mean net stress and suction changes were selected first to determine directly from the main model parameters. The saturated isotropic test 1 was adopted to the determine κ, p_0^*, and $\lambda_{(0)}$, as illustrated in Figure 5-7. The unsaturated isotropic Test 2 was chosen to estimate the other parameters involved in the definition of the *LC* yield locus. The initial loading at constant suction (i.e. s=0.8 MPa) was used to estimate the parameters r and β; which model the changes in soil compressibility with suction. As expected, the apparent pre-consolidation pressure observed in this experiment (i.e. p_0= 0.60 MPa) is very close to the compaction effort applied to prepare the specimens. After that, the sample is subjected at a wetting path (suction from 0.8 MPa-0.01MPa) at constant mean net stress. The deformation observed in the collapse compression path can be used to determine p_c, once the other parameters involved in the definition the *LC* curve (i.e. κ, p_0^*, $\lambda_{(0)}$, r and β) are identified.

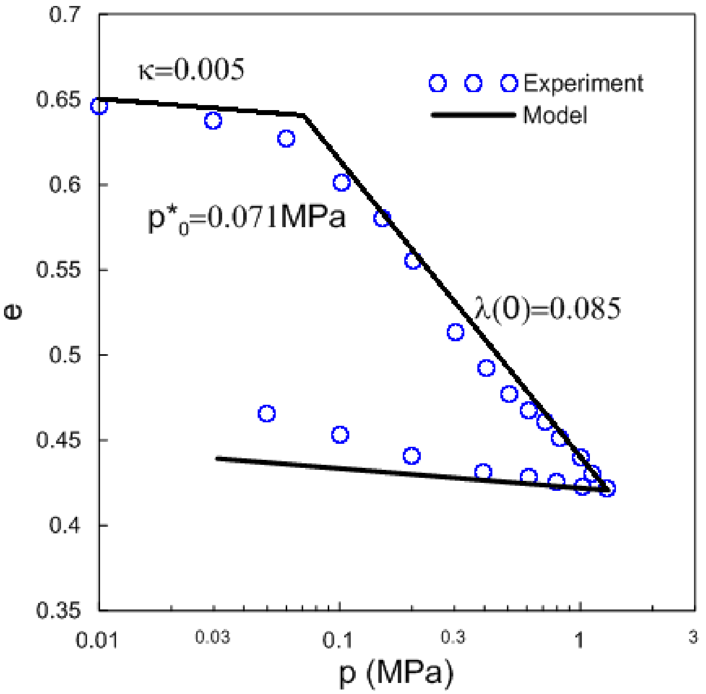

Figure 5-7 Isotropic loading on saturated sample

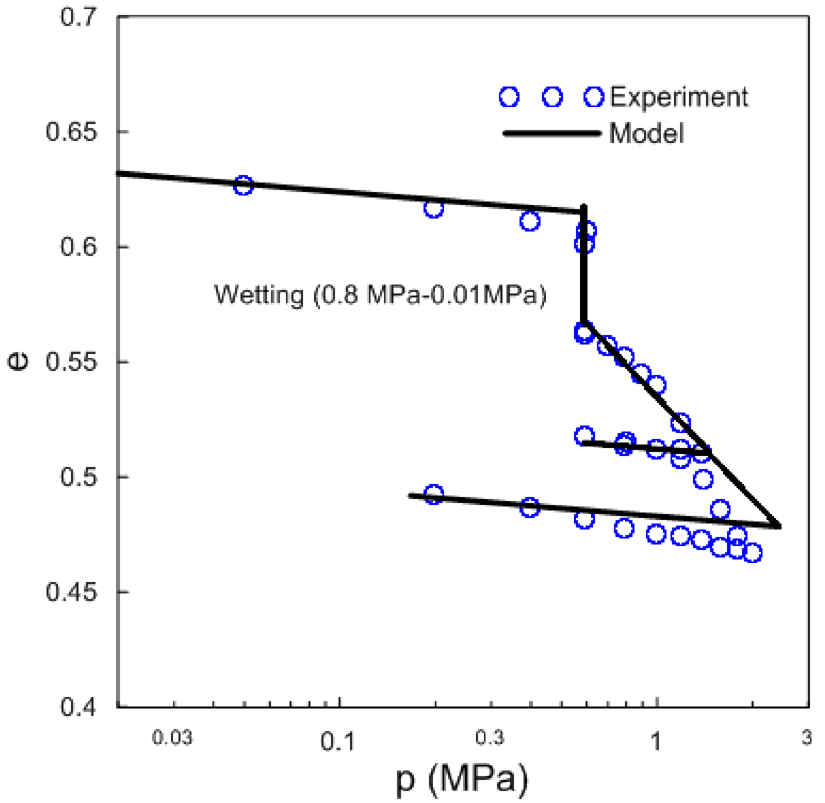

Figure 5-8 Isotropic loading on unsaturated sample

Figure 5-7 and Figure 5-8 shows the simulation results together with experimental observations. The agreements between test and modeling results are very satisfactory, with some small differences in the last steps of loading (i.e. after the reloading stage). The saturated soil at high stress appears to be more compressible, which is not a typical soil behavior, and obviously a critical state model cannot capture this particular feature observed in this experiment. Regardless of this slight difference, the global performance of the model in the isotropic tests involving changes in *p'* and *s* can be considered reasonable, including the simulation of the volumetric collapse compression strain upon wetting.

The determination of the parameters associated with the deviatoric behavior is based on a series of triaxial compression test conducted at different confining stresses and suctions on this type of soil. Figure 5-9 compiles shear strength results from triaxial tests conducted on the Barcelona clayey silt specimens at different confining stresses and suctions. From this experimental data, it was determined that M=1.155 and k_s=0.42. Finally, the parameter α is calculated from M, κ and $\lambda_{(0)}$ (Alonso et al. 1990)

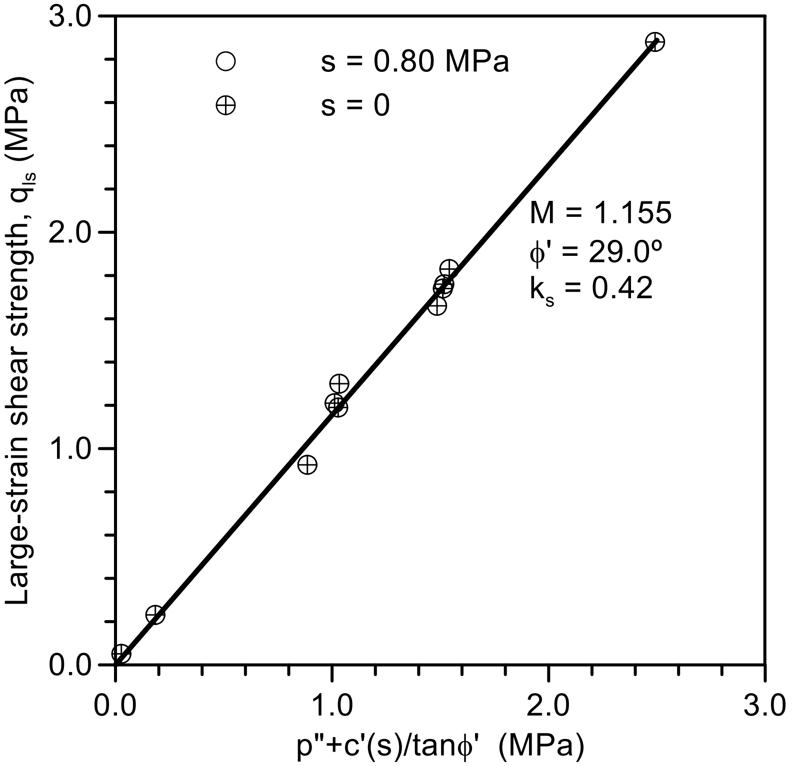

Figure 5-9 Experimental results related to Barcelona clayey silt shear strength compiled from triaxial tests

Table 5-1 lists all the BBM parameters adopted in this investigation. More details about the parameters associated with the BBM and their determination can be found elsewhere (Alonso et al., 1990; D'Onza et al., 2011; Gallipoli et al., 2010; Wheeler et al., 2002).

Table 5-1 Material parameters used in the simulation (BBM)

Parameter	Value	Parameter	Value
κ_s	0.0015	p^c	0.07 kPa
κ	0.005	v	0.33
λ (0)	0.085	M	1.15
p^*_0	0.071 MPa	α	0.6
γ	0.78	k_s	0.42
β	135 MPa^-	λs	0.0078

5.3.3 Main experimental and modeling results

In this part, the detailed experimental results from Test A, B, C and D are presented together with the modeling results. The stress path before shearing stage are analyzed using BBM in detail first and the stress strain curves during shearing are plot together to show the model's overall performance. Two additional triaxial test conducted on two partially saturated soil specimens at different confining were presented to further validated the modeling results.

In connection with test A, the suction decrease (A2→A3 in Figure 5-10) induces a volume reduction with important irreversible volumetric strains (collapse compression). The next scanning drying path induces shrinkage (A3→A4 in Figure 5-10) with no (apparently) irreversible component. Most of the collapsible strains develop at suction values lower than 0.1 MPa, affecting t related to the yield curve LC curve. The modeling results shows satisfied agreement with the experimental data.

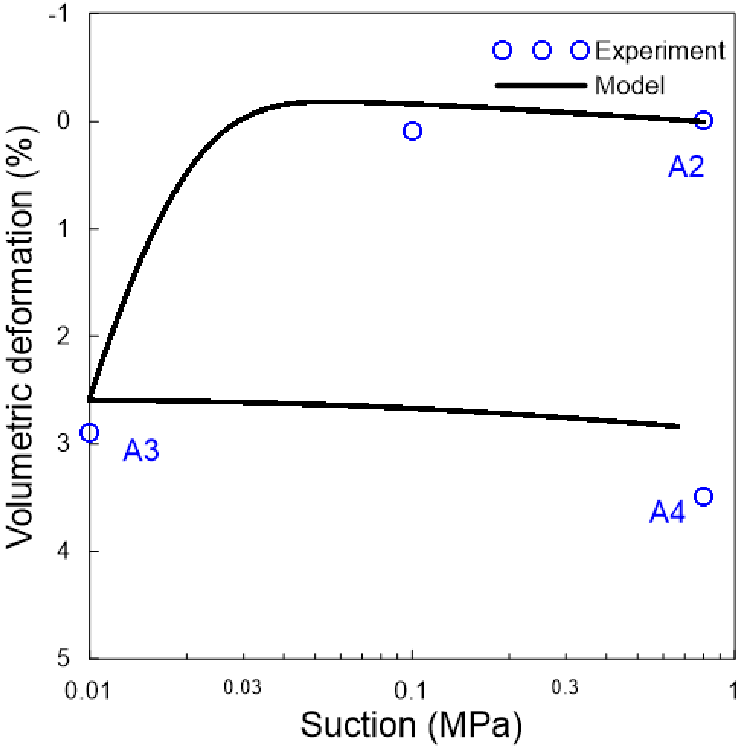

Figure 5-10 Variation of volumetric strain with suction (A2→A3→A4)

Figure 5-11 shows the LC curve and yield surface evolution during the wetting and drying processes. During the wetting process, collapsible strains (plastic strain) was induced which caused the moving of the hardening parameter p_0^*. This implies that the initial *LC* locus move to the final position LC after the wetting. The drying process only produce small elastic deformation which has no influence on the final yield surface before shearing. In this way, during the initial phase of the shearing stage only elastic strains will be developed and plastic strains will only appear after dragging the yield surface. As observed, the selected *LC* curve is able to satisfactorily capture the volumetric collapse compression strains observed upon wetting.

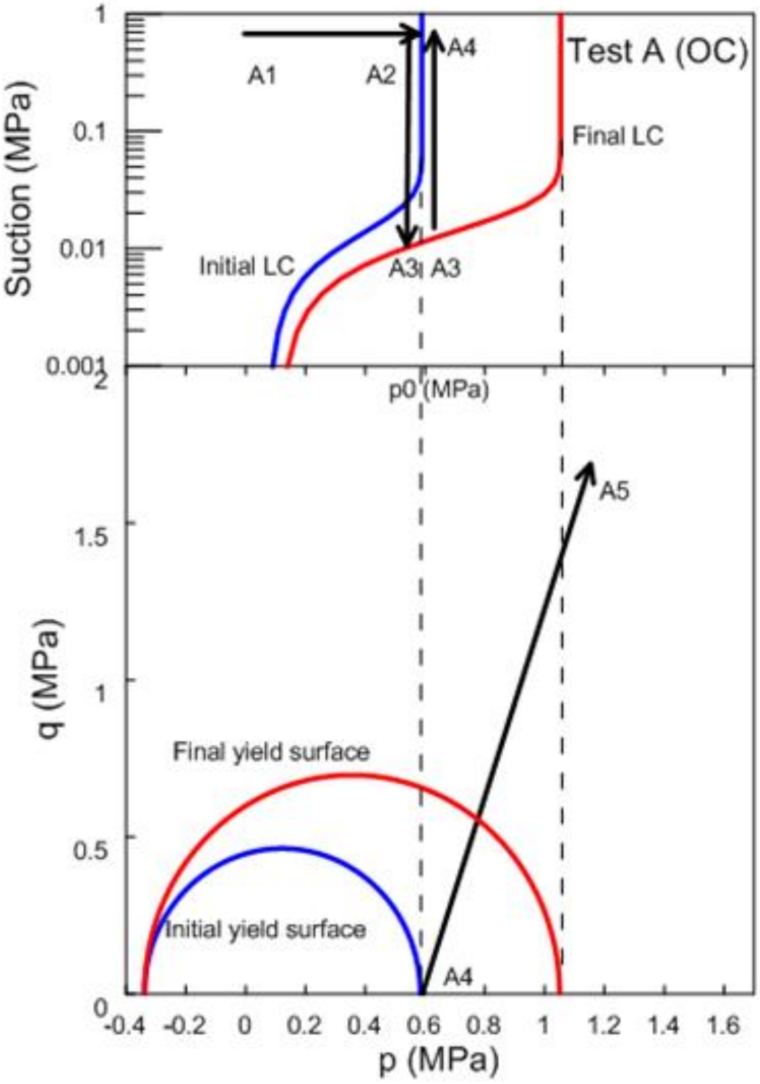

Figure 5-11 Evolution of LC and yield surface (A2→A3→A4)

Figure 5-12 presents the variation of volumetric strains that undergoes the sample upon applying loading / unloading cycle at *s* = 0.80 MPa (i.e. path C1 → C2 → C3). The volumetric strain behavior displays clear pre- and post- yield zones. A yield stress is identified around p_0 = 0.60 MPa, which corroborates the maximum fabrication stress attained on isotropic compaction. The selected parameters κ and $\lambda_{(s=0,8MPa)}$ properly reproduces the isotropic loading and unloading behavior observed previous to the shearing stage conducted in this experiment. On loading, the initial *LC* is dragged to the maximum *p* = 1.60 MPa (point C2). Therefore, on subsequent shearing C3 → C4 it is expected that elastic strains will develop only, and plastic strains will appear after dragging the expanded yield surface.

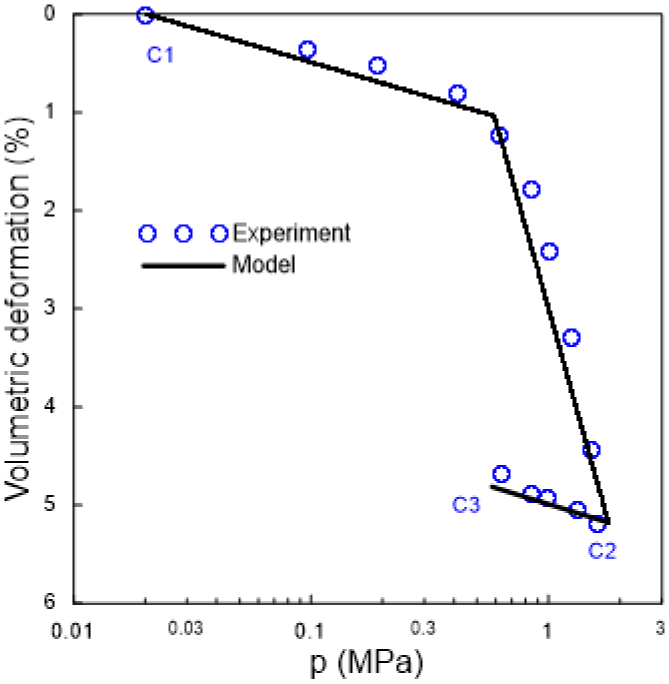

Figure 5-12 Isotropic loading and unloading at constant suction (i.e. cycle path C1 → C2 → C3)

Figure 5-18 presents the volumetric strains associated with the drying-wetting path at constant net stress in Test D (D1→D2→D3). It is expected that since the beginning of the test the drying will induce elasto-plastic deformations. Elastic strains are expected during the subsequent wetting. This test was selected to determine the elastic and plastic parameters associate with suction changes, k_s =0.001 and λ_s. = 0.005, respectively. Based on Alonso et al. (1990), it is assumed that the plastic deformations induced upon drying will also lead to an expansion of the *LC* yield curve because of the hardening induced by the plastic volume reduction of the soil, i.e. Eq. (5-5).

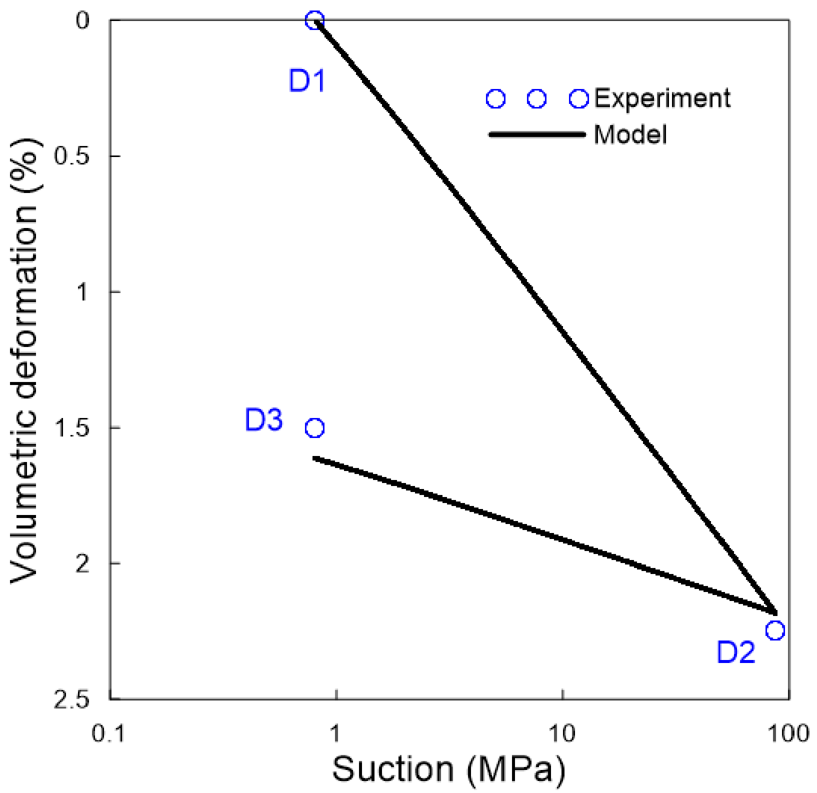

Figure 5-13 Variation of volumetric strain with suction (D1 → D2 → D3).

In summary, the comparisons between model simulations and experimental results of the wetting / drying and loading / unloading paths shown that the tests are qualitatively and quantitatively well-reproduced and the general trend is consistent with the BBM elastoplastic framework.

Figure 5-14 shows the predicted BBM responses on shearing and the experimental results for the different tests. As for the normally consolidated test, the stress point s = 0.8 MPa and $(p_o)_B$ = 0.6 MPa is on the yield surface LC-B at the beginning of the shearing stage (B1→B2 in Figure 5-15). In this test, plastic straining is occurring from the beginning of the shearing. According to the elastoplastic framework, a volume decrease associated with shearing is predicted in test B. The stress-strain curve of test B tends to follow a normally consolidated form of response with no appreciable yield point and with dominant contractive behavior, with dilatant behavior observed at advanced stages of the shearing. The stress and axial strain curves of test A, C and D shows a stiff pre-yield response, which is consistent with the initial elastic stress path lying inside the yield surface, which was dragged by the previous p and s paths involved in those tests (OC state). In those tests, the soil volume initially contracts, but at axial strains around 6 % the samples clearly dilate without displaying a strain softening behavior.

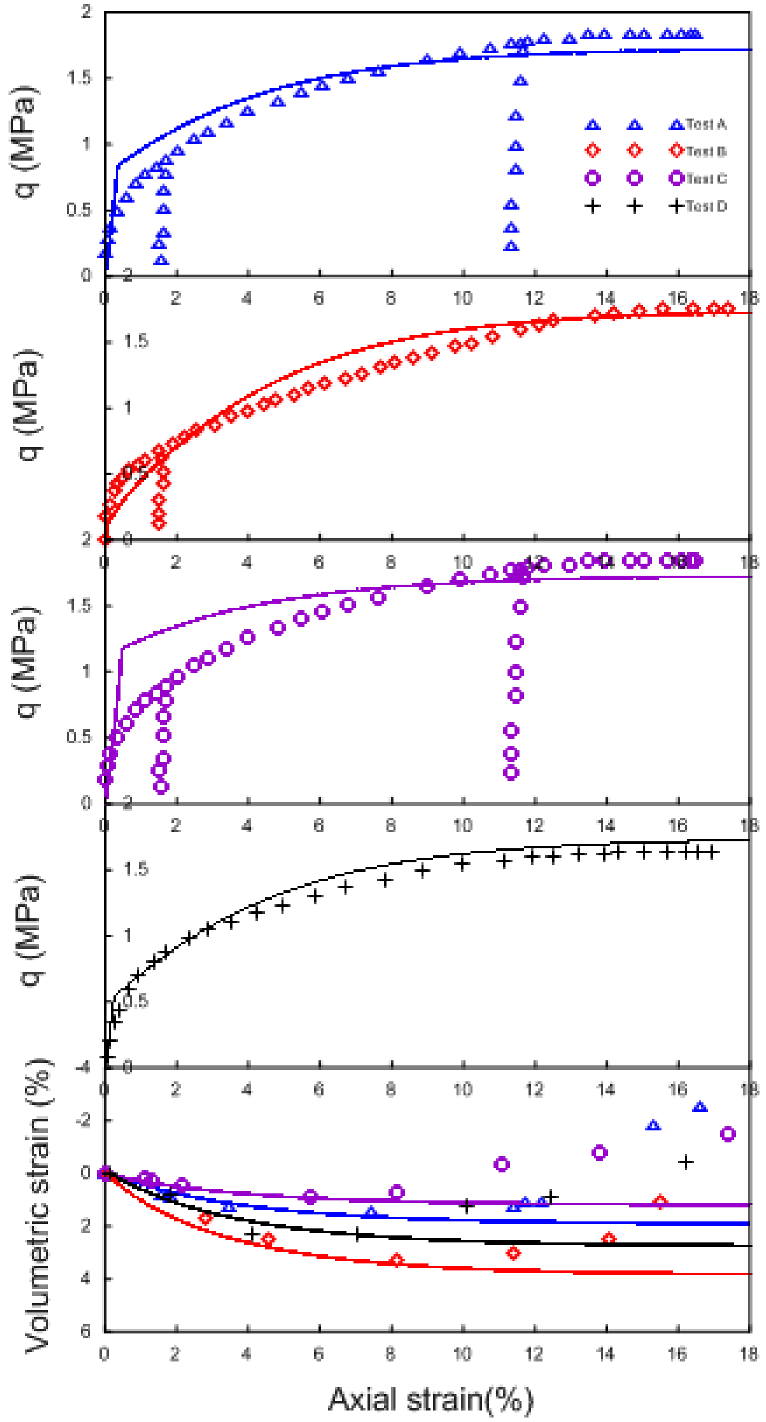

Figure 5-14 Simulation of the shearing paths BBM

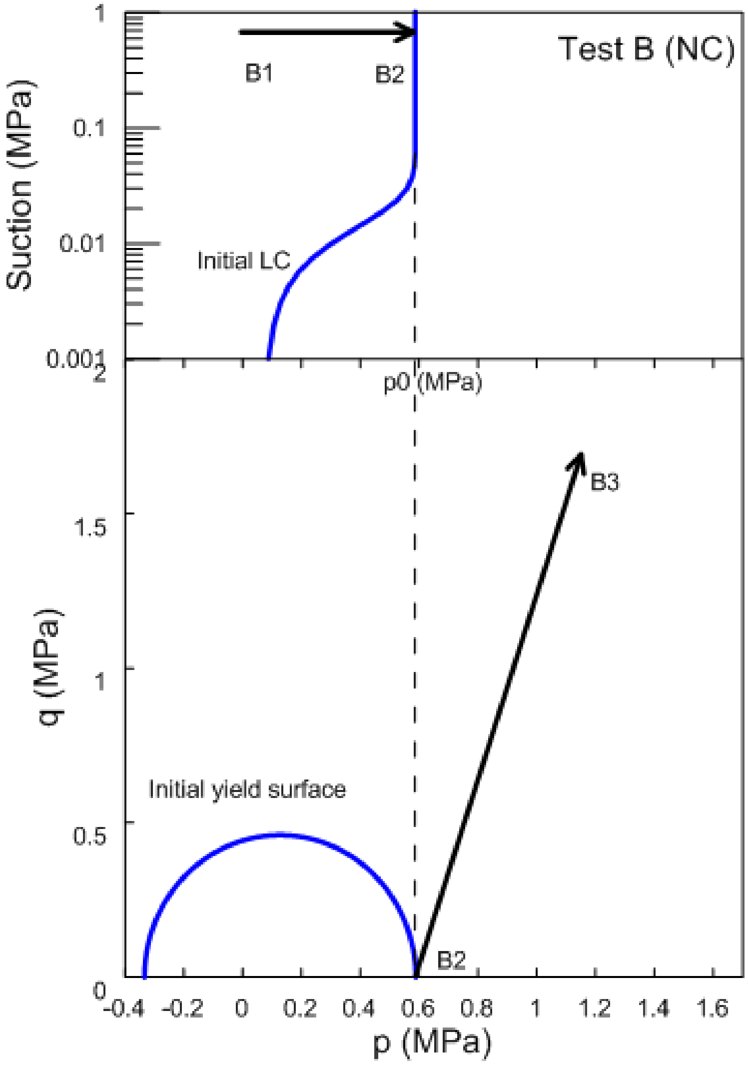

Figure 5-15 Evolution of LC and yield surface (B1→B2)

The gradual plastic straining involved from the beginning of the stress and axial strain curve of test B, as well as the stiff pre-yield response of tests A, C and D, are adequately reproduced. However, yielding is very sudden on the predicted curves and further refinement is necessary to provide a smoother transition. A satisfactory agreement from a qualitative point of view can also be observed regarding the volume change behavior at initial stages of shearing (i.e. less than 5%). The predicted normally consolidated behavior of test B displays a notable contractive response, which becomes less important in the lightly overconsolidated states. However, the model fails in simulating the observed dilatancy at medium/advanced conditions without the ability of predicting the observed strain softening. An upgraded model is proposed in the next section to overcome these problems and to achieve a closer modeling of the experimental results.

5.4 Enhanced BBM with sub-loading concepts

In this section, an enhanced BBM model is introduced. The highlight of the new model includes sub-loading concept (Hashiguchi, 1977, 1989) and new hardening parameter evolution law. The main components of the upgraded BBM are presented first, followed by the validation of the proposed approach using the experimental results modelled in the previous sections, plus some additional ones.

5.4.1 Enhanced BBM Model formulation

In the new formulation, the yield surface is slightly modified to include sub-loading concepts, as follows:

$$F = \frac{q^2}{M^2} + (p+p_s)\left(p - Rp_0\right) \tag{5-6}$$

where p is the mean net stress, q the deviator stress and s the suction, R is the sub-loading ratio ranges from 0 to 1. M is the slope of critical line in the q-p space.

In this equation, $p_s = k_s s$ is related to the increase in apparent cohesion with suction and p_0 is the yield stress for isotropic stress conditions that is related to the applied suction through:

$$\left(\frac{p_0}{p_c}\right) = \left(\frac{p_0{}^*}{p_c}\right)^{\frac{\lambda(0)-\kappa}{\lambda(s)-\kappa}} \tag{5-7}$$

where $p_0{}^*$ the yield net stress for saturated conditions, is the hardening parameter and $\lambda(s)$ is the slope of the virgin compression line for isotropic conditions. $\lambda(s)$ is related to suction through:

$$\lambda(s) = \lambda(0)\left[(1-\gamma)\exp(-\beta s)+\gamma\right] \tag{5-8}$$

$\lambda(0)$ is the slope of the virgin compression line for saturated conditions, κ is the slope of the (elastic) isotropic unloading – reloading paths and p_c is a reference stress. *r* is a parameter controlling soil compressibility and β provides the rate of change of $\lambda(\sigma)$ with *s*.

It is assumed in the model that isotropic hardening is controlled by plastic volumetric and shear strains ($d\varepsilon_v^p$,$d\varepsilon_q^p$)

$$\frac{dp_0{}^*}{p_0{}^*} = \frac{1+e}{\lambda-\kappa} d\varepsilon_v^p + Ds\frac{1+e}{\lambda-\kappa} d\varepsilon_q^p \tag{5-9}$$

Where $d\varepsilon_v{}^p$ is plastic volumetric strains and e is void ratio. *Ds* is an experimental parameter. This expression is similar to many previous models proposed (Roberto Nova, 1988; R Nova & Wood, 1979).

The evolution of the sub-loading ratio *R* is expressed as follows:

$$dR = -\mu lnR\left|d\varepsilon^{p}\right| \tag{5-10}$$

where $d\varepsilon^{p}$ is the increment of total plastic strain; μ is the parameter that controls the rate of the evolution of the sub-loading yield surface.

The soil elastic bulk modulus is calculated as follows:

$$K = \frac{1+e}{\kappa} p' \tag{5-11}$$

Where κ is the slope of the unloading/reloading line in the *e*-log(*p*)’ space. The elastic shear modulus *G* is determined using the following expression:

$$G = \frac{3(1-2\nu)}{2(1+\nu)} K \tag{5-12}$$

where ν is the poisson's ratio.

A non-associated flow rule is adopted:

$$P = \frac{\alpha q^{2}}{M^{2}} + (p+p_{s})\left(p - Rp_{0}\right) \tag{5-13}$$

Where is a constant related to *M*, κ and λ(*0*), which is adopted to predict zero lateral strain for K_0 loading.

Volume changes due to suction in the elastic region is defined as follows:

$$d\varepsilon_{v}^{e} = \kappa_{s} \frac{ds}{s + p_{atm}} \tag{5-14}$$

where κ_s is the compressibility modulus against suction changes. p_{atm} is atmospheric pressure that is added to avoid infinite values as s approaches zero.

Volume changes due to suction in the plastic region is defined as follows

$$d\varepsilon_v = \lambda_s \frac{ds}{s + p_{atm}} \tag{5-15}$$

where λ_s is the compressibility modulus against suction changes in plastic region.

5.4.2 New modeling results

The updated BBM model includes two extra parameters compared with the original BBM. *Ds* is set to be 0.3 and μ equals 100. Figure 5-16 shows the new modeling results with the experimental data. It is clear that the sharp transition between elastic and plastic deformation is eliminated compared with Figure 5-7.

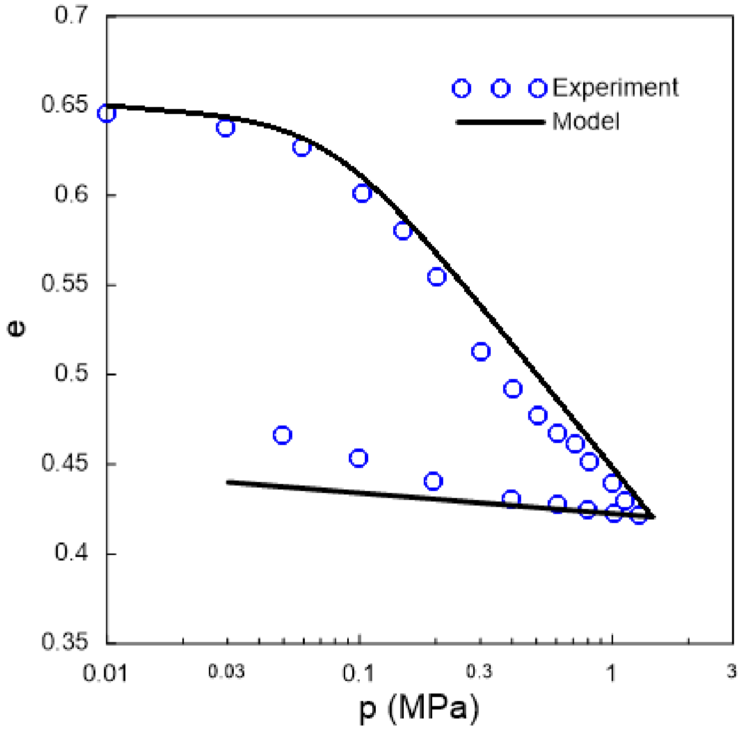

Figure 5-16 Saturated isotropic test, experimental and Enhanced *BBM* result

Figure 5-17 shows the predicted enhanced BBM responses on shearing and the experimental results for the different tests. For test A, there is sharp stress transition between elastic and plastic part which produced using original BBM (Figure 5-15) because of the OC state. In the new modeling results, this unrealistic prediction is replaced by a smooth transition between elastic and plastic part. The same comment can be made to Test C and Test D. The stress-strain relationship is captured quite well by the enhanced BBM. For the volumetric deformation, it is noted that the new model not only be able to capture the deformation at the early stage of the shearing (which is accomplished by BBM too), but also captures the dilation behavior in the late stage of the shearing.

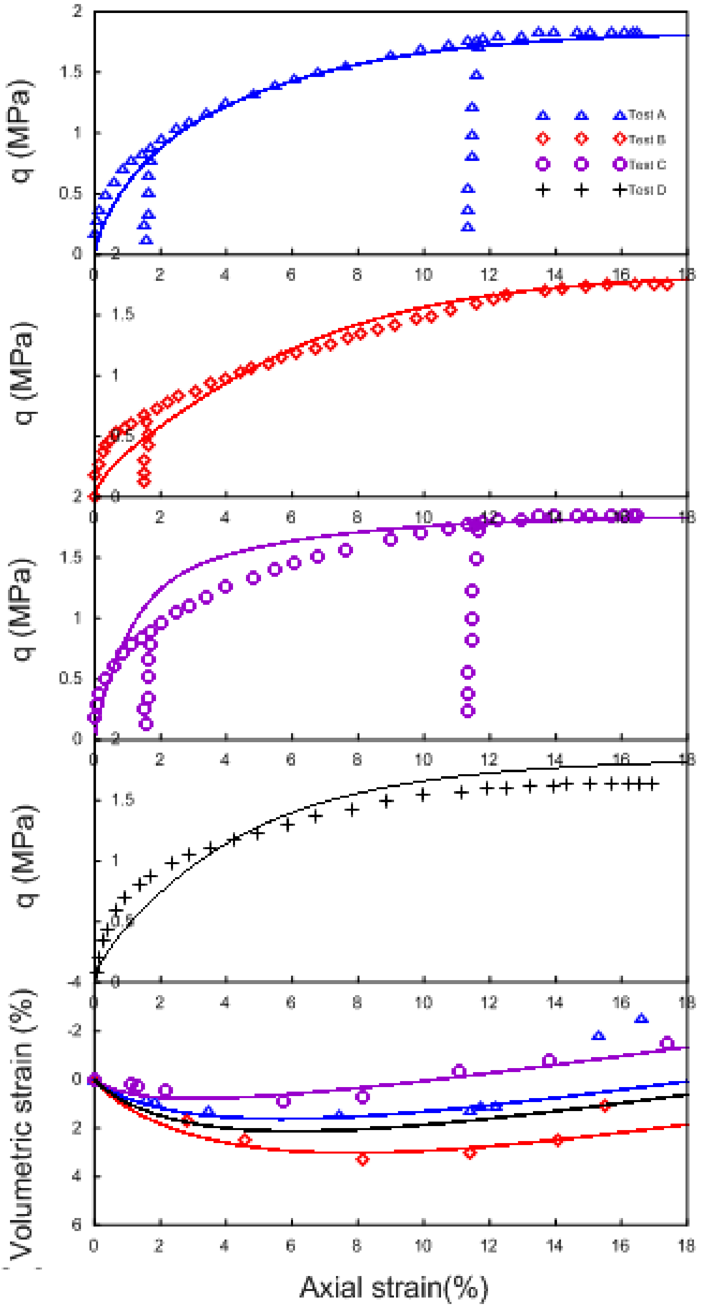

Figure 5-17 Simulation of the shearing paths with enhanced BBM

Two additional triaxial compression tests conducted at different confining pressure were selected to further validate the new model. The NC-0.3 test is sheared at a confining pressure 0.3 MPa, while the OC-1.2 is sheared at initial confining pressure 1.2 MPa. These two tests belong to the similar test as Test B, which is sheared at 0.6 MPa. The suction of all three tests are maintained at 0.8MPa. All the model parameters are kept the same and only confining pressure is changed. Figure 5-18 shows the modeling results together with the experimental data. It is clear that the enhanced model is able to capture the behavior of the studied partially saturated clay silt both qualitatively and quantitively.

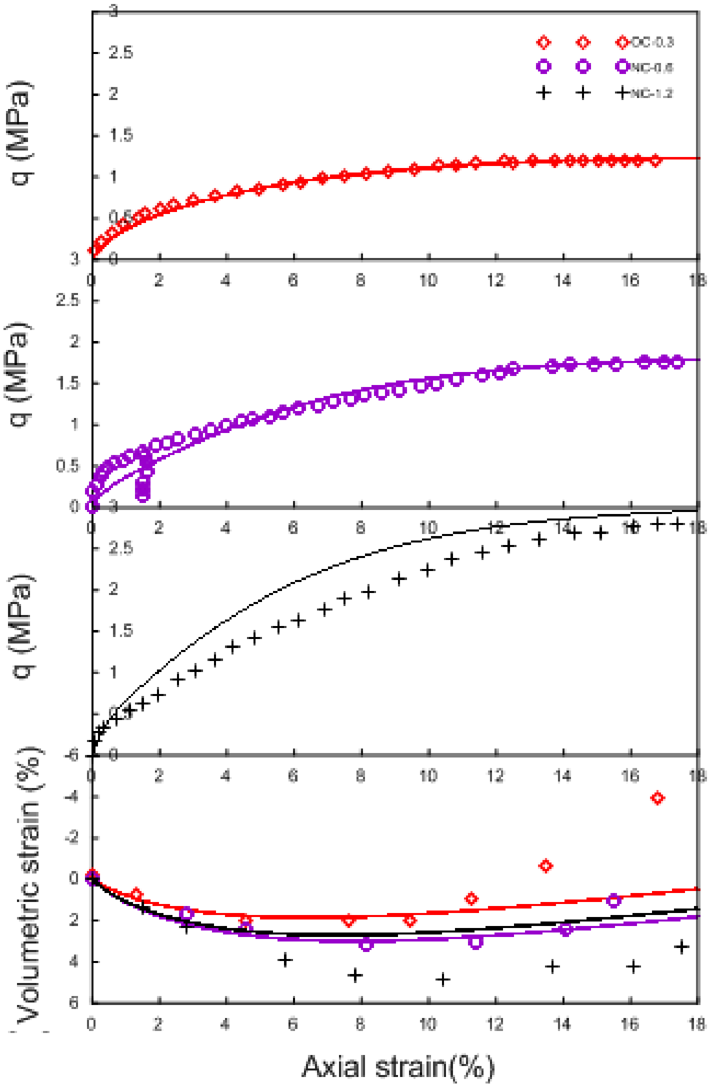

Figure 5-18 Shear at different confining pressure (0.3, 0.6, 1.2 MPa)

5.5 Conclusions and discussion

Suction-controlled triaxial tests were conducted to investigate the mechanical behavior of partially saturated clay silt. Different suction-stress paths were produced in the experiments and the mechanical response of the soil is recorded. The samples are subjected on different hydraulic (wetting/ drying) and isotropic loading path before shearing to examine the influence of suction variations on the mechanical response of partially saturated soil. It can be concluded that the soil can become lightly over-consolidated under these hydraulic and loading path subjected before shearing. Collapsible and shrinkage(plastic) deformation may occur depending the stress level and suction experienced. The experimental programme was also focused on the determination of the mechanical parameters within the context of the model, which is formulated in the framework of hardening elasto-plasticity and uses two basic variables: the net stress and the suction.

The BBM which unitizes the parameters obtained from the tests was selected to reproduce the soil response tested. From the comparison of the experimental results and modeling results, it showed that the BBM is capable of capturing the response observed in the wetting/drying and loading/unloading test results both qualitatively and quantitatively. The stress-strain response during shearing phase was also reproduced by BBM satisfactorily. The lightly over-consolidated state of soil caused by the various stress path was reflected in the stiff pre-yield response shown in the modeling results and gradual yielding is produced for the normally consolidated sample. However, it failed in predicting the post-yield transition between the contraction and the dilatancy of the ultimate shearing stage, which experienced by all the samples. Further refinements are required to improve the agreement between predicted and observed stress-strain curves by using a different formulation of the flow rule and a gradual transition at yielding between elastic and plastic behavior.

The proposed enhanced BBM successfully eliminated the unrealistic sharp transition produced by the original BBM but kept all the other features which prove to be appropriated in modeling partially saturated soils. The dilatancy of the experienced by the samples at the ultimate shearing stage are also well produced by the new enhanced BBM. It is safe to say that both BBM and enhanced BBM proposed here are valuable tools which is able to provide insight of the mechanical behavior of partially saturated soils and enhance the current understanding of this complex soil system.

6 MECHANICAL BEHAVIOR OF MICP TREATED SAND

6.1 Introduction

Microbially induced calcite precipitation (MICP) is an innovative biomediated soil improvement method that can be used to induce cementation within originally loose and collapsible soils such as sand. Through MICP treatment, bacterially induced calcium carbonate can be generated in the void and at the contact of the soil matrix, thus creating artificial cementation on original soil matrix.

The idea of utilizing MICP as a soil improvement method for geotechnical problems has become popular recently. For example, Whiffin et al. (Whiffin et al., 2007) found significant improvement in the behavior of soils treated with MICP in terms of both, strength and stiffness . The large-scale experiments conducted by van Paassen et al. (L. A. van Paassen, Ghose, et al., 2010) were aimed at investigating the feasibility of MICP as a ground improvement method. It was observed that the stiffness of the treated sand increase significantly.

Recent modeling efforts associated with MICP treated soils have been mainly focused on the prediction of biogeochemical processes and precipitated calcite distribution (Barkouki et al., 2011; Fauriel & Laloui, 2012; B. Martinez et al., 2011; Van Wijngaarden et al., 2011, 2012). Despite the substantial interests in MICP, the modeling of the mechanical behavior of MICP treated soil is still limited. Fauriel & Laloui (Fauriel & Laloui, 2012) developed a bio-chemo-mechanical coupled approach to simulate the behavior of MICP treated soils. The mechanical constitutive model is based on non-linear elastic framework. Feng and Montoya Feng and Montoya (2015) used the discrete element method to study the mechanical behavior of MICP treated sands.

This section focusses on the mechanical modeling of sands treated with MICP. This aspect is a key component for performing realistic analyses of engineering problems involving this type of material. An elastoplastic critical state mechanical model is suggested for simulating the behavior of MICP treated sands. The proposed approach attempts to improve some of the limitations of previous models based on elasticity (Fauriel & Laloui, 2012), with the intention of reproducing more accurately degradation processes and irreversible behaviors typically observed in cemented soils. The model considers specific features of MICP sands, such as the stiffness, strength and dilation enhancement due to the calcite precipitation. The model also introduced the simulation of bond degradation processes and sub-loading concepts. The proposed framework was validated against recently published experiments involving not only MICP samples treated with different calcite ($CaCO_3$) contents, but also under different test conditions (i.e. various confining pressure and loading path). In the following sections, the mechanical behavior of MICP treated sand is briefly reviewed. The rationale and benefits of the adopted elastoplastic framework are introduced afterwards, together with the main features and application of the proposed model to reproduce the behavior of MICP treated sand specimens under different conditions.

6.2 Mechanical behavior of MICP treated sand

Experimental investigation involving MICP treated sands (Barkouki et al., 2011; M. Burbank et al., 2012; Cheng et al., 2013; Chou et al., 2011; J. T. DeJong et al., 2006; Feng & Montoya, 2015; H. Lin et al., 2015; Montoya & DeJong, 2015; Tagliaferri et al., 2011; Weil et al., 2011) has revealed that this type of material are stronger and less compressible than the untreated host sand specimens under similar testing conditions. The MICP treated sands exhibit higher shear strength and more dilation under shearing and soften more after yielding. For example, Figure 6-1 presents the stress-strain behavior and strain-volumetric response of untreated and MICP treated sand samples under triaxial drained conditions reported by Montoya et al. (Montoya & DeJong, 2015).

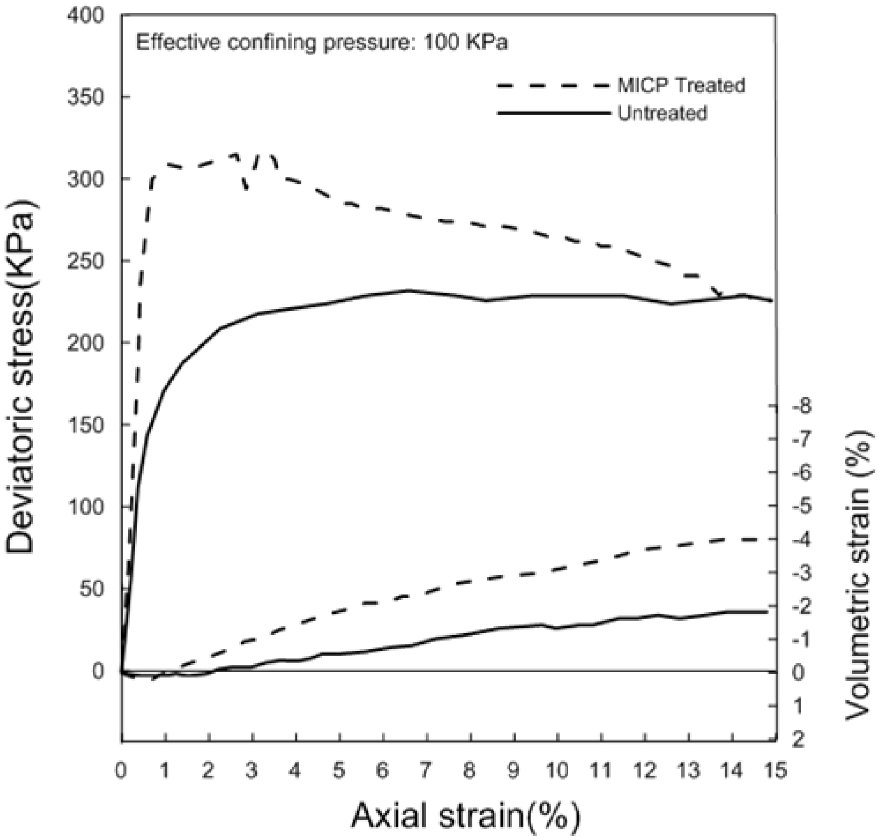

Figure 6-1 Triaxial drained tests involving untreated and MICP treated specimens in terms of stress–strain behavior and volumetric response. Experimental data from (Montoya & DeJong, 2015)

The stiffness, deviatoric peak stress and dilation of the MICP treated sand increased significantly respect to the untreated sample. Furthermore, the increase in precipitated calcite content is generally associated with both, a higher stiffness and strength, as well as with a more marked softening after peak stress and dilation (Figure 6-2). This kind of phenomena can be explained by two related mechanisms: 1) the induced calcite precipitation provides bonding effect between mineral particles, increasing the stiffness and strength of the MICP treated soil; and 2) calcite precipitation not only create larger sized grains (with more kinematic restraints) but also densify the soil by filling the voids between soil particles, leading to a higher dilation when the soil matrix is sheared.

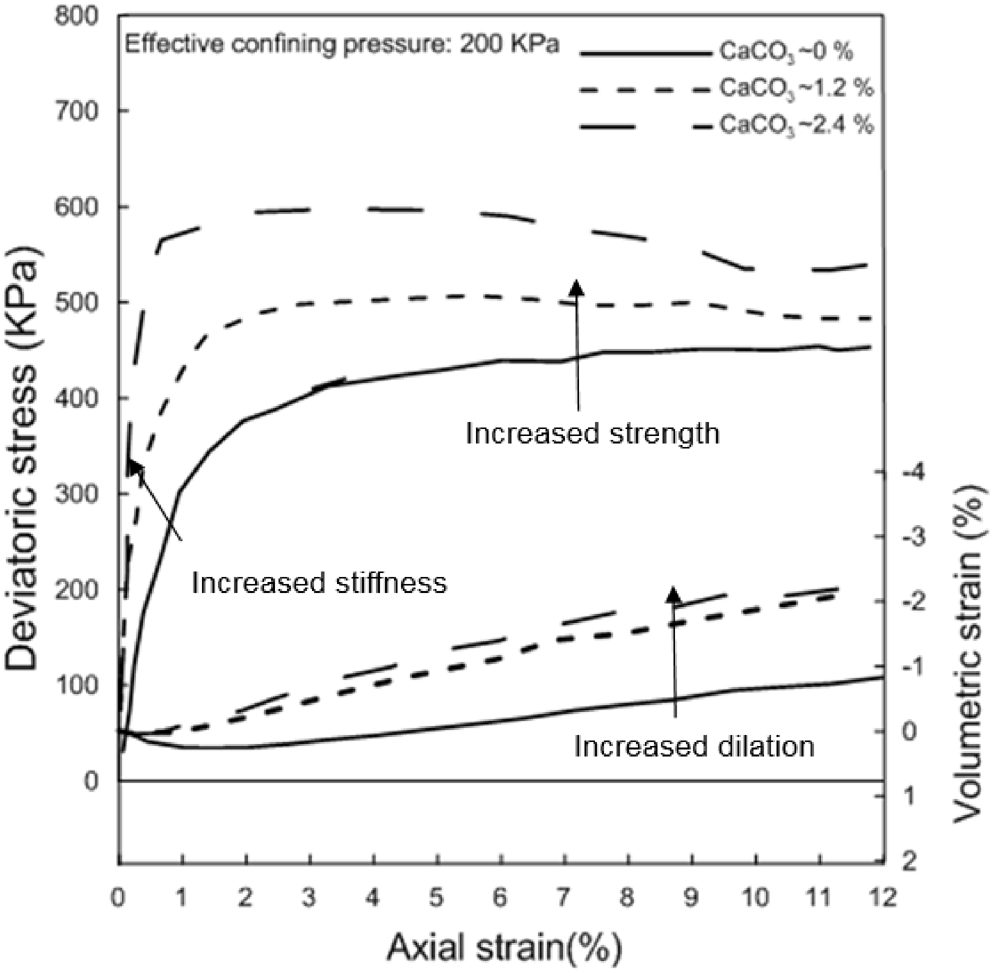

Figure 6-2 Triaxial drained tests on MICP treated specimens with different $CaCO_3$ contents in terms of stress–strain behavior and excess pore pressure response. Experimental data from (Feng & Montoya, 2015)

Another interesting behavior of MICP treated soils is the degradation of the cementation during loading. As shown in Figure 6-3, soil deformations may deteriorate the bonds induced by calcite precipitation which in turn reduces its contribution to the enhancement of stiffness and strength. The degradation of cementation during loading of MICP treated sands has been clearly captured by using the shear wave velocity monitoring technic. (e.g. (J. T. DeJong et al., 2006; Montoya & DeJong, 2015; Weil et al., 2011))

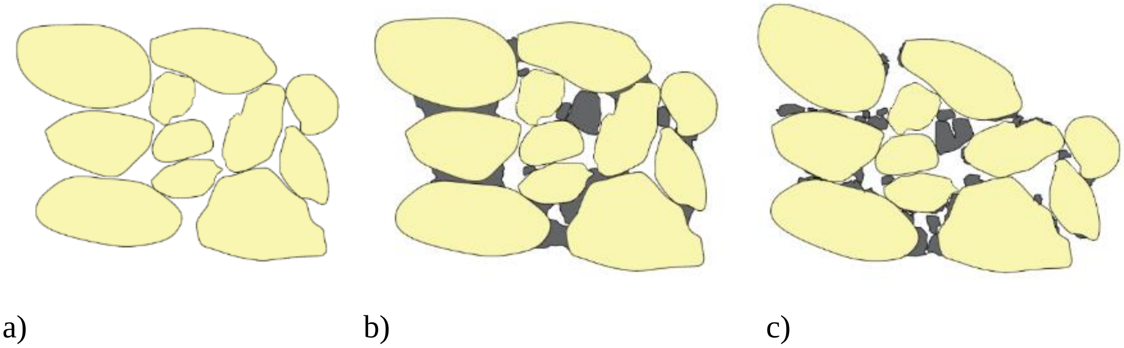

Figure 6-3 Schematic representation of MICP sand: a) untreated sand; b) MICP treated sand; c) damaged MICP treated sand

The spatial distribution of the bonding aggregates ($CaCO_3$) may also influence the mechanical behavior of MICP treated soils (A Al Qabany & Soga, 2013; Cheng et al., 2013; Chou et al., 2011; H. Lin et al., 2015). For example, to investigate the mechanical behavior of MICP treated sands, Lin et al. (2015) performed several sets of triaxil compression tests on MICP treated sand and their results demonstrate that the mechanical properties of MICP-treated sands are not only controlled by the average or bulk $CaCO_3$

content, but also by the spatial distribution of $CaCO_3$ in the pore space of the host sands. Three types of morphology for MICP treated sands were identified through scanning electron microscopy and energy-dispersive X-ray spectroscopy by Lin et al. (H. Lin et al., 2015): a) contact cementing; (b) grain coating; (c) matrix supporting. However, more research is still needed to evaluate the morphology influence on the mechanical behavior of MICP treated sands.

In the following sections, the main components of the proposed elastoplastic framework for MICP sands are discussed in detail, followed by the application of the model in different experiments involving MICP treated sand specimen.

6.3 Model description

The mechanical constitutive model present hereafter is based on the elastoplatic soil mechanics and it includes some ingredients that corresponded to the features of MICP treated sand (i.e. calcite participation cementation effect and bond damage). Sub-loading concepts (Hashiguchi, 1989) are also introduced to account for a more realistic modeling of soil behavior. The proposed model is hereafter named: MICP-Sand model.

6.3.1 Yield surface

There are three yield surfaces involved in MICP-Sand model, namely Modified Cam-Clay (MCC) yield surface, MICP enhanced yield surface and sub-loading yield surface. The MCC yield surface is used to describe the mechanical behavior of sand without MICP treatment as follows (Roscoe & Burland, 1968):

$$F_{MCC} = \frac{q^2}{M^2} + p'^2 - p' p_c \tag{6-1}$$

where *p'* and *q* are the mean effective and deviatoric stresses, respectively; *M* is the slope of critical line in the *q*-*p'* space; *p_c'* is the effective pre-consolidation pressure that is also one of the hardening variables of the model.

The MICP enhanced yield surface considers the mechanical influence of calcite precipitation as a cementation factor. To account for this bonding effect, the hardening parameter p_b is introduced into the model formulation. Subscript *b* refers here to the bond induced by calcite precipitation. This mechanism will induce an isotropic expansion of the MCC yield surface as shown in Figure 4 and expressed by:

$$F_{MICP} = \frac{q^2}{M^2} + p'^2 - p'\left(p_c + p_b\right) \tag{6-2}$$

A linear relationship is assumed here to relate the content of $CaCO_3$ and the mechanical hardening parameter p_b:

$$p_b = a\left(\chi\ m_c\right) \tag{6-3}$$

where m_c is the mass content of the precipitated calcite, obtained as the mass ratio between the precipitated calcite and host sand. The reason to choose $CaCO_3$ mass content here is because this value can reflect the cementation level and can be determined directly from laboratory tests. In Eq. (6-3) *a* is the scaling constant that relates the mass content of $CaCO_3$ with the mechanical contribution of the $CaCO_3$. In Eq. (6-3) χ is the damage factor (i.e. $1 < \chi < 0$) that accounts for the degradation of the cementation during loading. When χ is equal to 1, the cementation induced by the calcite participation is intact, but as the loading process degrades the cementation, χ progressively decreases. As χ aproaches 0, all cementation effects tend to disappear. The proposed evolution law for χ is:

$$d\chi = -\mu\, \chi\, d\varepsilon_q^p \tag{6-4}$$

where $d\varepsilon_q^p$ is the plastic deviatoric strain increment (defined for triaxial conditions as $d\varepsilon_1^p - d\varepsilon_3^p$); μ is a constant that defines the damage rate of the mechanical contribution from calcite precipitation. This evolution law implies that when the MICP treated sand is sheared, the cementation induced by MICP process will be undermined. This trend is consistent with experimental results (i.e.(J. T. DeJong et al., 2006; Montoya & DeJong, 2015)).

The third yield surface considered in the proposed model is the sub-loading yield surface. Conventional critical state model (e.g. MCC model), assumes that plastics strains occur when the stresses reach the yield surface. However, irrecoverable strains are also observed when the stress state is inside the yield surface. It is also well-known that the MCC model predicts a sharp transition between elastic and plastic states (particularly in soils with dilatancy). Thus, the sub-loading yield surface was incorporated to overcome these shortcomings. The expression of the sub-loading yield surface is defined as follows:

$$F_{SUB} = \frac{q^2}{M^2} + p'^2 - R\, p'\left(p_c + p_b\right) \tag{6-5}$$

where R is the sub-loading ratio that ranges from 0 to 1. The sub-loading yield surface is plotted together with MCC yield surface and MICP enhanced yield surface in Figure 6-4.

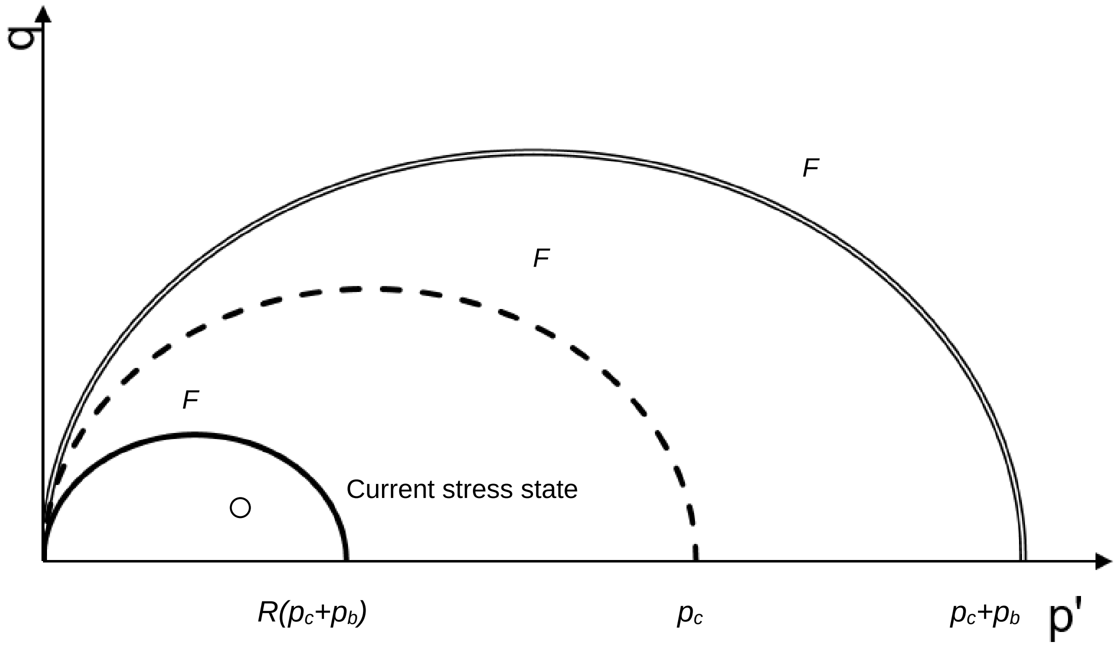

Figure 6-4 Yield surface adopted in the model

As shown in Figure 6-4, the current stress state will stay on the sub-loading yield surface when the soil specimen is loaded thus creating plastic strain in the elastic domain and inducing a smooth transition between compressive and dilative soil behavior.

The evolution of the sub-loading ratio *R* is expressed as follows:

$$dR = -\eta lnR \left| d\varepsilon^{p} \right| \tag{6-6}$$

where $d\varepsilon^{p}$ is the increment of total plastic strain; η is the parameter that controls the rate of the evolution of the sub-loading yield surface.

6.3.2 Stiffness matrix

The soil elastic bulk modulus is calculated as follows:

$$K = \frac{1+e}{\kappa} p' \tag{6-7}$$

where e is the void ratio; and κ is the slope of the unloading/reloading line in the e-log(p)’ space. The elastic shear modulus G is determined using the following expression:

$$G = \frac{3(1-2\nu)}{2(1+\nu)} K \tag{6-8}$$

where ν is the poisson's ratio. Then the elastic stiffness matrix can be expressed as follows:

$$\mathbf{D}^e = \begin{bmatrix} K+\frac{4}{3}G & K-\frac{2}{3}G & K-\frac{2}{3}G & 0 & 0 & 0 \\ & K+\frac{4}{3}G & K-\frac{2}{3}G & 0 & 0 & 0 \\ & & K+\frac{4}{3}G & 0 & 0 & 0 \\ & \mathit{Symetric} & & G & 0 & 0 \\ & & & & G & 0 \\ & & & & & G \end{bmatrix} \tag{6-9}$$

6.3.3 Hardening law and flow rule

The proposed model includes three different strain hardening parameters: p_c, R and p_b. Each hardening parameter has its own strain dependent evolution law. The hardening laws for p_b and R is defined by Equations (6-4) and (6-6). The hardening law for the pre-consolidation pressure p_c is assumed to be depends on the plastic volumetric and shear strains ($d\varepsilon_v^p$,$d\varepsilon_q^p$) through:

$$\frac{dp_c}{p_c} = \frac{1+e}{\lambda - \kappa} d\varepsilon_v^p + Ds \frac{1+e}{\lambda - \kappa} d\varepsilon_q^p \tag{6-10}$$

where λ is the slope of the normal compression line in the *e*-log(*p*)' space. *Ds* is an experimental parameter. This expression is similar to many previous models proposed by (R Nova & Wood, 1979).

For the sake of the simplicity, an associated flow rule is assumed in this paper (i.e. *F* coincide with the plastic potential G_p), so the flow rule can be written as:

$$d\boldsymbol{\varepsilon}^p = \Lambda \frac{\partial G_p}{\partial \boldsymbol{\sigma}'} = \Lambda \frac{\partial F_{SUB}}{\partial \boldsymbol{\sigma}'} \tag{6-11}$$

where Λ is the plastic multiplier and $\boldsymbol{\sigma}'$ is the effective Cauchy's stress tensor; $d\boldsymbol{\varepsilon}^p$ is the increment of plastic strain. A non-associated flow rule can be easily incorporated if necessary.

6.3.4 Stress-strain relation

The stress-strain relationship of the proposed elastoplastic model can be written as:

$$d\boldsymbol{\sigma}' = \mathbf{D}^e \left(d\boldsymbol{\varepsilon} - d\boldsymbol{\varepsilon}^p \right) \tag{6-12}$$

where d$\boldsymbol{\varepsilon}$ is the total strain increment.

The consistency condition is imposed to ensure that the stress state remains on the yield surface during yielding:

$$dF_{SUB} = \frac{\partial F_{SUB}}{\partial \boldsymbol{\sigma}'} : d\boldsymbol{\sigma}' + \frac{\partial F_{SUB}}{\partial \mathrm{p}_c} d\mathrm{p}_c + \frac{\partial F_{SUB}}{\partial \mathrm{p}_b} d\mathrm{p}_b + \frac{\partial F_{SUB}}{\partial \mathrm{R}} d\mathrm{R} = 0 \tag{6-13}$$

Using Equations (6-12), (6-13) and (6-14), the final stress strain relationship can be written as:

$$d\boldsymbol{\sigma}' = \mathbf{D} d\boldsymbol{\varepsilon} \tag{6-14}$$

where **D** is elastoplastic stiffness matrix, which can be expressed as:

$$\mathbf{D} = \left[\mathbf{D}^{e} - \frac{\mathbf{D}^{e} \frac{\partial F_{SUB}}{\partial \boldsymbol{\sigma}'} \left(\frac{\partial F_{SUB}}{\partial \boldsymbol{\sigma}'} \right)^{T} \mathbf{D}^{e}}{\left(\frac{\partial F_{SUB}}{\partial \boldsymbol{\sigma}'} \right)^{\mathrm{T}} \mathbf{D}^{e} \frac{\partial F_{SUB}}{\partial \boldsymbol{\sigma}'} - \frac{\partial F_{SUB}}{\partial \mathrm{p}_{c}} \left(\frac{1+e}{\lambda - \mathrm{k}} \right) p_{c} \left(\frac{\partial F_{SUB}}{\partial \mathrm{p}'} + D_{S} \frac{\partial F_{SUB}}{\partial q} \right) - \frac{\partial F_{SUB}}{\partial \mathrm{p}_{b}} a(-\mu)(\chi m_{c}) \frac{\partial F_{SUB}}{\partial \mathrm{q}} - \frac{\partial F_{SUB}}{\partial \mathrm{R}} (-\eta) \ln\mathrm{R} \left| \frac{\partial F_{SUB}}{\partial \boldsymbol{\sigma}'} \right|} \right] \tag{6-15}$$

The equations above provide the relationship between external strain and effective stress to model the behavior of MICP treated sand. In a general case, the constitutive equation can be implemented numerically in finite element software and perform coupled modeling of MICP soil (i.e. bio-chemo-mechanical coupled model proposed by Fauriel & Laloui (2012)). In this section, the mechanical constitutive model proposed for MICP sands was integrated following the method proposed by Sloan et al. (Sloan, 1987) and all the analysis presented in this paper correspond to the ‘point integration level’ type, because the intention of this contribution is to explore the model capabilities and to validate it.

6.4 Model application

The performance of the proposed model was evaluated against available experimental data involving a variety of laboratory tests. All the experimental data are from recently published works and detailed analyses are presented in the following sections.

6.4.1 Host sand

For most mechanical experimental studies related with MICP treated sand, Ottawa sand is deemed as the most popular choices as it provides the compatible particle size for the microbes to freely move throughout the pore space with sufficient particle contact for cementation to occur ((DeJong et al. 2006). In this study, the experimental results adopted to evaluate the model (Montoya and Dejone 2015, Feng and Montoya 2016) all took Ottawa sand as host sand. Thus, the host sand without MICP treatment from these literatures was firstly selected to calibrate the model parameters.

The proposed model includes eight material parameters with actual physical meaning and 6 of them related to the host sand (κ, λ, M, Ds, ν, η) can be determined directly from experiment. λ and M can be determined from triaxial drained and undrained test. κ can be obtained from consolidation test. Ds is obtained from the dilation at failure from drained triaxial test. p_c' is assumed to vary with confining pressure. The material parameter for the host sand are summarized in Table 6-1. The modeling results together with the experimental results is shown in Table 6-1.

Table 6-1 Model parameters of Ottawa sand (reference soil)

Model parameters for host sand				
$\kappa=0.003$	$\lambda=0.25$	$M=1.09$	$Ds=0.04$	$\nu=0.17$

For the rest of the model parameter, a, m_c and μ are related with MICP treatment. The model parameter a accounts for enhancement effect of m_c on the hardening variable p_b can be directly determined by conducting isotropic tests in samples prepared with different $CaCO_3$ content (m_c). The parameter μ, that controls the effect of shearing on cementation damage, can be back-calculated from triaxial tests on MICP treated sand specimen. The $CaCO_3$ mass content (m_c) can be determined directly from the measuring the weight of dry MICP treated specimen and after acid washing. The estimation of the sub-loading parameter η can be found elsewhere (e.g., Hashiguchi 1988, Sanchez et al. 2017), in short, this parameter controls how much plastic deformation in the elastic region and it can be obtained from triaxial tests. Table 6-2 shows the model parameters related with MICP treatment adopted in the following modeling.

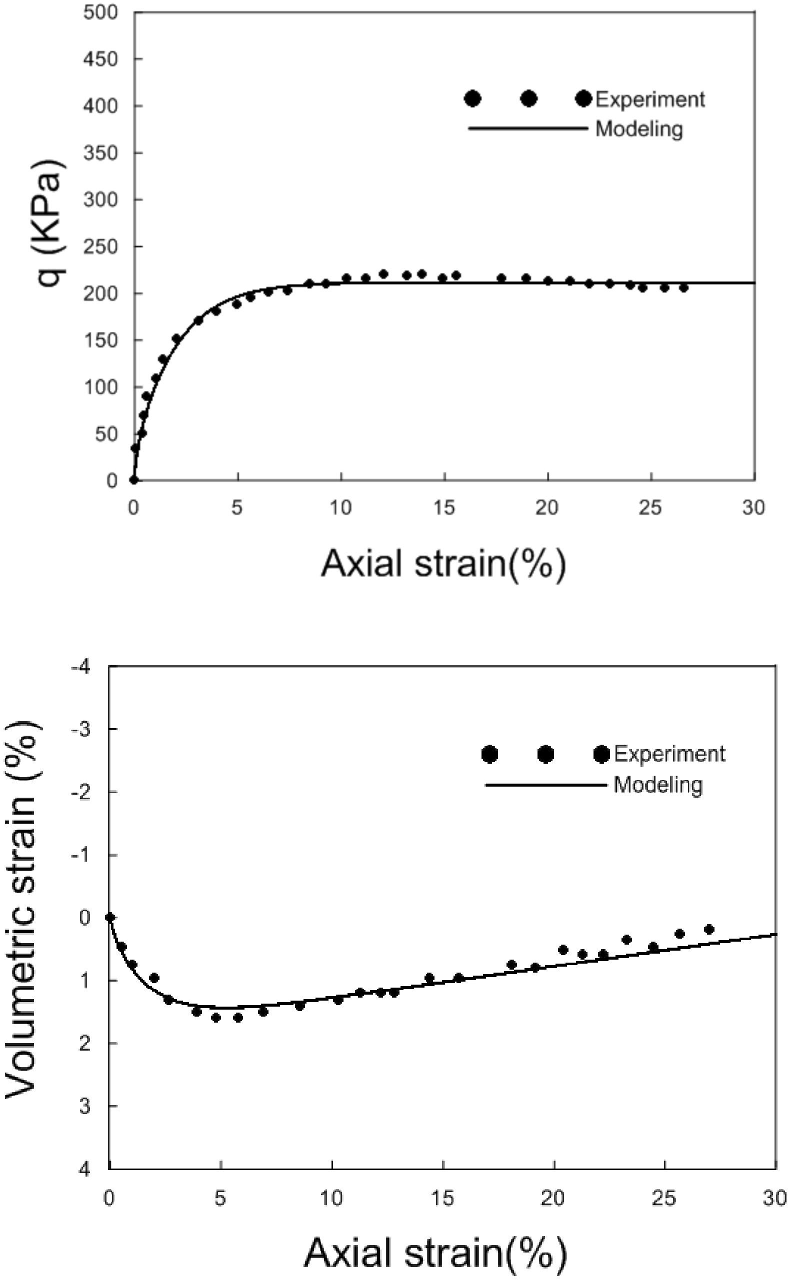

Figure 6-5 Triaxial test results of host sand

Table 6-2 Model parameters related with MICP treatment

Model parameters for MICP treatment			
a=200 *	μ=6.5*	η=60*	m_c=measured from each test

*assumed

Compared with achieving a good fit for each given experiment, which typically requires a trial and error process in order to define a set of material parameters, it is more important to obtain a set of consistent results for a variety of tests using realistic parameters from experiment. In this sense, the developed model may help in gaining a more fundamental insight into the nature of MICP treated sand.

6.4.2 Drained triaxial compression loading tests I

Montoya and Dejone (Montoya & DeJong, 2015) conducted several triaxial drained compression tests by using MICP treated sand specimens. Two sets of triaxial drained tests at 100 KPa confining pressure were conducted to compare the stress strain behavior of the MICP treated sample and the untreated specimen. The treated specimen presented a moderate cementation with a velocity of approximately 450 m/s, while the untreated specimen had an initial shear wave velocity about 180 m/s.

Table 6-3 lists the main soil index properties, alongside the testing conditions related to the samples and experiments.

Table 6-3 Soil index properties and testing conditions

Test	Host type	Effective confining pressure (KPa)	Test condition	Initial void ratio	Mass content of $CaCO_3$ (%)
1	Ottawa sand	100	Drained compression	0.73	0
2	Ottawa sand	100	Drained compression	0.72	1.25

Figure 6-6 presents the experimental stress-strain behavior and volumetric response of the MICP treated and untreated specimens discussed above (on the left), together with the model results (on the right). As shown in Figure 6-6a, the MICP treated specimen exhibits an increase of the peak shear strength when compared against the untreated sample. After reaching the peak strength, the MICP treated soil softens as the cementation degrades with continued shearing. The residual shear strength of the MCIP treated specimen tends to the untreated specimen. The treated specimen exhibits more dilation compared with untreated one. The model performance is satisfactory in terms of the stiffness and peak strength increase due to cementation as shown in Figure 6-6b. The dilation enhanced by the MICP treatment is also captured by the model.

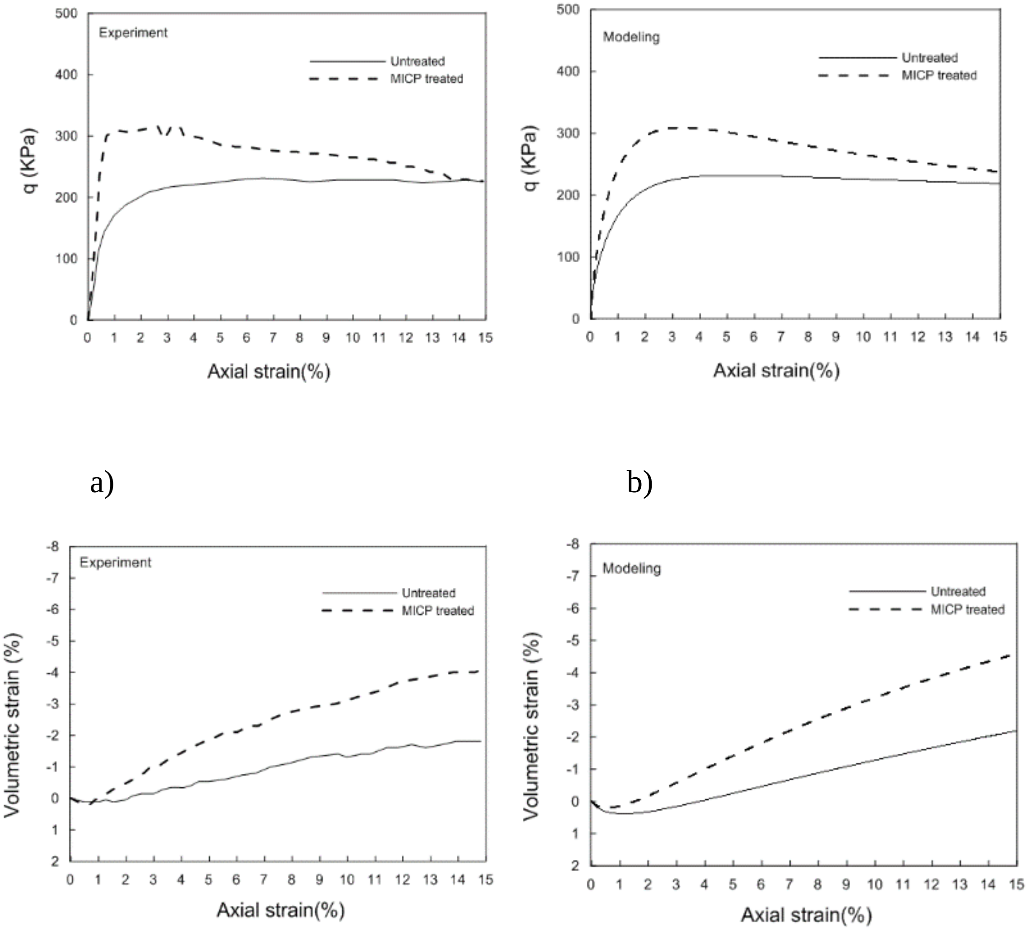

a) b)

c) d)

Figure 6-6 Comparison of experimental and modeling results of drained triaxial compression tests on MICP treated sand (a) stress–strain behavior of the experiment; (b) stress–strain behavior of modeling; c) volumetric response of the experiment; d) volumetric response of the modeling

Figure 6-7 shows the stress path and the evolution of void ratio versus mean effective stress evolution during loading. The plots on the left is experimental data and the computational results is on the right. The stress path of the treated sample in the experiment shows some unexpected changing at the final stage of the experiment which could influence the accuracy of the results. The model capture well the general trend of stress path evolution of both specimen during loading. Both specimens were under compressive deformation at the early phase of the test and started to dilate with continuing shearing. The model reproduced the general trend of the test but with some deviations from the experimental data, particularly at the MICP treated sand specimen. Further examination found that the experimental results of the void ratio evolution for the MICP treated specimen at the late stage is not recorded correctly when compared with volumetric deformation in Figure 6-6c.

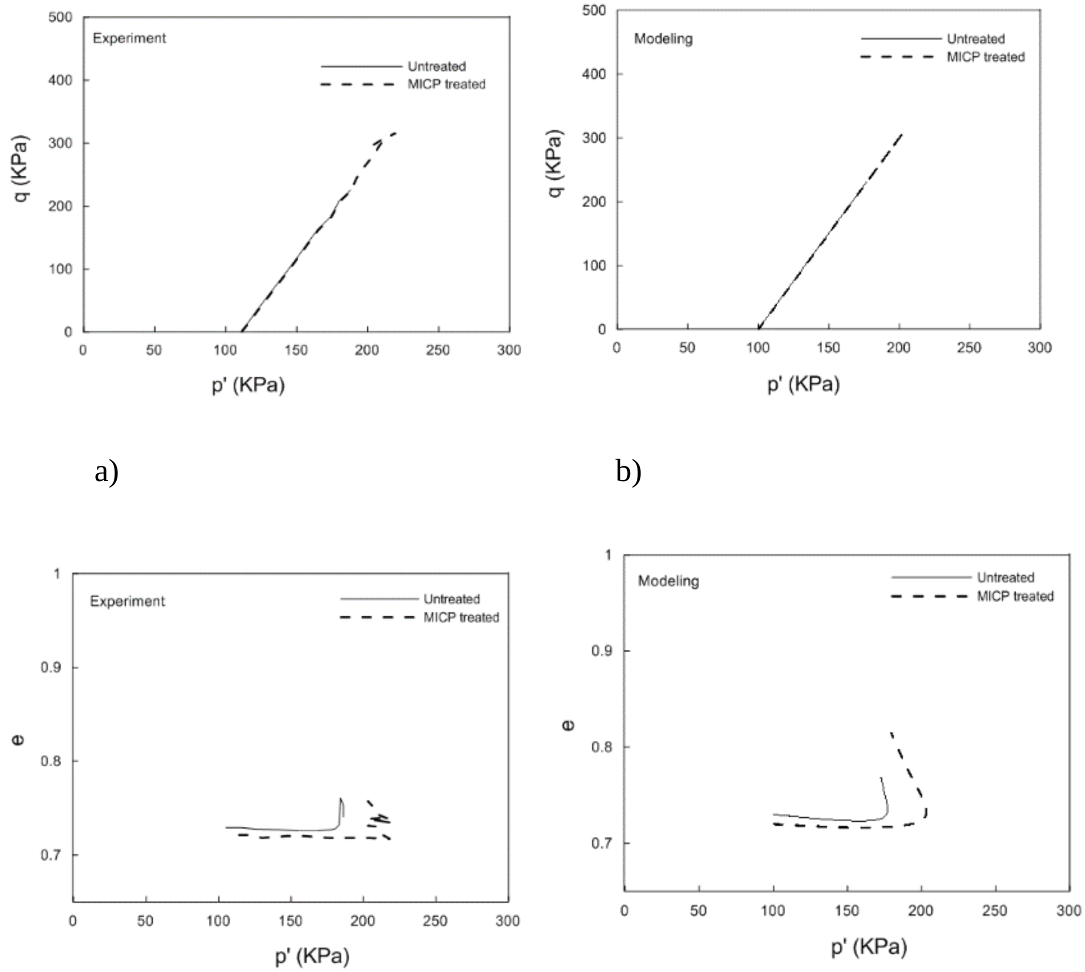

a) b)

c) d)

Figure 6-7 Comparison of experimental and modeling results: a) stress path evolution (experiment); b) stress path evolution (modeling); c) mean effective stress versus void ratio (experiment); d) mean effective stress versus void ratio (modeling)

The evolution of shear wave velocity can (approximately) represent the trend of cementation damage during shearing (Montoya & DeJong, 2015). In the context of the adopted framework, p_b provides an idea that can be considered as an equivalent variable, because it informs about the cementation evolution during loading predicted by the model. Figure 6-8 presents the evolution against the axial deformation of both, the shear wave velocity (i.e. from the experimental study of the MICP treated specimen), and the hardening parameter (i.e., from the modeling of this experiment). A good correlation between these two trends can be observed, implying that p_b can provides a helpful insight about how the cementation degradation evolves in this type of soils.

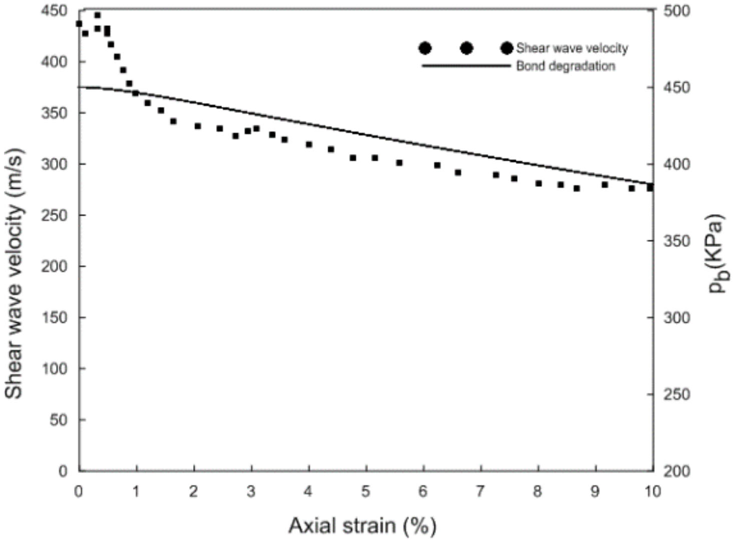

Figure 6-8 Comparison of cementation degradation mechanism of the experiment and simulation

6.4.3 Drained compression loading with various $CaCO_3$ mass content

As discussed in Section 6-2, the increase in precipitated calcite mass content is generally associated with both, a higher stiffness and strength, as well as with a more marked softening after the peak stress and dilation. To illustrate the model's ability to capture this type of behavior of MICP treated sands, triaxial drained compression tests performed by Feng and Montoya (2015) were adopted in this study. Ottawa sand was adopted as the host sand for preparing three MICP treated specimens with different mass content of $CaCO_3$ that were sheared at a constant confining pressure of 200 KPa. The soil index properties, alongside the testing conditions related to these samples are listed in Table 6-4.

Table 6-4 Soil index properties and testing conditions

Test	Host type	Effective confining pressure (KPa)	Test condition	Initial void ratio	Mass content of $CaCO_3$ (%)
1	Ottawa sand	200	Axial compression	0.723	0
2	Ottawa sand	200	Axial compression	0.718	1.2
3	Ottawa sand	200	Axial compression	0.715	2.4
4	Ottawa sand	200	Axial compression	0.709	5.3

Figure 6-9 presents the experimental stress-strain behavior and volumetric response of the MICP treated and untreated specimens discussed above (on the left), together with the modeling results (on the right). It is observed that most of specimens shown a dominant dilative volume change and strain softening behavior at this level of confining pressure. The sample with the higher mass content presents increased dilative behavior. Also in these tests, a marked increase in the initial stiffness and shear strength is observed with the increase of mass content of $CaCO_3$. As shown in Figure 6-9a, the MICP treated samples exhibit a higher stiffness and strength than the untreated specimen. The stiffness and strength enhancement increase with the cementation level. The model manages to reproduce the general behavior by increasing the m_c. As shown in Figure 9c, the dilative volumetric deformation is also increasing with $CaCO_3$ mass content. For the specimen with 5.3 % mass content of $CaCO_3$, it seems to exhibit less dilative volumetric deformation at the final stage of the test as it was shown in Figure 6-9c by crossing the specimens with less $CaCO_3$. This can be explained as follows: for the specimen with 5.3 % $CaCO_3$ the soil particles' movement is localized to the shear band resulting in smaller global volume change.

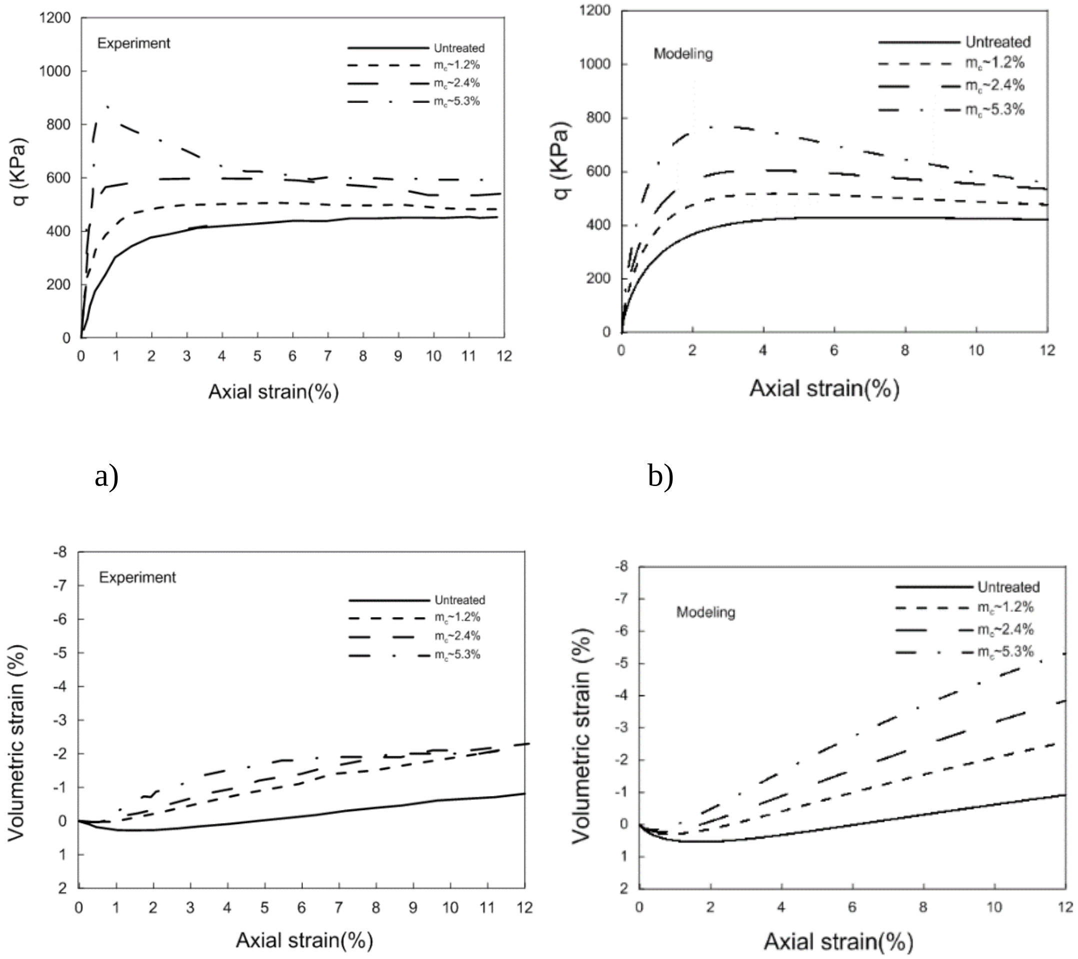

a) b)

c) d)

Figure 6-9 Comparison of experimental and modeling results of drained triaxial compression tests on MICP treated sand (a) stress–strain behavior of the experiment; (b) stress–strain behavior of modeling; c) volumetric response of the experiment; d) volumetric response of the modeling

Figure 6-10 shows additional information of the model regarding the stress path in q/p space with initial, final sub-loading yield surface and boundary yield surface of each case. The stress paths of all these cases start with the same initial sub-loading yield surface and evolves following the typical stress path of a triaxial compression drained test, while staying on the sub-loading yield surface. At the end of the shearing (i.e. 12 % axial strain), different final yield surfaces were reached.

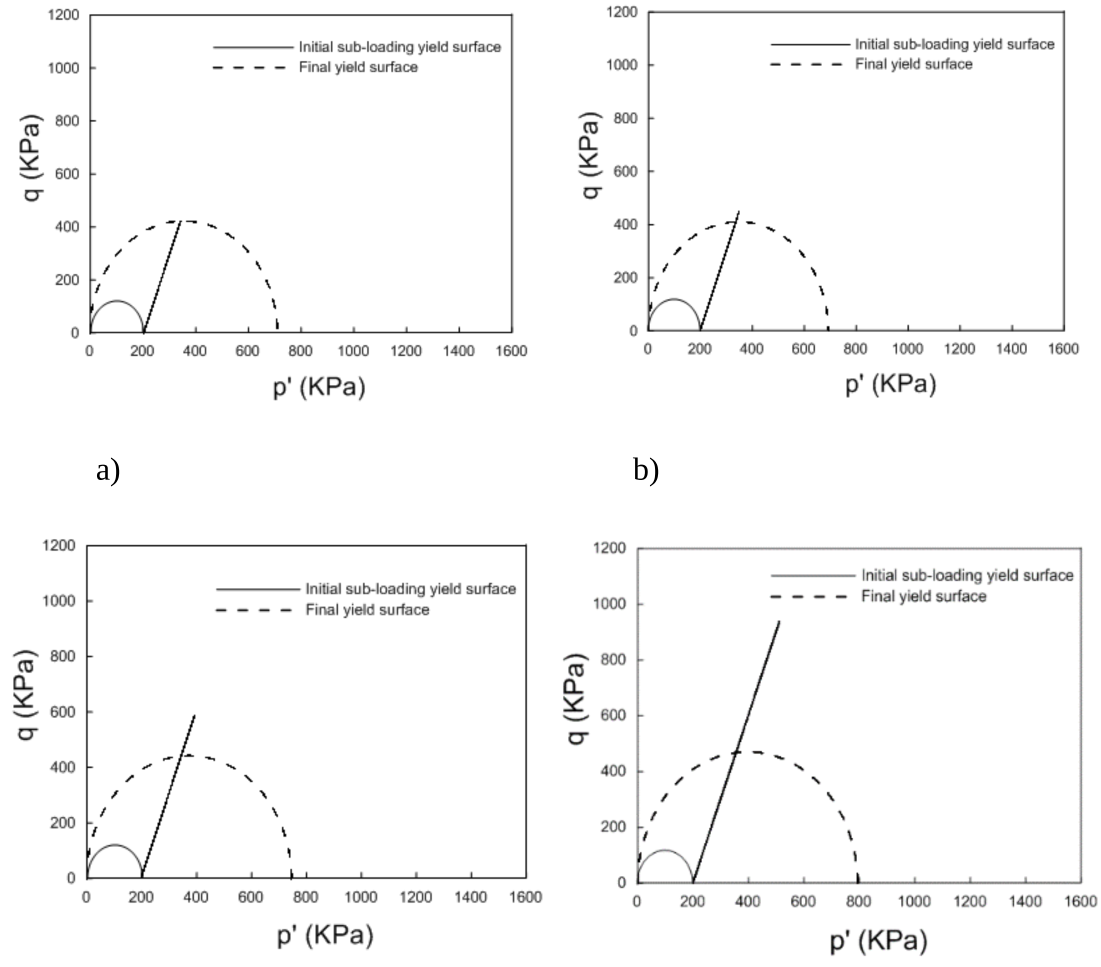

a)

b)

c)

d)

Figure 6-10 Evolution of stress and corresponding yield surfaces. a) untreated;b)1.2% c) 2.4% and d) 5.1%

The plots in Figure 6-11 shows more details about how the main variables of the model evolve for the 2.4 % mass calcite content case. Figure 6-11a presents the evolution of damage factor and sub-loading ratio. As expected, during shearing, damage starts while the sub-loading ratio continue increasing. Figure 6-11b shows the evolution of the effective pre-consolidation pressure, bonding hardening parameter and the effective hardening parameter during the experiment. The effective pre-consolidation pressure increases first, as the stress state lies on the left side of the sub-loading yield surface. Then, it begins to decrease because of the dilative volumetric deformation. The bonding hardening parameter keeps decreasing, as it is controlled by the damage factor. The evolution of the effective hardening parameter depends on the evolution law of χ, R, and p_c. The peak of effective hardening parameter ($R\left(p_c + p_b\right)$) corresponds to the peak deviatoric stress, as shown in Figure 6-11.

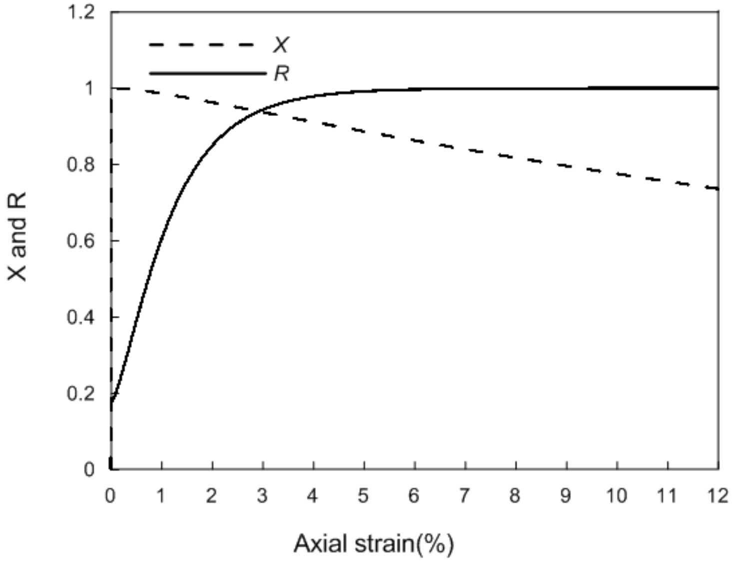

a)

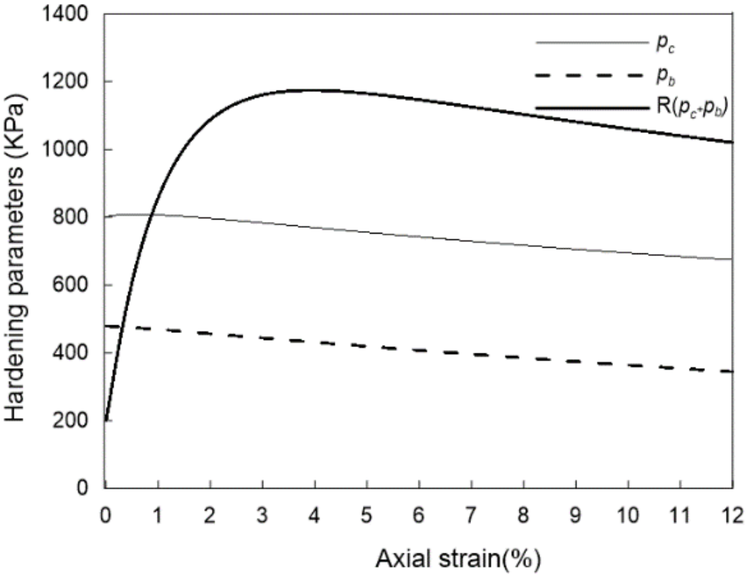

b)

Figure 6-11 Evolution of main variables: a) damage factor (*X*) and sub-loading ratio (*R*); b) effective pre-consolidation pressure (p_c), bonding hardening parameter (p_b), and effective hardening parameter ($R\left(p_c+p_b\right)$)

6.4.4 Parametric study-damage rate

The cementation degradation under loading is observed in MICP treated sands (J. T. DeJong et al., 2006; Montoya & DeJong, 2015; Weil et al., 2011). By tracing the shear wave velocity during the test, the cementation damage process can be captured. It is interesting to notice from the literatures that MCIP treated sand specimen may endure a different rate of damage during shearing. To capture this kind of behavior, a damage mechanism is incorporated into the proposed model. According to Equation (6-4), the cementation effects associated with calcite precipitation will decrease as plastic shear strains accumulate, and μ is the constant that controls the cementation damage rate. In this section, a series of triaxial drained tests adopting same $CaCO_3$ mass content subjected to triaxial conditions (drained) are simulated. The initial confining pressure of all cases is 100 KPa. The mass content of $CaCO_3$ is 2.4%. All the model parameters are the same as the host soil but μ (Table 6-5).

Table 6-5 Different damage rates adopted in this study

Case 1	Case 2	Case 3	Case 4
$\mu= 1.5$	$\mu= 4.5$	$\mu= 8.5$	$\mu= 16.5$

Figure 6-12 shows how the damage rate can be adjusted for tests conducted at the same $CaCO_3$ mass content, illustrating the model flexibility to capture different features of behavior of treated soils. As of the damage rate increases, a lower peak strength is predicted together with more softening. However, the initial stiffness of MICP samples is almost unchanged. Lower dilative volumetric strains are observed with the increase of damage rate.

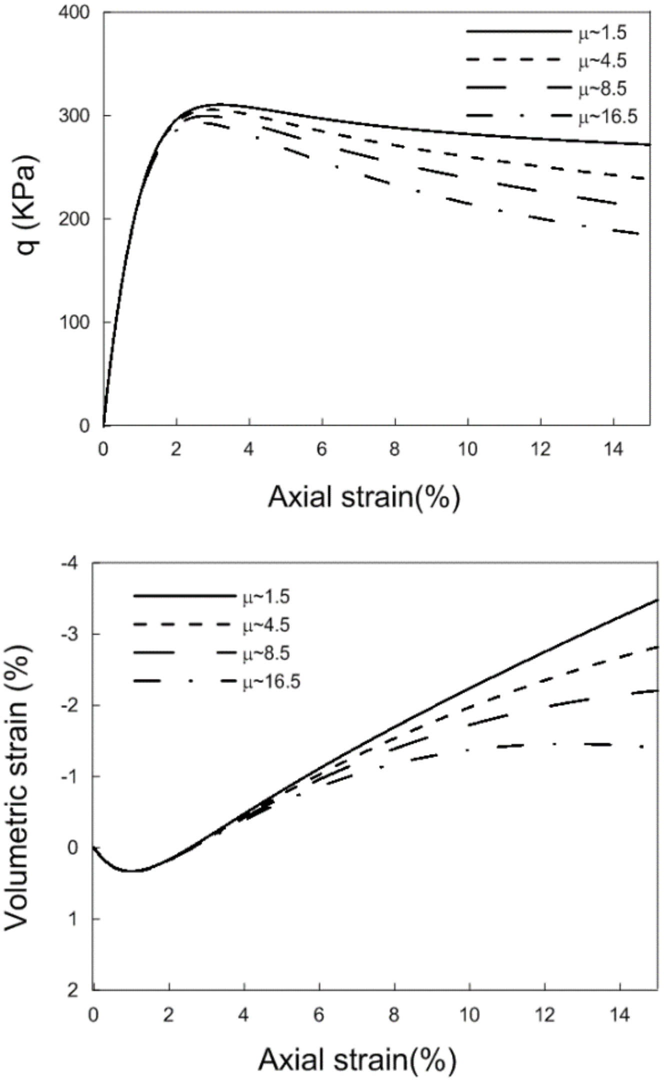

a)

b)

Figure 6-12 Modeling the drained triaxial tests on MCIP treated sand (a) stress–strain behavior, and (b) volumetric response

Figure 6-13 shows the evolution of the main variables (i.e. p_c', p_b, μ, and R) against axial strains during shearing. The bonding hardening parameter decreases more noticeably when a higher value of μ is adopted. The evolution of R is identical for all the cases and it reaches the maximum value (i.e. R=1) around 7% axial strain. In case 1, which corresponds to the lower damage rate, the bonding hardening parameter reaches about 700 KPa at 15% of axial strain. While in case 4 the bonding hardening parameter is around 30 KPa, because of the higher damage rate. The parameter $R(p_c+p_b)$ correspond to the effective hardening parameter which control the stress strain behavior of MICP treated specimen. As shown in Figure 6-13 from case 1 to case 4, the gap between $R(p_c+p_b)$ and p_c is decreasing with the increasing of damage rate. This trend reveals that with the damage of MICP specimen, the sand part of the specimen starts to dominate the mechanical behavior the specimen.

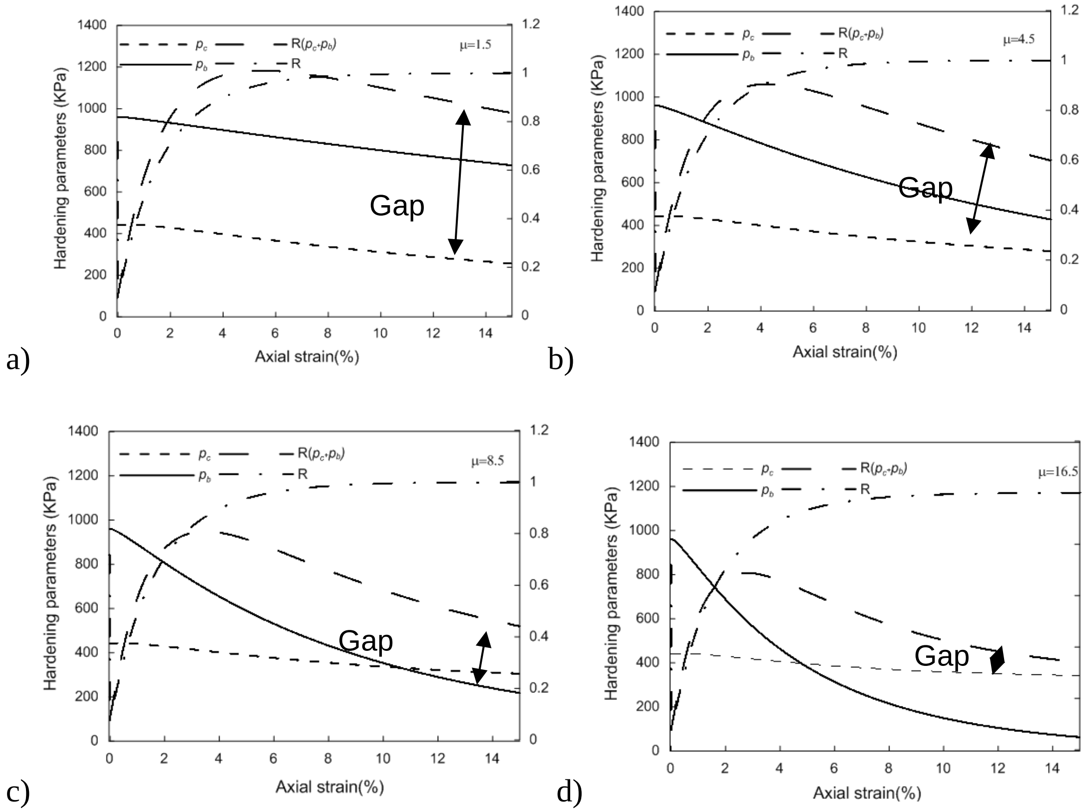

Figure 6-13 Evolution of main model variables (p_c', p_b, μ, and R) against axial strain: a) case 1 b) case 2 c) case 3 d) case 4

6.4.5 Drained loading under various confining pressure

It has been found that the mechanical response of MICP treated sand is also depending on the confining pressure. So it is necessary to check the model's performance in this aspect. Feng and Montoya (2015) performed a series of triaxial drained compression test on MICP treated sand with similar m_ϵ but under different confining pressure. The major test condition and soil index properties are shown in Table 6-6.

Table 6-6 Soil index properties and testing conditions

Test	Host type	Effective confining pressure (KPa)	Test condition	Initial void ratio	Mass content of $CaCO_3$ (%)
1	Ottawa sand	100	Axial compression	0.723	0.9
2	Ottawa sand	200	Axial compression	0.718	1.2
3	Ottawa sand	400	Axial compression	0.715	1.4

Figure 6-14 presents the experimental stress-strain behavior and volumetric response of the MICP treated specimens discussed above (on the left), together with the model results (on the right). It is observed that, at similar cementation level, the mechanical response of MICP treated sand is largely influenced by confining pressure. With the increase of confining pressure, shear strength of the MICP treated sand specimen increased while the dilative volumetric deformation decreased.

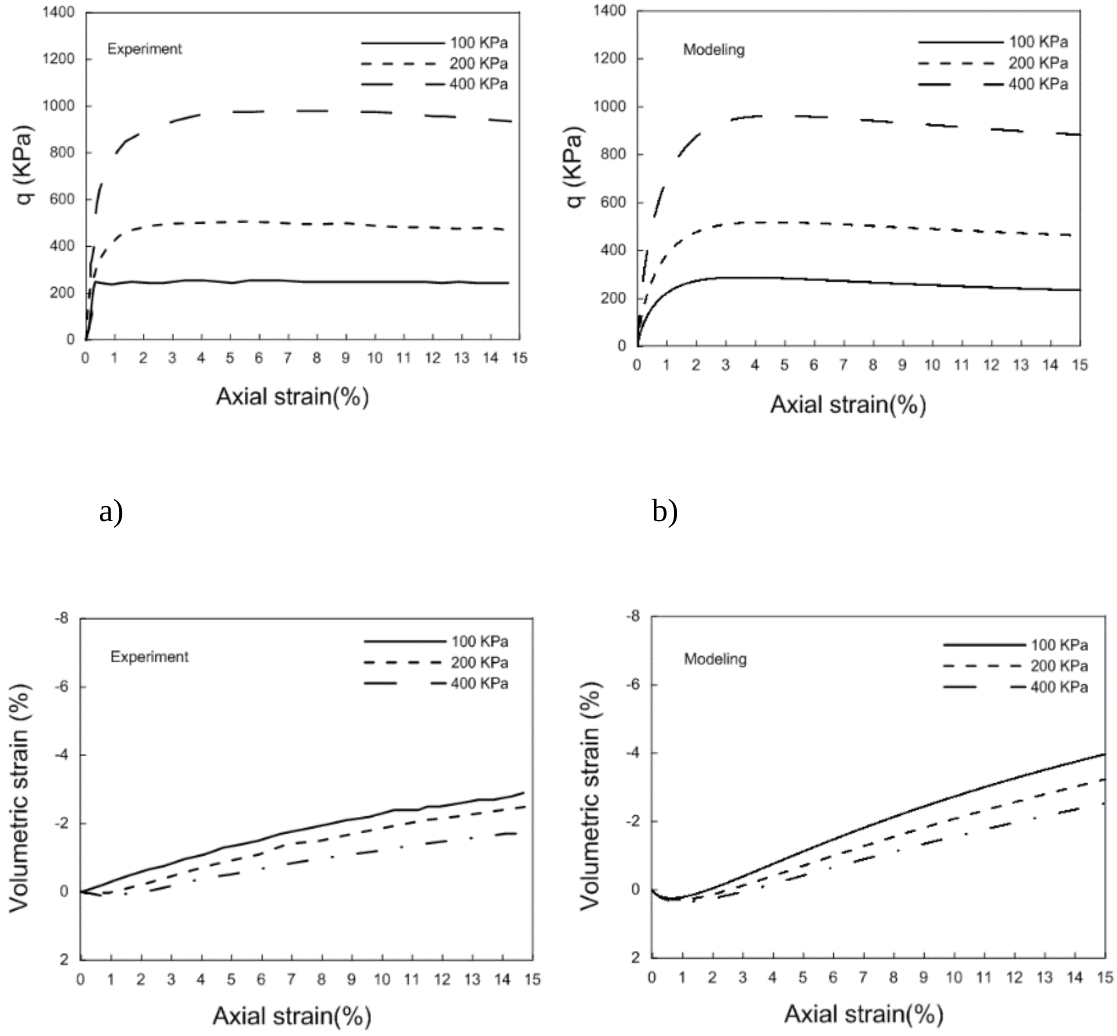

a) b)

c) d)

Figure 6-14 Comparison of experimental and modeling results of drained triaxial compression tests on MICP treated sand (a) stress–strain behavior of the experiment; (b) stress–strain behavior of modeling; c) volumetric response of the experiment; d) volumetric response of the modeling

Figure 6-15 shows the stress path evolution during loading and the evolution of void ratio versus mean effective stress. The plots on the left is experimental data and the computational results is on the right. It is clear to find that the model can reproduce the different stress path and void ratio evolution caused by different confining pressure observed in these experiments.

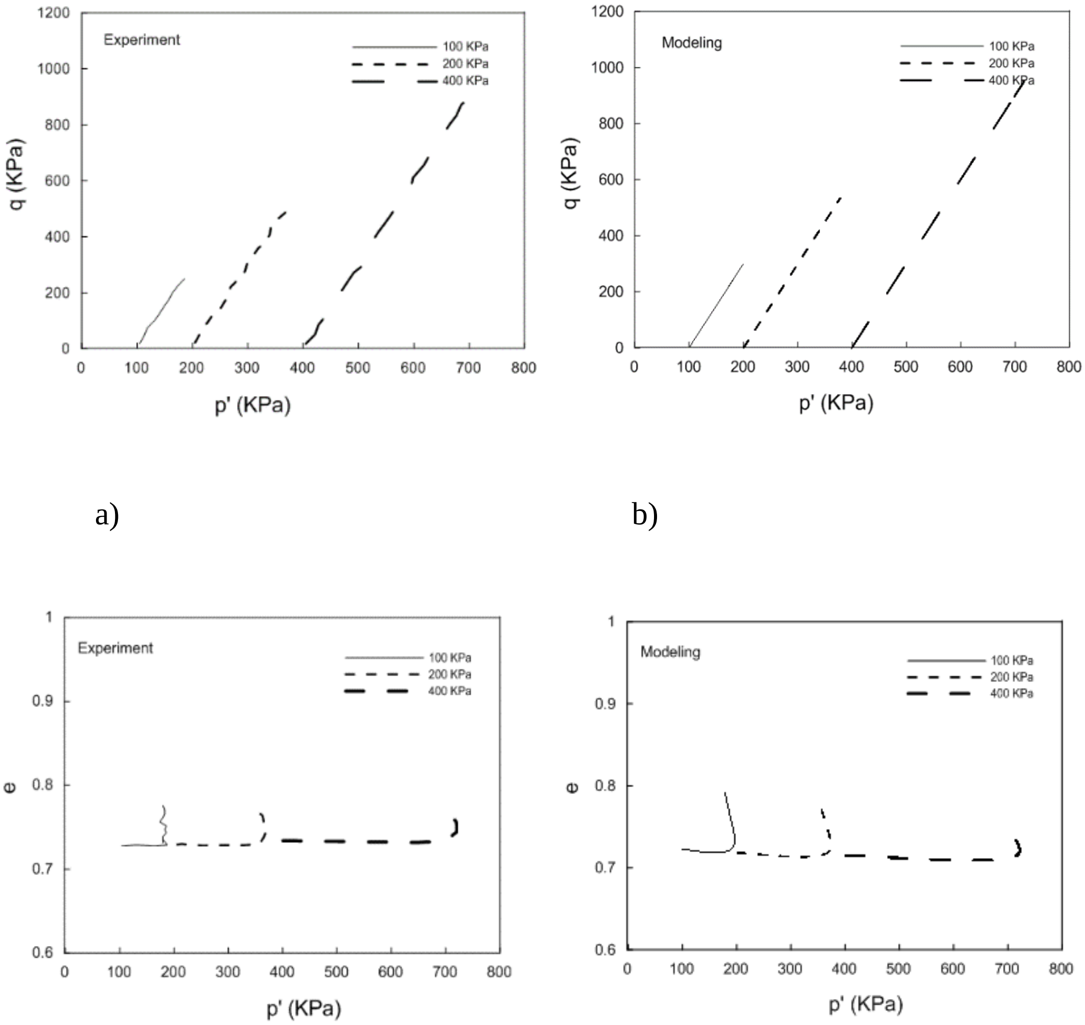

a) b)

c) d)

Figure 6-15 Comparison of experimental and modeling results: a) stress path evolution (experiment); b) stress path evolution (modeling); c) mean effective stress versus void ratio (experiment); d) mean effective stress versus void ratio (modeling)

6.4.6 Drained loading under various loading path

After exploring the proposed models' performance under drained triaxial compression condition, it is necessary to investigate how the model will perform under different loading path. The experiments conducted by (Montoya & DeJong, 2015) were selected in this study. Three MICP treated sand specimen with similar mass content of calcite were sheared under different drained loading paths: axial compression, radial extension decreases, and increasing deviatoric stress while keeping constant mean effective stress. Table 6-7 lists the main soil index properties, alongside the testing conditions related to the samples and experiments.

Table 6-7 Soil index properties and testing conditions

Test	Host type	Effective confining pressure (KPa)	Test condition	Initial void ratio	Mass content of $CaCO_3$ (%)
1	Ottawa sand	100	Axial compression	0.72	1.25
2	Ottawa sand	100	Radial extension	0.72	1.25
3	Ottawa sand	100	Constant p	0.72	1.25

Figure 6-16 presents the experimental stress-strain behavior and volumetric response of the MICP treated and untreated specimens discussed above (on the left), together with the model results (on the right). As shown in Figure 6-16a, the shear strength of MICP treated sand is influenced by the stress path. The commentated specimen subjected to axial compression showed the highest peak and residue shear strength. In contrast, the cemented specimen subjected to radial extension exhibited the minimum peak and residue shear strength while the specimen subjected under constant p loading path was in the middle. Figure 6-16b shows that under radial extension condition, the MICP treated specimen shows more dilative deformation compared with specimen under the other two loading path. By comparing the modeling and experimental results, it concludes that the model could capture the fundamental nature of MICP treated sand exhibited in the experiment quite well. The model predictions, even is satisfactory, are far from perfect as the dilation in the radial extension case in highly over predicted. It is advised that this type of problems can be dealt first by checking the parameters adopted and to see whether more appropriate values exist. It is then convenient to seek other constitutive relations between the constitutive parameters.

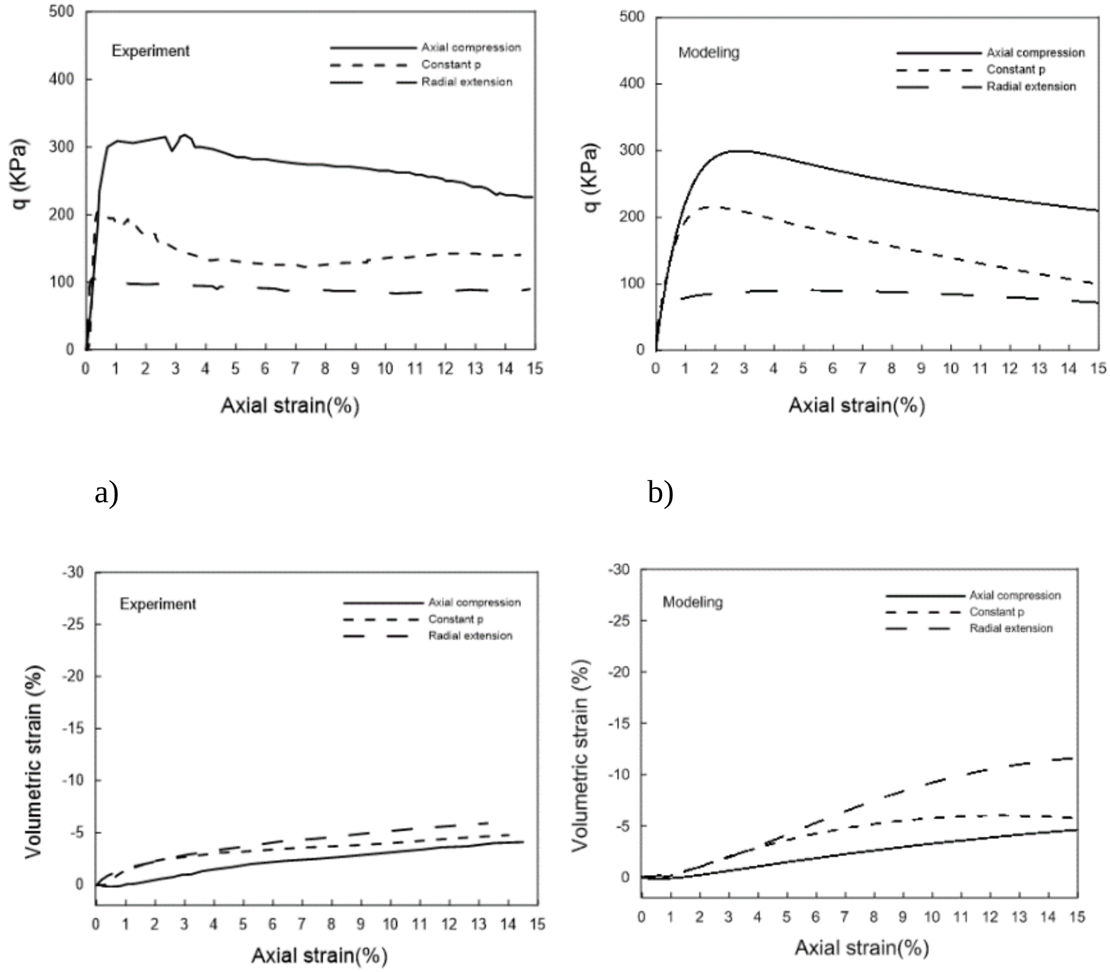

a) b)

c) d)

Figure 6-16 Comparison of experimental and modeling results of drained triaxial compression tests on MICP treated sand (a) stress–strain behavior of the experiment; (b) stress–strain behavior of modeling; c) volumetric response of the experiment; d) volumetric response of the modeling

Figure 6-17 shows the stress path evolution during loading and the evolution of void ratio versus mean effective stress. The plots on the left is experimental data and the computational results is on the right. It is clear to find in Figure 6-17a that there are disturbances happened at the final stage of the experiment which caused problems recording the corrected stress path. For example, the peak stress of the radial extension test reaches about 110 KPa in Figure 6-16a, but in Figure 6-17a, the peak stress only reaches 75 KPa which contradicts the previous results. However, this should not be a problem for the model’s capability in reproducing the stress path observed in these experiment as shown in Figure 17b. The general trend of the void ratio evolution is also captured by the model.

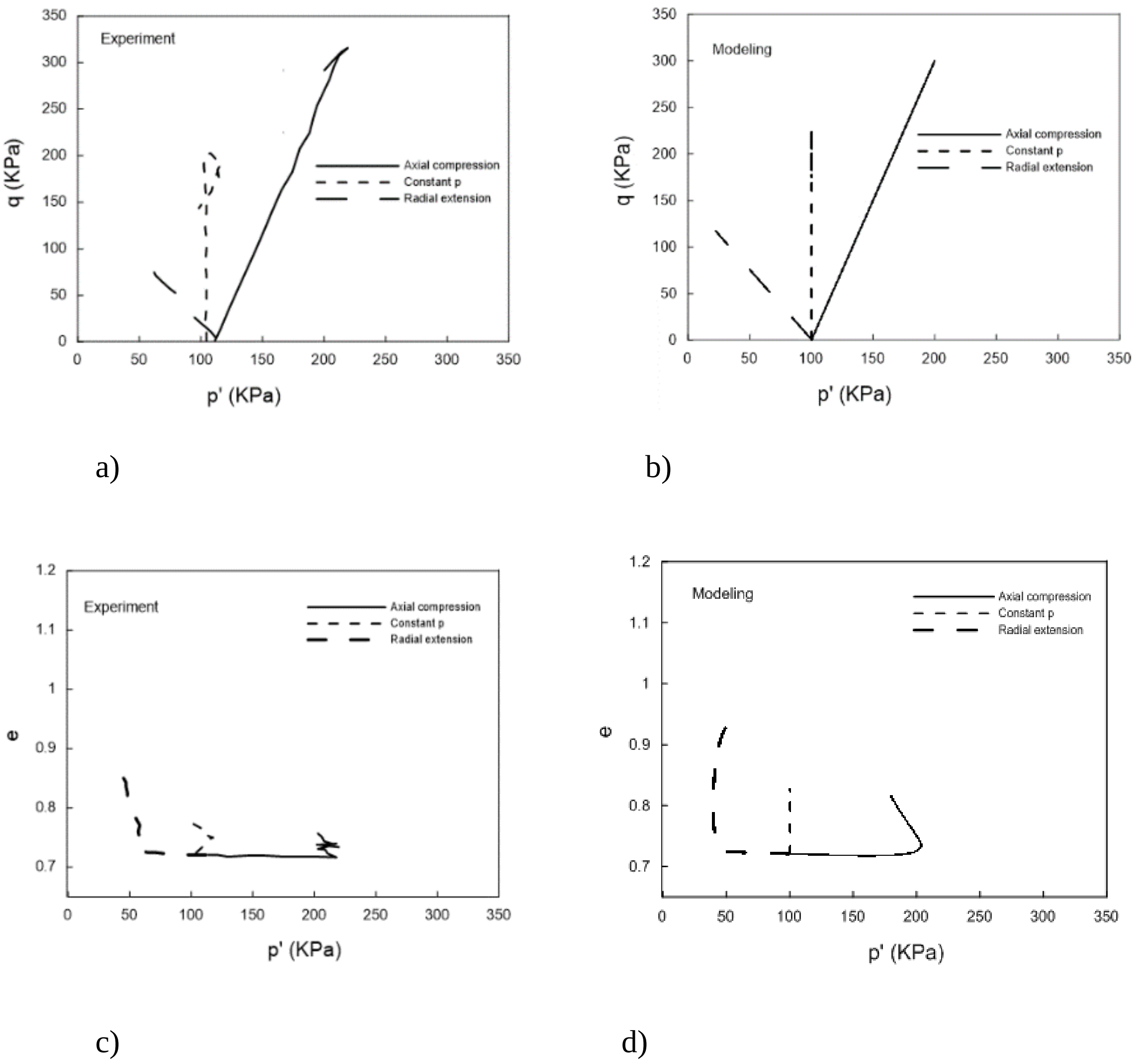

a)

b)

c)

d)

Figure 6-17 Comparison of experimental and modeling results: a) stress path evolution (experiment); b) stress path evolution (modeling); c) mean effective stress versus void ratio (experiment); d) mean effective stress versus void ratio (modeling)

6.5 Conclusion and discussion

A mechanical constitutive model for MICP treated sand was presented in this work. Experimental observations have shown that the presence of $CaCO_3$ cementation impact on different aspects of the soil behavior, amongst others: stiffness, peak stress, softening behavior and dilation. It has been observed that these features of soil behavior depend on $CaCO_3$ content, confining pressure and loading path as well.

The core components of this model include a modified Cam-Clay yield surface, sub-loading concepts for modeling the plastic strains generally observed inside the yield surface, MICP induced cementation enhancement and cementation degradation upon loading. The formal full mathematical framework was presented and discussed in detail. One thing worth mentioning is that this model contains only 8 parameters and all of them can be determined through simple experimental tests.

The resulting model has many features that appear to follow experimental observations. The model is able to reproduce the increase of stiffness, the peak strength and dilation with the increased cementation level by comparing with several drained triaxial compression experiments. A relevant feature of the model is the ability to incorporate the bond degradation during loading. A parametric study related to the bonding damage rate is performed and it showed that the damage rate parameter in this model is effective in modeling the marked strain-softening behavior of MICP treated sand specimen. The model also provided serval internal variables which can be traced during the simulation to provide a better understanding of the fundamental behavior of MICP treated sand. The behavior of MICP treated sand under various loading path is also studied through comparing the modeling and experimental results.

In general, the ability of proposed model to achieve good qualitatively results were illustrated through comparing a variety of experimental result by using one set of host sand parameters. By considering the limited number of parameters employed and the simplicity of the mathematical structure of the model, it seems possible to conclude that the model presented may be considered a useful tool to describe the MICP treated sand behavior and provide help in gaining a fundamental insight into the nature of MICP treated sand.

7 CONCLUSIONS AND SCOPE FOR FURTHER WORK

7.1 Introduction

The research presented in this dissertation covers geomechanical modeling of three distinct complex soil systems: gas hydrate bearing sediment, partially saturated soils and microbially induced calcite precipitation treated sand. For each type of soil, the dissertation follows a consistent methodology: firstly, the relevance of understanding the main features associated with the mechanical behavior of the complex soil systems under study are identified. Then the current knowledge of mechanical properties of the complex soil systems is summarized and the necessity of new research development is recognized. Lastly, the new mechanical constitutive models account for the observed mechanical response of the complex soils are described in detail and corresponding validations of the proposed models are presented and discussed. In this section, the major conclusions and future work of each complex soil are presented separately.

7.2 Gas hydrate bearing sediment

The mechanical behavior of GHBS is highly complex because of the existence of ice like hydrates in the sediments pore space. The main conclusions regarding the mechanical characteristics of GHBS are summarized as follows:

- ✓ The stiffness, shear strength and dilative deformation increase with the increase of hydrate saturation for the sample host sediment at similar condition (i.e., similar confine pressure, porosity, hydrates morphology).

- ✓ The mechanical response of GHBS depends on the type of hydrate pore habit (i.e., cementing, pore-filling, or load-bearing). The stiffness, shear strength and dilative deformation enhancement is more obvious in the cementing and loading bearing cases compared with the pore-filling.
- ✓ It is anticipated that hydrates bonding effect in cementing case will be damaged during shearing.
- ✓ It is observed that the stress level will also influence the mechanical response of GHBS. Higher confining pressure corresponds with higher stiffness and shear strength, but lower dilative deformation.
- ✓ Hydrate dissociation is accompanied by profound changes in the sediment structure. During dissociation, GHBS may experience collapse deformation or shear failure if the sample is under normally consolidated condition or the shear stress exceed the maximum shear strength.

An elastoplastic constitutive model based on HISS critical state framework was firstly introduced by the author. The major concepts adopted to accommodate the specific mechanical response of GHBS are summarized as follows:

- ✓ This model is based on critical state soil mechanics and is suitable for strain hardening/softening soils.
- ✓ This model incorporates multiple yield surfaces option which provides more flexibilities compared with previous work.
- ✓ Sub-loading concept was adopted to provide a smooth transition between elastic and plastic part.

- ✓ Hydrates enhancement to the stiffness, strength and dilative deformation was considered by expanding the original yield surfaces.
- ✓ Bonding effect and bond damage concept is incorporated to model the shear damage to the bond created by hydrates.

The model was validated through a variety of triaxial tests conducted on GHBS specimens at constant S_h and the main conclusion are shown below:

- ✓ The model was capable of capturing the difference in the mechanical response (enhanced stiffness, strength induced and dilative deformation) associated with different S_h values and also with the type of hydrate morphology.
- ✓ This model also performs well under different ranges of confining pressure. Under low confining conditions, it was observed that the hydrate sediment behaved mainly as a strain softening material, with a marked dilatant behavior. While at higher confinements, the GHBS samples tended to act mainly as a strain hardening material, with contraction under shearing loads.

A more advanced constitutive model based on critical state and stress-partition framework is presented after the HISS-MH model. The proposed model takes in account two basic aspects related to the presence of hydrates in soils:

- ✓ The model considers that hydrates contribute to the mechanical stability of the sediment and the contribution is computed through stress partition concept.
- ✓ The model contemplates that the presence of hydrates alters the mechanical behavior of sediments (e.g., providing hardening and dilation enhancement

effects), inelastic mechanisms are incorporated into a critical state model for the sediment to account for these effects.

Several mechanical tests recently published are selected to study the model capabilities. The experiments were chosen to cover the most relevant conditions related to GHBS behavior including tests performed at constant S_h. Particularly attention was paid to the study of the mechanical behavior of GHBS during hydrate dissociation under loading.

- ✓ The model's ability to reproduce the mechanical behavior of GHBS at constant S_h was investigated through a variety of tests. A wide range of hydrate saturations, confine pressure and different morphology are considered in the modeling and the model's performance during all of these conditions was extremely satisfactory.
- ✓ The model was also capable of capturing the volumetric soil collapsible compressive deformation observed during hydrate dissociation at constant stresses.
- ✓ One remarkable contribution of this model is the ability to show how sediment and hydrates contribute to the mechanical behavior of GHBS respectively and how these contributions evolve during loading and hydrates dissociation.

As for future work, it is suggested to perform more experiments to increase the available test data to help understand the mechanical behavior of GHBS. As shown in this dissertation, most of the parameters in the proposed models can be obtained from laboratory testing and it would be interesting to utilize the proposed model and experimental study at the same time: i) using the experimental data to calibrate the proposed models' parameters and further validate the models; ii) using the proposed model as a formal tool to analyze and explain the test results. Future research efforts should also be put on the implementation of the proposed models into THM-coupled modeling codes for GHBS implemented in finite element software (M Sánchez & Gai, 2016; Sanchez et al., 2014) to perform thermal-hydro-mechanical coupled analysis.

7.3 Partially saturated soil

Suction-controlled triaxial tests were conducted to investigate the mechanical behavior of partially saturated clay silt. Different suction-stress paths were produced in the experiments and the mechanical response of the soil is recorded. The samples are subjected on different hydraulic (wetting/ drying) and isotropic loading path before shearing to examine the influence of suction variations on the mechanical response of partially saturated soil. It can be concluded that the soil can become lightly over-consolidated under these hydraulic and loading path subjected before shearing. Collapsible and shrinkage (plastic) deformation may occur depending the stress level and suction experienced. The experimental programme was also focused on the determination of the mechanical parameters within the context of the model, which is formulated in the framework of hardening elasto-plasticity and uses two basic variables: the net stress and the suction.

The BBM which unitizes the parameters obtained from the tests was selected to reproduce the soil response tested. From the comparison of the experimental results and modeling results, it showed that the BBM is capable of capturing the response observed in the wetting/drying and loading/unloading test results both qualitatively and quantitatively. The stress-strain response during shearing phase was also reproduced by BBM satisfactorily. The lightly over-consolidated state of soil caused by the various stress path was reflected in the stiff pre-yield response shown in the modeling results and gradual yielding is produced for the normally consolidated sample. However, it failed in predicting the post-yield transition between the contraction and the dilatancy of the ultimate shearing stage, which experienced by all the samples. Further refinements are required to improve the agreement between predicted and observed stress-strain curves by using a different formulation of the flow rule and a gradual transition at yielding between elastic and plastic behavior.

The proposed enhanced BBM successfully eliminated the unrealistic sharp transition produced by the original BBM but kept all the other features which prove to be appropriated in modeling partially saturated soils. The dilative deformation experienced by the samples at the ultimate shearing stage are also well produced by the new enhanced BBM. It is safe to say the enhanced BBM proposed here is a valuable tool which is able to provide insight of the mechanical behavior of partially saturated soils and enhance the current understanding of this complex soil system.

7.4 MICP treated sand

A mechanical constitutive model for MICP treated sand was presented in this work. Experimental observations have shown that the presence of $CaCO_3$ cementation impact on different aspects of the soil behavior, amongst others: stiffness, peak stress, softening behavior and dilation. It has been observed that these features of soil behavior depend on $CaCO_3$ content, confining pressure and loading path as well.

The core components of this model include a modified Cam-Clay yield surface, sub-loading concepts for modeling the plastic strains generally observed inside the yield surface, MICP induced cementation enhancement and cementation degradation upon loading. The formal full mathematical framework was presented and discussed in detail. One thing worth mentioning is that this model contains only 8 parameters and all of them can be determined through simple experimental tests.

The resulting model has many features that appear to follow experimental observations. The model is able to reproduce the increase of stiffness, the peak strength and dilation with the increased cementation level by comparing with several drained triaxial compression experiments. A relevant feature of the model is the ability to incorporate the bond degradation during loading. A parametric study related to the bonding damage rate is performed and it showed that the damage rate parameter in this model is effective in modeling the marked strain-softening behavior of MICP treated sand specimen. The model also provided serval internal variables which can be traced during the simulation to provide a better understanding of the fundamental behavior of MICP treated sand. The behavior of MICP treated sand under various loading path is also studied through comparing the modeling and experimental results.

In general, the ability of proposed model to achieve good qualitatively results were illustrated through comparing a variety of experimental result by using one set of host sand parameters. By considering the limited number of parameters employed and the simplicity of the mathematical structure of the model, it seems possible to conclude that the model presented may be considered a useful tool to describe the MICP treated sand behavior and provide help in gaining a fundamental insight into the nature of MICP treated sand.

7.5 Concluding remarks

All the models present in this dissertation contain new features and advantages that previous modes did not consider. They are also able to reproduce the observed behavior with very satisfactory accuracy. Therefore, they can be used to as a tool to understand better some of the phenomena exhibited by these complex soils, which might be difficult to appreciate or quantify based on the experimental observations only.

However, there exist plenty of research efforts left regarding these models. More experimental tests should be conducted to further validate these models and then improvements can be made, if necessary. These models were developed in the general context of elasto-plasticity, which is quite straight forward to implement in finite element pieces of software. Thus, they may also be used to solve boundary value problems of practical interest with a proper implementation method.

REFERENCES

Al Qabany, A., & Soga, K. (2013). Effect of chemical treatment used in MICP on engineering properties of cemented soils. *Geotechnique, 63*(4), 331.

Al Qabany, A., Soga, K., & Santamarina, C. (2011). Factors affecting efficiency of microbially induced calcite precipitation. *Journal of Geotechnical and Geoenvironmental Engineering*, *138*(8), 992-1001.

Alonso, E. E., Gens, A., & Josa, A. (1990). A constitutive model for partially saturated soils. *Geotechnique, 40*(3), 405-430.

Aman, Z. M., Leith, W. J., Grasso, G. A., Sloan, E. D., Sum, A. K., & Koh, C. A. (2013). Adhesion force between cyclopentane hydrate and mineral surfaces. *Langmuir, 29*(50), 15551-15557.

Bachmeier, K. L., Williams, A. E., Warmington, J. R., & Bang, S. S. (2002). Urease activity in microbiologically-induced calcite precipitation. *Journal of Biotechnology, 93*(2), 171-181.

Barkouki, T., Martinez, B., Mortensen, B., Weathers, T., De Jong, J., Ginn, T., . . . Fujita, Y. (2011). Forward and inverse bio-geochemical modeling of microbially induced calcite precipitation in half-meter column experiments. *Transport in Porous Media, 90*(1), 23-39.

Barrera, M., Romero, E., Sánchez, M., & Lloret, A. (2002). Laboratory tests to validate and determine parameters of an elastoplastic model for unsaturated soils.

Beaudoin, Y., Waite, W., Boswell, R., & Dallimore, S. (2014). Frozen heat: A UNEP global outlook on methane gas hydrates. *United Nations Environment Programme, GRID-Arendal*.

Benini, S., Rypniewski, W. R., Wilson, K. S., Miletti, S., Ciurli, S., & Mangani, S. (1999). A new proposal for urease mechanism based on the crystal structures of the native and inhibited enzyme from Bacillus pasteurii: why urea hydrolysis costs two nickels. *Structure, 7*(2), 205-216.

Berge, L. I., Jacobsen, K. A., & Solstad, A. (1999). Measured acoustic wave velocities of R11 (CCl3F) hydrate samples with and without sand as a function of hydrate concentration. *Journal of Geophysical Research: Solid Earth (1978–2012), 104*(B7), 15415-15424.

Burbank, M., Weaver, T., Lewis, R., Williams, T., Williams, B., & Crawford, R. (2012). Geotechnical tests of sands following bioinduced calcite precipitation catalyzed by indigenous bacteria. *Journal of Geotechnical and Geoenvironmental Engineering, 139*(6), 928-936.

Burbank, M. B., Weaver, T. J., Green, T. L., Williams, B. C., & Crawford, R. L. (2011). Precipitation of calcite by indigenous microorganisms to strengthen liquefiable soils. *Geomicrobiology Journal, 28*(4), 301-312.

Carol, I., Rizzi, E., & Willam, K. (2001). On the formulation of anisotropic elastic degradation. I. Theory based on a pseudo-logarithmic damage tensor rate. *International Journal of Solids and Structures, 38*(4), 491-518.

Chaouachi, M., Falenty, A., Sell, K., Enzmann, F., Kersten, M., Haberthür, D., & Kuhs, W. F. (2015). Microstructural evolution of gas hydrates in sedimentary matrices observed with synchrotron X-ray computed tomographic microscopy. *Geochemistry, Geophysics, Geosystems, 16*(6), 1711-1722.

Cheng, L., & Cord-Ruwisch, R. (2012). In situ soil cementation with ureolytic bacteria by surface percolation. *Ecological Engineering, 42*, 64-72.

Cheng, L., Cord-Ruwisch, R., & Shahin, M. A. (2013). Cementation of sand soil by microbially induced calcite precipitation at various degrees of saturation. *Canadian Geotechnical Journal, 50*(1), 81-90.

Chou, C.-W., Seagren, E. A., Aydilek, A. H., & Lai, M. (2011). Biocalcification of sand through ureolysis. *Journal of Geotechnical and Geoenvironmental Engineering, 137*(12), 1179-1189.

Chu, J., Ivanov, V., Stabnikov, V., & Li, B. (2013). Microbial method for construction of an aquaculture pond in sand.

Clayton, C., Priest, J., & Rees, E. (2010). The effects of hydrate cement on the stiffness of some sands. *Geotechnique, 60*(6), 435-445.

Collett, T. S. (2002). Energy resource potential of natural gas hydrates. *AAPG bulletin, 86*(11), 1971-1992.

D'Onza, F., Gallipoli, D., Wheeler, S., Casini, F., Vaunat, J., Khalili, N., . . . Nuth, M. (2011). Benchmark of constitutive models for unsaturated soils. *Geotechnique, 61*(4), 283-302.

Dai, J., Xu, H., Snyder, F., & Dutta, N. (2004). Detection and estimation of gas hydrates using rock physics and seismic inversion: Examples from the northern deepwater Gulf of Mexico. *The Leading Edge, 23*(1), 60-66.

DeJong, J., Martinez, B., Mortensen, B., Nelson, D., Waller, J., Weil, M., . . . Fujita, Y. (2009). *Upscaling of bio-mediated soil improvement.* Paper presented at the Proc. 17th Int. Conf. on Soil Mechanics and Geotechnical Engineering, 5–9 October 2009, Alexandria, Egypt, pp. 2300–2303. Rotterdam, The Netherlands: Millpress Science Publishers.

DeJong, J., Soga, K., Kavazanjian, E., Burns, S., Van Paassen, L., Al Qabany, A., . . . Caslake, L. F. (2013). Biogeochemical processes and geotechnical applications: progress, opportunities and challenges. *Geotechnique, 63*(4), 287.

DeJong, J. T., Fritzges, M. B., & Nüsslein, K. (2006). Microbially induced cementation to control sand response to undrained shear. *Journal of Geotechnical and Geoenvironmental Engineering, 132*(11), 1381-1392.

DeJong, J. T., Mortensen, B. M., Martinez, B. C., & Nelson, D. C. (2010). Bio-mediated soil improvement. *Ecological Engineering, 36*(2), 197-210.

DeJong, J. T., Soga, K., Banwart, S. A., Whalley, W. R., Ginn, T. R., Nelson, D. C., . . . Barkouki, T. (2010). Soil engineering in vivo: harnessing natural biogeochemical systems for sustainable, multi-functional engineering solutions. *Journal of the Royal society Interface*, rsif20100270.

Desai, C. (1989). Letter to editor single surface yield and potential function plasticity models: A review. *Computers and Geotechnics, 7*(4), 319-333.

Desai, C., Somasundaram, S., & Frantziskonis, G. (1986). A hierarchical approach for constitutive modeling of geologic materials. *International Journal for Numerical and Analytical Methods in Geomechanics, 10*(3), 225-257.

Desai, C. S. (2000). *Mechanics of materials and interfaces: The disturbed state concept*: CRC press.

Duncan, J. M., & Chang, C.-Y. (1970). Nonlinear analysis of stress and strain in soils. *Journal of Soil Mechanics & Foundations Div*.

Dvorkin, J., & Uden, R. (2004). Seismic wave attenuation in a methane hydrate reservoir. *The Leading Edge, 23*(8), 730-732.

Fauriel, S., & Laloui, L. (2012). A bio-chemo-hydro-mechanical model for microbially induced calcite precipitation in soils. *Computers and Geotechnics, 46*, 104-120.

Feng, K., & Montoya, B. (2015). Influence of confinement and cementation level on the behavior of microbial-induced calcite precipitated sands under monotonic drained loading. *Journal of Geotechnical and Geoenvironmental Engineering, 142*(1), 04015057.

Fernandez, A., & Santamarina, J. (2001). Effect of cementation on the small-strain parameters of sands. *Canadian Geotechnical Journal, 38*(1), 191-199.

Fujita, Y., Taylor, J. L., Wendt, L. M., Reed, D. W., & Smith, R. W. (2010). Evaluating the potential of native ureolytic microbes to remediate a 90Sr contaminated environment. *Environmental Science & Technology, 44*(19), 7652-7658.

Gai, X., & Sancehz, M. (2016, 15th to 18th Nov. 2015.). *“Mechanical Modeling of Gas Hydrate Bearing Sediments Using an Elasto-Plastic Framework"*. Paper presented at the XV Panamerican Conference on Soil Mechanics and Geotechnical Engineering, Buenos Aires, Argentina

Gai, X., & Sánchez, M. (2017). A geomechanical model for gas hydrate-bearing sediments. *Environmental Geotechnics*, 1-14.

Gallipoli, D., D'Onza, F., & Wheeler, S. J. (2010). A sequential method for selecting parameter values in the Barcelona basic model. *Canadian Geotechnical Journal, 47*(11), 1175-1186.

Gray, D. H., & Sotir, R. B. (1996). *Biotechnical and soil bioengineering slope stabilization: a practical guide for erosion control*: John Wiley & Sons.

Hamdan, N., Kavazanjian Jr, E., Rittmann, B. E., & Karatas, I. (2017). Carbonate mineral precipitation for soil improvement through microbial denitrification. *Geomicrobiology Journal, 34*(2), 139-146.

Hashiguchi, K. (1977). Elasto-plastic constitutive laws of granular materials, Constitutive Equations of Soils. *Proc. Spec. Session 9 of 9th Int. ICSMFE*, 73-82.

Hashiguchi, K. (1989). Subloading surface model in unconventional plasticity. *International journal of solids and structures, 25*(8), 917-945.

Helgerud, M., Dvorkin, J., Nur, A., Sakai, A., & Collett, T. (1999). Elastic-wave velocity in marine sediments with gas hydrates: Effective medium modeling. *Geophysical Research Letters, 26*(13), 2021-2024.

Hyodo, M., Li, Y., Yoneda, J., Nakata, Y., Yoshimoto, N., & Nishimura, A. (2014). Effects of dissociation on the shear strength and deformation behavior of methane hydrate-bearing sediments. *Marine and Petroleum Geology, 51*, 52-62.

Hyodo, M., Nakata, Y., Yoshimoto, N., & Ebinuma, T. (2005). Basic research on the mechanical behavior of methane hydrate-sediments mixture. *Soils and foundations, 45*(1), 75-85.

Hyodo, M., Yoneda, J., Yoshimoto, N., & Nakata, Y. (2013). Mechanical and dissociation properties of methane hydrate-bearing sand in deep seabed. *Soils and foundations, 53*(2), 299-314.

Ivanov, V., & Chu, J. (2008). Applications of microorganisms to geotechnical engineering for bioclogging and biocementation of soil in situ. *Reviews in Environmental Science and Bio/Technology, 7*(2), 139-153.

James, G., Warwood, B., Hiebert, R., & Cunningham, A. (2000). Microbial barriers to the spread of pollution *Bioremediation* (pp. 1-13): Springer.

Jiang, M., Chen, H., Tapias, M., Arroyo, M., & Fang, R. (2014). Study of mechanical behavior and strain localization of methane hydrate bearing sediments with different saturations by a new DEM model. *Computers and Geotechnics, 57*, 122-138.

Jiang, M., Zhu, F., & Utili, S. (2015). Investigation into the effect of backpressure on the mechanical behavior of methane-hydrate-bearing sediments via DEM analyses. *Computers and Geotechnics, 69*, 551-563.

Kachanov, L., & Krajcinovic, D. (1987). Introduction to continuum damage mechanics. *Journal of Applied Mechanics, 54*, 481.

Kimoto, S., Oka, F., Fushita, T., & Fujiwaki, M. (2007). A chemo-thermo-mechanically coupled numerical simulation of the subsurface ground deformations due to methane hydrate dissociation. *Computers and Geotechnics, 34*(4), 216-228.

Klar, A., Soga, K., & Ng, M. (2010). Coupled deformation–flow analysis for methane hydrate extraction. *Geotechnique, 60*(10), 765-776.

Li, M., Cheng, X., & Guo, H. (2013). Heavy metal removal by biomineralization of urease producing bacteria isolated from soil. *International Biodeterioration & Biodegradation, 76*, 81-85.

Li, Y., Song, Y., Yu, F., Liu, W., & Zhao, J. (2011). Experimental study on mechanical properties of gas hydrate-bearing sediments using kaolin clay. *China Ocean Engineering, 25*, 113-122.

Lin, H., Suleiman, M. T., Brown, D. G., & Kavazanjian Jr, E. (2015). Mechanical behavior of sands treated by microbially induced carbonate precipitation. *Journal of Geotechnical and Geoenvironmental Engineering, 142*(2), 04015066.

Lin, J., Seol, Y., & Choi, J. H. (2015). An SMP critical state model for methane hydrate-bearing sands. *International Journal for Numerical and Analytical Methods in Geomechanics, 39*(9), 969-987.

Lin, J. S., Seol, Y., & Choi, J. H. (2017). Geomechanical modeling of hydrate-bearing sediments during dissociation under shear. *International Journal for Numerical and Analytical Methods in Geomechanics*.

Liu, F., Jiang, M., & Zhu, F. (2014). Discrete element analysis of uplift and lateral capacity of a single pile in methane hydrate bearing sediments. *Computers and Geotechnics, 62*, 61-76.

Mahajan, D., Taylor, C. E., & Mansoori, G. A. (2007). An introduction to natural gas hydrate/clathrate: The major organic carbon reserve of the Earth. *Journal of Petroleum Science and Engineering, 56*(1), 1-8.

Manning, D. (2008). Biological enhancement of soil carbonate precipitation: passive removal of atmospheric CO2. *Mineralogical Magazine, 72*(2), 639-649.

Martinez, B., Barkouki, T., DeJong, J., & Ginn, T. (2011). Upscaling microbial induced calcite precipitation in 0.5 m columns: Experimental and modeling results *Geo-Frontiers 2011: Advances in Geotechnical Engineering* (pp. 4049-4059).

Martinez, B., DeJong, J., Ginn, T., Montoya, B., Barkouki, T., Hunt, C., . . . Major, D. (2013). Experimental optimization of microbial-induced carbonate precipitation for soil improvement. *Journal of Geotechnical and Geoenvironmental Engineering, 139*(4), 587-598.

Martinez, B. C., & DeJong, J. T. (2009). Bio-mediated soil improvement: load transfer mechanisms at the micro-and macro-scales *Advances in Ground Improvement: Research to Practice in the United States and China* (pp. 242-251).

Masui, A., Haneda, H., Ogata, Y., & Aoki, K. (2005). *Effects of methane hydrate formation on shear strength of synthetic methane hydrate sediments.* Paper presented at the The Fifteenth International Offshore and Polar Engineering Conference.

Masui, A., Miyazaki, K., Haneda, H., Ogata, Y., & Aoki, K. (2008). *Mechanical characteristics of natural and artificial gas hydrate bearing sediments.* Paper presented at the Proceedings of the 6th International Conference on Gas Hydrates.

Miranda, C. R., & Matsuoka, T. (2008). *First-principles study on mechanical properties of CH4 hydrate.* Paper presented at the Proceedings of the 6th International Conference on Gas Hydrates.

Mitchell, J. K., & Santamarina, J. C. (2005). Biological considerations in geotechnical engineering. *Journal of Geotechnical and Geoenvironmental Engineering, 131*(10), 1222-1233.

Miyazaki, K., Masui, A., Sakamoto, Y., Aoki, K., Tenma, N., & Yamaguchi, T. (2011). Triaxial compressive properties of artificial methane-hydrate-bearing sediment. *Journal of Geophysical Research: Solid Earth (1978–2012), 116*(B6).

Miyazaki, K., Masui, A., Tenma, N., Ogata, Y., Aoki, K., Yamaguchi, T., & Sakamoto, Y. (2010). Study on mechanical behavior for methane hydrate sediment based on constant strain-rate test and unloading-reloading test under triaxial compression. *International Journal of Offshore and Polar Engineering, 20*(01).

Montoya, B., & DeJong, J. (2015). Stress-strain behavior of sands cemented by microbially induced calcite precipitation. *Journal of Geotechnical and Geoenvironmental Engineering, 141*(6), 04015019.

Mortensen, B., Haber, M., DeJong, J., Caslake, L., & Nelson, D. (2011). Effects of environmental factors on microbial induced calcium carbonate precipitation. *Journal of applied microbiology, 111*(2), 338-349.

Nova, R. (1988). Sinfonietta classica: an exercise on classical soil modeling. *Constitutive Equations for Granular non-cohesive soils*, 501-519.

Nova, R., & Wood, D. M. (1979). A constitutive model for sand in triaxial compression. *International Journal for Numerical and Analytical Methods in Geomechanics, 3*(3), 255-278.

Pinkert, S. (2016). Rowe’s Stress-Dilatancy Theory for Hydrate-Bearing Sand. *International Journal of Geomechanics*, 06016008.

Pinkert, S., & Grozic, J. (2014). Prediction of the mechanical response of hydrate-bearing sands. *Journal of Geophysical Research: Solid Earth, 119*(6), 4695-4707.

Pinyol Puigmartí, N. M., Vaunat, J., & Alonso Pérez de Agreda, E. (2007). A constitutive model for soft clayey rocks that includes weathering effects.

Priest, J. A., Rees, E. V., & Clayton, C. R. (2009). Influence of gas hydrate morphology on the seismic velocities of sands. *Journal of Geophysical Research: Solid Earth, 114*(B11).

Romero, E., Facio, J., Lloret, A., Gens, A., & Alonso, E. (1997). *A new suction and temperature controlled triaxial apparatus.* Paper presented at the Proceedings of the International Conference on Soil Mechanics on Soil Mechancs and Foundation Engineering.

Romero Morales, E. E. (1999). *Characterisation and thermo-hydro-mechanical behavior of unsaturated Boom clay: an experimental study*: Universitat Politècnica de Catalunya.

Roscoe, K. H., & Burland, J. (1968). On the generalized stress-strain behavior of wet clay.

Rowe, P. W. (1962). *The stress-dilatancy relation for static equilibrium of an assembly of particles in contact.* Paper presented at the Proceedings of the royal society of London a: mathematical, physical and engineering sciences.

Rutqvist, J., & Moridis, G. J. (2007). *Numerical studies on the geomechanical stability of hydrate-bearing sediments.* Paper presented at the Offshore Technology Conference.

Sanchez, M., & Gai, X. (2016, 29th to 31st Aug.). *Geomechanical and numerical modeling of gas hydrate sediments.* Paper presented at the 1st International Conference on Energy Geotechnics, Kiel, Germany.

Sánchez, M., & Gai, X. (2016). *Geomechanical and numerical modeling of gas hydrate sediments.* Paper presented at the Energy Geotechnics: Proceedings of the 1st International Conference on Energy Geotechnics, ICEGT 2016, Kiel, Germany, 29-31 August 2016.

Sánchez, M., Gai, X., & Santamarina, J. C. (2017). A constitutive mechanical model for gas hydrate bearing sediments incorporating inelastic mechanisms. *Computers and Geotechnics, 84,* 28-46.

Sanchez, M., Gai, X., Shastri, A., & Santamarina, J. (2014). *Coupled THCM Modeling of Gas Hydrate Bearing Sediments.* Paper presented at the AGU Fall Meeting Abstracts.

Santamarina, J. C., Dai, S., Jang, J., & Terzariol, M. (2012). Pressure core characterization tools for hydrate-bearing sediments. *Sci. Drill, 14*(4).

Santamarina, J. C., Dai, S., Terzariol, M., Jang, J., Waite, W. F., Winters, W. J., . . . Fujii, T. (2015). Hydro-bio-geomechanical properties of hydrate-bearing sediments from Nankai Trough. *Marine and Petroleum Geology, 66*, 434-450.

Shastri, A. (2014). *Advanced Coupled THM Analysis in Geomechanics.*

Shen, J., Chiu, C., Ng, C. W., Lei, G., & Xu, J. (2016). A state-dependent critical state model for methane hydrate-bearing sand. *Computers and Geotechnics, 75*, 1-11.

Shen, Z., & Jiang, M. (2016). DEM simulation of bonded granular material. Part II: Extension to grain-coating type methane hydrate bearing sand. *Computers and Geotechnics, 75*, 225-243.

Shen, Z., Jiang, M., & Thornton, C. (2016). DEM simulation of bonded granular material. Part I: Contact model and application to cemented sand. *Computers and Geotechnics, 75*, 192-209.

Sloan, S. W. (1987). Substepping schemes for the numerical integration of elastoplastic stress–strain relations. *International journal for numerical methods in engineering, 24*(5), 893-911.

Soga, K., Lee, S., Ng, M., & Klar, A. (2006). Characterisation and engineering properties of methane hydrate soils. *Characterisation and engineering properties of natural soils*, 2591-2642.

Stocks-Fischer, S., Galinat, J. K., & Bang, S. S. (1999). Microbiological precipitation of CaCO 3. *Soil Biology and Biochemistry, 31*(11), 1563-1571.

Sultan, N., & Garziglia, S. (2011). *Geomechanical constitutive modeling of gas-hydrate-bearing sediments*. Paper presented at the The 7th International Conference on Gas Hydrates (ICGH 2011).

Tagliaferri, F., Waller, J., Andò, E., Hall, S. A., Viggiani, G., Bésuelle, P., & DeJong, J. T. (2011). Observing strain localisation processes in bio-cemented sand using x-ray imaging. *Granular Matter, 13*(3), 247-250.

Uchida, S., Soga, K., & Yamamoto, K. (2012). Critical state soil constitutive model for methane hydrate soil. *Journal of Geophysical Research: Solid Earth (1978–2012), 117*(B3).

Uchida, S., Xie, X. G., & Leung, Y. F. (2016). Role of critical state framework in understanding geomechanical behavior of methane hydrate-bearing sediments. *Journal of Geophysical Research: Solid Earth*.

Van Paassen, L. (2011). Bio-mediated ground improvement: from laboratory experiment to pilot applications *Geo-Frontiers 2011: Advances in Geotechnical Engineering* (pp. 4099-4108).

van Paassen, L. A., Daza, C. M., Staal, M., Sorokin, D. Y., van der Zon, W., & van Loosdrecht, M. C. (2010). Potential soil reinforcement by biological denitrification. *Ecological Engineering, 36*(2), 168-175.

van Paassen, L. A., Ghose, R., van der Linden, T. J., van der Star, W. R., & van Loosdrecht, M. C. (2010). Quantifying biomediated ground improvement by ureolysis: large-scale biogrout experiment. *Journal of Geotechnical and Geoenvironmental Engineering, 136*(12), 1721-1728.

Van Wijngaarden, W., Vermolen, F., van Meurs, G. A., & Vuik, C. (2011). Modeling biogrout: a new ground improvement method based on microbial-induced carbonate precipitation. *Transport in Porous Media, 87*(2), 397-420.

Van Wijngaarden, W., Vermolen, F., Van Meurs, G. A., & Vuik, C. (2012). A mathematical model and analytical solution for the fixation of bacteria in Biogrout. *Transport in Porous Media, 92*(3), 847-866.

Waite, W. F., Santamarina, J. C., Cortes, D. D., Dugan, B., Espinoza, D., Germaine, J., . . . Shin, H. (2009). Physical properties of hydrate-bearing sediments. *Reviews of Geophysics, 47*(4).

Weil, M. H., DeJong, J. T., Martinez, B. C., & Mortensen, B. M. (2011). Seismic and resistivity measurements for real-time monitoring of microbially induced calcite precipitation in sand.

Wheeler, S., Gallipoli, D., & Karstunen, M. (2002). Comments on use of the Barcelona Basic Model for unsaturated soils. *International Journal for Numerical and Analytical Methods in Geomechanics, 26*(15), 1561-1571.

Whiffin, V. S., van Paassen, L. A., & Harkes, M. P. (2007). Microbial carbonate precipitation as a soil improvement technique. *Geomicrobiology Journal, 24*(5), 417-423.

Xuerui, G., & Marcelo, S. (2017). A geomechanical model for gas hydrate-bearing sediments. *Environmental Geotechnics, 4*(2), 143-156. doi:10.1680/jenge.15.00050

Yoneda, J., Masui, A., Konno, Y., Jin, Y., Egawa, K., Kida, M., . . . Tenma, N. (2015). Mechanical properties of hydrate-bearing turbidite reservoir in the first gas production test site of the Eastern Nankai Trough. *Marine and Petroleum Geology, 66*, 471-486.

Yu, Y., Cheng, Y. P., Xu, X., & Soga, K. (2016). Discrete element modeling of methane hydrate soil sediments using elongated soil particles. *Computers and Geotechnics*.

Yun, T., Francisca, F., Santamarina, j., & Ruppel, C. (2005). Compressional and shear wave velocities in uncemented sediment containing gas hydrate. *Geophysical Research Letters, 32*(10).

Yun, T., Narsilio, G. A., & Santamarina, J. C. (2006). Physical characterization of core samples recovered from Gulf of Mexico. *Marine and Petroleum Geology, 23*(9), 893-900.

Yun, T. S., Santamarina, J. C., & Ruppel, C. (2007). Mechanical properties of sand, silt, and clay containing tetrahydrofuran hydrate. *Journal of Geophysical Research: Solid Earth (1978–2012), 112*(B4).

Zhang, X.-H., Lu, X.-B., Zhang, L.-M., Wang, S.-Y., & Li, Q.-P. (2012). Experimental study on mechanical properties of methane-hydrate-bearing sediments. *Acta Mechanica Sinica, 28*(5), 1356-1366.